MODELING AND SIMULATION OF DYNAMIC

PROBLEMS IN SOLID MECHANICS USING

MATERIAL POINT METHOD

By

NITIN PANDURANG DAPHALAPURKAR

Bachelor of Engineering in Mechanical Engineering
University of Pune
Pune, India
2002

Master of Science in Mechanical Engineering
Oklahoma State University
Stillwater, Oklahoma
2004

Submitted to the Faculty of the
Graduate College of the
Oklahoma State University
in partial fulfillment of
the requirements for
the Degree of
DOCTOR OF PHILOSOPHY
December, 2008

MODELING AND SIMULATION OF DYNAMIC

PROBLEMS IN SOLID MECHANICS USING

MATERIAL POINT METHOD

Dissertation Approved:

Dr. Hongbing Lu
_____
Dissertation Advisor


Dr. Ranga Komanduri
_____
Committee Member


Dr. Jay Hanan
_____
Committee Member


Dr. Satish Bukkapatnam
_____
Committee Member


Dr. A. Gordon Emslie
_____
Dean of the Graduate College

Finally, my eternal appreciation to my parents Pandurang and Rupali Daphalapurkar, who have also been my teachers, and whose blessings and motivation, have helped me arrive at this prestigious level in academics.

TABLE OF CONTENTS

LIST OF FIGURES

CHAPTER I

INTRODUCTION

A novel computational method, namely, the material point method (MPM) was introduced by Sulsky (Sulsky *et al.* 1995) at the University of New Mexico in collaboration with the researchers of the Sandia National Laboratory for solving dynamic problems in solid mechanics. Sulsky *et al.* (1995) demonstrated the advantages of MPM by simulating a copper bar undergoing large deformations; while other methods, such as finite element method (FEM) in this process were faced with extensive challenges. Professors Lu and Komanduri recognized the advantages of this novel method and have been one of the major contributors in the development of MPM since then. In this study, the basic numerical methodology (as introduced by Sulsky) has been used to further build upon the advancements, in order to make MPM more versatile and powerful. In this regard, various material simulations were carried out. In this process, the MPM algorithm was developed by either implementing completely newer capabilities of simulation or refining the older versions for increased robustness and versatility.

Professors Lu, Komanduri, and Roy at Oklahoma State University in Stillwater recognized that the particle nature of this novel method can be used to couple atomistic to continuum, and to develop multiscale material simulation algorithms. To pursue this aspect, hierarchical mesh refinement was developed to refine the continuum material

(simulated using MPM) down to atomistic scale [simulated using molecular dynamics (MD)]. The method was verified using purely MD simulations and used to investigate dynamics of micro-tensile testing at high-strain rates (Lu *et al.* 2006).

Further, MPM was used to study dynamic crack growth by implementing the cohesive zone model, the details of which are included in Chapter III. MPM, as generalized by Bardenhagen and Kober (2002, 2004), was used to improve the numerical accuracy of the explicit time-stepping solution, during convection of particles over the grid. Multiple velocity field technique was used in MPM to enable it to handle discrete discontinuity on each side of the interface. Multilevel refinements along with parallel computation (both were built upon SAMRAI by Ma *et al.* 2004) were adapted in the region around the crack-tip to resolve higher strain gradients. Numerical simulations of the crack growth in a homogeneous elastic solid under mode-II plane strain conditions were conducted with the crack propagating along a weak interface. A parametric study was conducted to investigate the dynamics of crack growth. Numerical results (Daphalapurkar *et al.* 2007) are compared qualitatively with the available experimental results. The simulations were able to handle the crack growth with crack-tip velocities in both sub-Rayleigh and intersonic regimes. Crack initiation and propagation were the natural outcomes of the simulations incorporating the cohesive zone model.

Simulation of realistic microstructures has been an inherent advantage of modeling using MPM, due to ease in discretization of material geometry. This fact has been used to demonstrate the simulation of closed-cell foam structure in compression, and is discussed in Chapter IV. The microstructural evolution of closed-cell polymethacrylimide foam was simulated in compression undergoing elastic, compaction, and densification stages.

The three-dimensional microstructure of the foam was determined using micro-computed tomography ($\mu$-CT), and was converted to the material points for simulations using the MPM. The properties of the cell-walls were determined from nanoindentation on the cell-walls of the foam. MPM simulations were able to capture the three-stages of deformation which are typical for foams in compression. Simulated features of microstructure evolution were compared qualitatively with the *in-situ* observations of the foam under compression using $\mu$-CT.

The mechanics of granular materials (e.g. sand) has been an area of increasing interest in the past ten years, due mainly to the challenges it poses in addressing its behavior (such as mechanisms of deformation, flow, and fracture of granular materials under load) as well as due to the emerging technologies, such as $\mu$-CT, X-ray radiography, and laminography as well as the rapidly increasing computing power available that facilitates in addressing its complex behavior. However, this area remains to be relatively insufficiently understood. One of the requirements within this study is measuring the properties of granular media. Measurement of mechanical properties, mainly, the Young's modulus, hardness, stress-strain relationship, and failure behavior of granular materials (e.g. fine sand particles) by conventional material testing methods, such as tensile/compressive testing is difficult due to limitations on the size of individual particles (a few micrometers). This can be overcome by using the recently introduced nanoindentation testing machine. Chapter V deals with measurement of properties of one such granular material, namely sand. In this investigation, a Berkovich nanoindenter was used to measure the Young's modulus, hardness, and fracture toughness. An inverse problem solving approach was used to determine the stress-strain behavior of sand at the

3

granular level, by allowing the numerically simulated nanoindentation load-displacement data to correlate with the measured values. A cube-corner indenter tip was used to generate radial cracks. The lengths of these cracks were used to determine the fracture toughness of sand grains. The mechanical property data (along with statistical variability of individual sand grains) measured in this investigation can be used in the simulations of sand at the granular or meso scale.

Following the measurement of mechanical properties of granular media in Chapter V, Chapter VI discusses implementation of contact algorithm and friction to simulate the interaction between grains. In order to simulate the flow or deformation of granular media (e.g. sand) under various loading conditions using MPM, it would require implementation of various phenomenological models such as (but not limited to) cohesive zone model (to model the fracture and fragmentation of sand grains), contact algorithm and friction between sand grains, and constitutive model for sand grain material. In this part of the study, a contact algorithm is implemented in 3D MPM. A new methodology is used to update the surface normals during successive MPM simulation time steps. This methodology conserves the original geometry of the bodies in contact, thus increasing the accuracy of the results. Slip (considering Coulomb friction) has been implemented for the interfaces in contact. For verification, results obtained from the rolling simulation of a sphere on an inclined plate are used to compare with their corresponding analytical solutions. Both stick and slip occurrences have been demonstrated in these rolling simulations.

CHAPTER II

MATERIAL POINT METHOD (MPM)

2.1   Background

MPM was developed by Sulsky *et al.* (1995) from FLIP (Fluid - implicit - particle) particle-in-cell (PIC) (Harlow, 1964; Brackbill and Ruppel, 1986) method by extending the computational fluid dynamics capability of the code, to solving solid mechanics problems. MPM has combined the advantages of both Eulerian scheme (provided by the grid) and the Lagrangian scheme (provided by the material points). The grid is usually held fixed, and is used to determine spatial gradients and for solving field equations. Irregular transitional grid can be used to improve the accuracy in the case of highly localized strain gradients. The material points are convected by the deformation of the solid throughout the background grid and are not subjected to mesh tangling. Additionally, incorporation of various constitutive material models in MPM is relatively straightforward. For example, each material point can have a different mass and Young's modulus. In the case where the material points move in a single-valued velocity field, no-slip contact between the surfaces can be handled automatically.

Although finite element method (FEM) has been used for many years for addressing many solid mechanics problems, the newly introduced MPM has following advantages:

a.   It can handle no-slip contact naturally.

b. It is capable of handling large deformations. Since the background mesh is fixed, it does not experience any mesh lock-up or element degeneracy which are sometimes experienced in FEM;

c. It can easily couple with molecular dynamics (MD) simulations, and link length/time scales, because of the use of material points (similar to atoms used in MD) instead of arbitrary sized elements in FEM;

d. Parallel computation is more straightforward with MPM because of the use of a grid structure that is consistent with parallel computing grids;

e. Use of the background grid in MPM enables structured adaptive refinement for local interested regions; and

f. Ease in implementation of constitutive relations with history dependent variables.

Essentially MPM gives same results as FEM under small deformations; however, under large non-linear deformations FEM sometimes quits (might be due to mesh distortions or degeneracy) while MPM doesn't and still gives valid results. Sulsky *et al.* (1994) initially demonstrated the potential of MPM to 2D impact problems. A more general description of MPM, along with special considerations relevant to axisymmetric problems, was given by Sulsky and Schreyer (1996). This method combines the advantages of Lagrangian and Eulerian methods and has proven to be useful for solving solid mechanics problems involving materials with history dependent properties, such as plasticity or viscoelasticity effects. MPM is amendable to parallel computation (Parker 2002), implicit integration method for unconditionally stable time increments (Guilkey and Weiss 2003, Sulsky and Kaul 2003, Cummins and Brackbill 2001) and alternative

interpolation schemes using $C^1$ continuous interpolating functions for improved smoothness in field properties (Bardenhagen and Kober 2000). Bardenhagen and Kober (2000), suggested the improved MPM as generalized interpolation material point (GIMP) method. However, if we take a look back through decades of development of finite element method, there have been many improvements in its methodologies, including the shape functions, to further its application. Going through all its development, the original name phrased as 'Finite Element Method (FEM)' has been persistent. In this regard, considering a similar reasoning, this work will refer to the method 'generalized interpolation material (GIMP) method' also as 'material point method (MPM)' as originally coined by Sulsky *et al.* (1995).

2.2 Numerical Methodology

As stated earlier, material point method (Sulsky *et al.* 1995) has been improved further by Bardenhagen and Kober (2000) by incorporating $C^1$ continuous shape function to overcome some of the problems encountered with MPM, such as numerical instability and noise in the stress field when material points cross the cell-walls. We present in some detail their improved material point method (MPM).

In MPM, material continuum is discretized into a finite collection of N material areas (2D), or volumes (3D) as shown in Fig. 1.1 (Tan and Nairn, 2002). For convenience, each material volume is represented by a circle only as a schematic representation. The actual volume can be square for 2D case (cube for 3D case) in the reference configuration and quadrilateral in the deformed state with its center located at the center of the circle. Each material volume is assigned a mass ($m_p$, where $p = 1,…, N$) consistent with the material

density and volume ($V_p$) of the point, and all other variables, such as position, acceleration, velocity, strain and stress, and temperature. Physical variables carried by the points are projected onto the background grid, and motion and energy equations are solved at the background computational grid (or mesh).
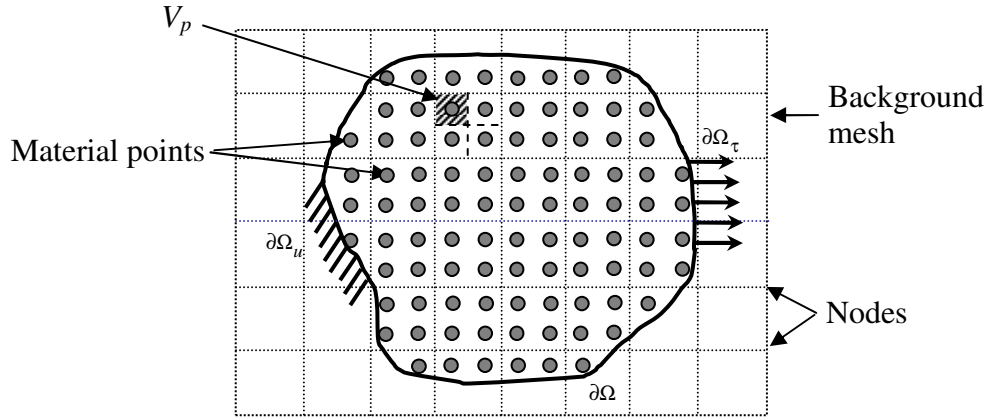


Figure 1.1:  Schematic of MPM grid cells with material points
(adapted from Tan and Nairn, 2002)

Equations used here for MPM numerical scheme have been developed by Sulsky *et al.* (1995). The governing equations for such dynamic simulations are the mass and momentum conservation equations:

$$\frac{d\rho}{dt} + \rho \nabla \cdot \mathbf{v} = 0 \text{, and} \tag{2.1}$$

$$\rho \mathbf{a} = \nabla \cdot \boldsymbol{\sigma} + \mathbf{b}. \tag{2.2}$$

where $\rho$ is the material mass density, $\mathbf{a}$ is the acceleration, $\boldsymbol{\sigma}$ and $\mathbf{b}$ are the Cauchy stress tensor and body force density, respectively.

The displacement and traction boundary conditions are given as

$$\mathbf{u} = \overline{\mathbf{u}} \text{ on } \partial\Omega_u, \tag{2.3}$$

$$\boldsymbol{\tau} = \overline{\boldsymbol{\tau}} \text{ on } \partial\Omega_\tau, \tag{2.4}$$

8

$$\boldsymbol{\tau}_{coh} = \overline{\boldsymbol{\tau}}_{coh} \text{ on } \partial\Omega_{coh}, \tag{2.5}$$

where $\partial\Omega_u \cap \partial\Omega_\tau = \varnothing$, $\partial\Omega_{coh} \cap \partial\Omega_\tau = \varnothing$ and $\partial\Omega = \partial\Omega_u \cup \partial\Omega_\tau \cup \partial\Omega_{coh}$. In variational

form, the momentum conservation equation is written as

$$\int_\Omega \rho\mathbf{a}\cdot\boldsymbol{\delta v}dx = \int_\Omega (\nabla\cdot\boldsymbol{\sigma})\cdot\boldsymbol{\delta v}dx + \int_\Omega \mathbf{b}\cdot\boldsymbol{\delta v}dx, \tag{2.6}$$

where $\boldsymbol{\delta v}$ is an admissible velocity field.

Applying the chain rule, $(\nabla\cdot\boldsymbol{\sigma})\cdot\boldsymbol{\delta v} = \nabla\cdot(\boldsymbol{\sigma}\cdot\boldsymbol{\delta v}) - \boldsymbol{\sigma}:\nabla\boldsymbol{\delta v}$, and the divergence

theorem, Eq. (2.6) can be written as

$$\int_\Omega \rho\mathbf{a}\cdot\boldsymbol{\delta v}dx + \int_\Omega \boldsymbol{\sigma}:\nabla\boldsymbol{\delta v}dx = \int_\Omega \mathbf{b}\cdot\boldsymbol{\delta v}dx + \int_{\partial\Omega_\tau} \overline{\boldsymbol{\tau}}\cdot\boldsymbol{\delta v}dS + \int_{\partial\Omega_{coh}} \overline{\boldsymbol{\tau}}_{coh}\cdot\boldsymbol{\delta v}dS + \int_{\partial\Omega_u} \overline{\boldsymbol{\tau}}_u\cdot\boldsymbol{\delta v}dS. \tag{2.7}$$

Here, $\boldsymbol{\tau}_u$ is the resultant traction due to the displacement boundary condition on $\partial\Omega_u$, $\overline{\boldsymbol{\tau}}$

is the external traction vector, and $\overline{\boldsymbol{\tau}}_{coh}$ is the cohesive traction at the interface $\partial\Omega_{coh}$. In

MPM, the domain $\Omega$ is discretized into a collection of material particles, with $\Omega_p$ as the

domain of particle $p$. Physical quantities, such as mass, stress, and momentum are defined

for each particle. For example, the momentum for particle $p$ can be expressed as

$\mathbf{p}_p = \int_{\Omega_p} \rho(\mathbf{x})\mathbf{v}(\mathbf{x})\chi_p(\mathbf{x})d\mathbf{x}$, where $\mathbf{v}(\mathbf{x})$ is the velocity and $\chi_p(\mathbf{x})$ is the particle

characteristic function. From this, the particle volume is calculated by $V_p = \int_{\Omega\cap\Omega_p} \chi_p(\mathbf{x})d\mathbf{x}$.

The momentum conservation equation is thus discretized as

$$\sum_p \int_{\Omega\cap\Omega_p} \frac{\dot{\mathbf{p}}_p\chi_p}{V_p}\cdot\boldsymbol{\delta v}dx + \sum_p \int_{\Omega\cap\Omega_p} \boldsymbol{\sigma}_p\chi_p:\boldsymbol{\delta v}dx =$$

$$\sum_p \int_{\Omega\cap\Omega_p} \frac{m_p\chi_p}{V_p}\boldsymbol{b}\cdot\boldsymbol{\delta v}dx + \sum_p \int_{\partial\Omega_\tau\cap\Omega_p} \overline{\boldsymbol{\tau}}\cdot\boldsymbol{\delta v}dS + \sum_p \int_{\partial\Omega_{coh}\cap\Omega_p} \overline{\boldsymbol{\tau}}_{coh}\cdot\boldsymbol{\delta v}dS + \sum_p \int_{\partial\Omega_u\cap\Omega_p} \overline{\boldsymbol{\tau}}_u\cdot\boldsymbol{\delta v}dS \tag{2.8}$$

where $m_p$ is the lumped mass of each material particle. In order to simplify computations, the lumped mass is used instead of consistent mass matrix. Introducing a background grid and the grid shape function $S_i(\mathbf{x})$, the admissible velocity field can be represented by the grid nodal data as $\delta \mathbf{v} = \sum_i \delta \mathbf{v}_i S_i(\mathbf{x})$. Here, the grid shape function satisfies partition of unity $\sum_i S_i(\mathbf{x}) = 1$.

The momentum conservation, Eq. (2.8), can eventually be written for each node $i$ as

$$\dot{\mathbf{p}}_i = \mathbf{f}_i^{\text{int}} + \mathbf{f}_i^b + \mathbf{f}_i^\tau + \mathbf{f}_i^{coh}. \tag{2.9}$$

Here, the time rate of change of momentum is $\dot{\mathbf{p}}_i = \sum_p \overline{S}_{ip} \mathbf{p}_p / \Delta t$, $\hspace{2cm}$ (2.9a)

the nodal internal force vector $\mathbf{f}_i^{\text{int}} = -\sum_p \boldsymbol{\sigma}_p \cdot \overline{\nabla S}_{ip} V_p$, $\hspace{2cm}$ (2.9b)

the body force vector $\mathbf{f}_i^b = \sum_p m_p \mathbf{b} \overline{S}_{ip}$, $\hspace{2cm}$ (2.9c)

and the external force vector $\mathbf{f}_i^\tau = \sum_p \int_{\partial\Omega_\tau \cap \Omega_p} \overline{\boldsymbol{\tau}} S_i(\mathbf{x}) dS$, $\hspace{2cm}$ (2.9d)

and the cohesive force vector $\mathbf{f}_i^{coh} = \sum_p \int_{\partial\Omega_{coh} \cap \Omega_p} \overline{\boldsymbol{\tau}}_{coh} S_i(\mathbf{x}) dS$. $\hspace{2cm}$ (2.9e)

$\overline{S}_{ip}$ is the weighting function between particle $p$ and node $i$, given as

$$\overline{S}_{ip} = \frac{1}{V_p} \int_{\Omega \cap \Omega_p} \chi_p(\boldsymbol{x}) S_i(\boldsymbol{x}) d\boldsymbol{x}. \tag{2.10}$$

The weighting function in MPM is $C^1$ continuous and satisfies partition of unity, as given by Bardenhagen and Kober (2004). The momentum conservation equation [Eqn. (2.8)] is solved at each node to update the nodal momentum, acceleration, and velocity. These updated nodal quantities are interpolated to the material particles to update the

particle position, velocity, stress, and strain. The material constitutive relation can be represented as

$$\boldsymbol{\sigma} = \mathbf{C} : \boldsymbol{\varepsilon} \text{ and } \boldsymbol{\varepsilon} = \frac{1}{2} \left[ (\nabla \mathbf{u}) + (\nabla \mathbf{u})^{\mathrm{T}} \right], \tag{2.11}$$

where $\mathbf{C}$ is the fourth-order elasticity tensor, $\boldsymbol{\varepsilon}$ is the infinitesimal strain tensor. This work will consider only the isotropic materials under infinitesimally small deformations.

The mass of each material particle does not change throughout the computation so that the mass conservation equation is automatically satisfied. Using a background grid, the weak form of momentum conservation equation is discretized. In our computations, a spatially fixed structured grid is chosen for convenience. The equations listed above are applicable for both 2D and 3D. For a uniform structural grid, the grid shape function in 2D is defined as the product of two nodal tent functions (Bardenhagen and Kober, 2004)

$$S_i(\boldsymbol{x}) = S_i^x(x) S_i^y(y), \tag{2.12}$$

in which the nodal tent functions are in the same form, e.g.,

$$S_i^x(x) = \begin{cases} 0 & x - x_i \leq -L_x \\ 1 + (x - x_i)/L_x & -L_x \leq x - x_i \leq 0 \\ 1 - (x - x_i)/L_x & 0 \leq x - x_i \leq L_x \\ 0 & L_x \leq x - x_i \end{cases} \tag{2.13}$$

where $2L_x$ is the background mesh cell-length.

Also, the particle characteristic function of the material particle located at $(x_p, y_p)$ is taken as

$$\chi_p(\mathbf{x}) = \chi_p^x(x) \chi_p^y(y), \tag{2.14}$$

and $\chi_p^x(x) = H[x - (x_p - l_x)] - H[x - (x_p + l_x)], \tag{2.15}$

where $H$ denotes the Heavyside unit step function and $2l_x$ is the particle size along $x$ axis.

With Eqn. (2.15) as particle characteristic function, the weighing function [from Eqn. (2.10)] can be evaluated (Bardenhagen and Kober, 2004) as

$$\bar{S}_{ip}^{x} = \begin{cases} 0 & x - x_i \leq -L_x - l_x \\ \left(L_x + l_x + (x - x_i)\right)^2 / 4L_x l_x & -L_x - l_x < x - x_i \leq -L_x + l_x \\ 1 + (x - x_i)/L_x & -L_x + l_x < x - x_i \leq -l_x \\ 1 - \left((x - x_i)^2 + l_x^2\right)/2L_x l_x & -l_x < x - x_i \leq l_x \\ 1 - (x - x_i)/L_x & l_x < x - x_i \leq L_x - l_x \\ \left(L_x + l_x - (x - x_i)\right)^2 / 4L_x l_x & L_x - l_x < x - x_i \leq L_x + l_x \\ 0 & L_x + l_x < x - x_i \end{cases} \qquad (2.16)$$

Thus, for a cuboid particle in 3D the weighting function between particle $p$ and node $i$, can be written as

$$\bar{S}_{ip}(\boldsymbol{x}) = S_{ip}^{x}(x) S_{ip}^{y}(y) S_{ip}^{z}(z). \qquad (2.17)$$

CHAPTER III

DYNAMIC CRACK GROWTH SIMULATION USING COHESIVE ZONE MODEL

AND MATERIAL POINT METHOD

3.1   Introduction

Dynamic fracture has been an area of sustained interest with the aim of understanding various phenomena in engineering and geosciences. Linear elastic fracture mechanics (LEFM) has been applied extensively to crack dynamics. However, LEFM has been effective mainly for brittle fracture phenomena and not so in dealing with materials undergoing ductile fracture. More particularly, it does not provide a physical description on how the crack process zone is formed and how its state affects the crack propagation phenomena (Yang and Ravi-Chandar, 1996). Dugdale (1960) and Barenblatt (1962) introduced a methodology to explicitly model the crack process zone by considering crack opening displacements and tractions over the crack surface. This approach is applicable for both ductile and quasi-brittle materials and independent of the microstructure at the crack-tip. As far as numerical implementation is concerned, the introduction of the cohesive element methods (Needleman, 1987; Camacho and Ortiz, 1996) provided a detailed force-separation relation as well as the cohesive strength in the process zone. Their applications have resulted in satisfactory explanations of numerous phenomena related to crack dynamics.

MPM does not use body-fixed mesh for computation, giving it an advantage in simulations of some dynamic problems in solid mechanics over finite element and meshless methods, (Nairn and Guo, 2005). Thus, modeling a crack is relatively easier compared to FEM. Multiple velocity-field technique can be used to model discontinuities in the displacements and velocities across the propagating crack surfaces. In this part of the work, a methodology of incorporating cohesive zone model in MPM is proposed to simulate damage zone at the crack-tip. A parametric study is carried out by varying the impact speeds and the cohesive strengths. The results obtained for one of the cases are compared with the experimental results of Rosakis *et al.* (1999).

3.2   Background

The past decade has seen advances in the field of dynamic fracture, including experimental and numerical observations, determination of limiting velocities for crack propagation in different modes, allowable speed regimes for crack propagation, intersonic crack propagation, and sub-Rayleigh to intersonic transition mechanism. The research has been progressing towards the development of a phenomenological model as well as a unifying theory that incorporates the physical basis at all scales from atomistic to continuum, and even extending to geological scales.

Majority of studies involving size effects were carried out using molecular dynamics (MD) simulations.  For example, Abraham and Gao (2000) performed MD simulations of mode-II crack propagation along a weak interface between two harmonic crystals. Their simulations showed that a shear dominated crack initially accelerates to the Rayleigh wave speed, followed by the nucleation of a daughter microcrack ahead of the main

crack, and finally coalescence of the mother and daughter-cracks with the crack-tip velocity reaching a value as high as the longitudinal wave speed. After coalescence, when the far-field loading is relaxed, the crack decelerates and propagates at a steady rate close to a speed of $\sqrt{2}\ c_S$, where $c_S$ is the shear wave speed of the bulk material. Abraham and Gao (2000) also reported that the essential features in the results obtained from MD simulations matched well with the experimental observations reported by Rosakis *et al.* (1999)*,* as well as with the results using cohesive zone modeling (Needleman, 1999), even though they were results obtained at different scales.

Even though large scale simulations of up to one-billion atoms have been reported using massive parallel processing (Abraham and Gao, 2000), most MD simulations reported in the literature are still somewhat limited in their size (a few thousand atoms). As a result, multiscale simulation approaches (see Lu *et al.* 2006) requiring seamless coupling between atomistic and continuum have been emerging. The applicability of these methods, in general, and the development of continuum methods containing atomistic information, in particular, are of great interest to researchers. Both microscopic scale and continuum scale simulations are necessary to reflect appropriate behavior of dynamic fracture since dominant physical processes occur at both these scales. They include, mechanisms seen in ductile materials, such as void formation, their coalescence into microcracks, and subsequent growth into macrocracks; phase transformations; and friction at the asperity level involving junction formation and collapse. In all these cases, continuum simulations of dynamic fracture require a unifying law that will take into account the physics of deformation as well as the length scale phenomena.

A critical contribution to the computational fracture mechanics has been the development and application of cohesive element methods (Needleman, 1987; Tvergaard and Hutchinson, 1993; Xu and Needleman, 1994; Camacho and Ortiz, 1996, Leonov and Panasyuk, 1998). Modeling using these methods enables simulation of a nonlinear zone at the crack-tip. The modeling of complex fracture phenomena, such as crack branching, kinking is still under development. For instance, using a cohesive element network, there is an artificial softening of material properties as the size of cohesive elements decreases (Falk *et al.* 2001).

Belytschko and co-workers (Moes and Belytschko, 2002) developed a new class of cohesive elements which allows the crack to propagate through an element instead of just at the element boundaries and termed it the extended finite element method (XFEM). Thus, constraint in the direction of crack motion is relieved. Furthermore, Belytschko *et al.* (2003) developed a methodology to switch from a continuum to a discrete discontinuity based on loss of hyperbolicity of the governing partial differential equations. They used the XFEM to deal with the discontinuity.

Gao and Klein (1998) used the virtual internal bond (VIB) method for crack growth simulation. In this model, randomized cohesive bond interactions are incorporated into the constitutive law and cohesive interactions are assumed between the material particles. Gao and Ji (2003) used VIB method to model nanomaterials and demonstrated that at a critical length scale of one nanometer, there is a change in the fracture mechanism from the classical Griffith fracture to one involving homogenous failure near the theoretical strength of solids. For this transition, they replaced the classical singular deformation

field near a crack-tip by a uniform stress distribution with no stress concentration near the crack-tip.

Considerable amount of analytical, experimental, and numerical work has been reported in the literature on intersonic crack growth (Gao *et. al.* 2001; Huang and Gao; 2001; Klein *et. al.* 2001; Rosakis 2002; Guo *et. al.* 2003; Hao *et. al.* 2004; and Xia *et. al.* 2004, 2005). The term *intersonic speed* is referred to as the crack-tip velocity between shear and dilatational wave speeds of the material, while the term *sub-Rayleigh speed* is referred to as the crack-tip velocity less than the Rayleigh wave speed of the material.

Washabaugh and Knauss (1994) observed that the sustained mode-I crack-tip velocity is always less than the Rayleigh wave speed of the material. Ravi-Chandar and Knauss [1984 (a), (b)] observed microcracks on the trailing crack surfaces and pointed out that this crack branching was responsible for limiting the crack-tip velocities. They designed a fracture specimen with a weak plane possessing varying bond strengths so that the mode-I crack was guided to propagate along the weak plane. They concluded that for mode-I, the crack-tip velocity approaches asymptotically the Rayleigh wave speed of the material in the limit of vanishing bond strengths.

Andrews (1976) presented numerical work on plane strain, mode-II dominated shear cracks and concluded that the crack would rapidly accelerate at first, toward the Rayleigh wave speed and then after a short period of adjustment would start propagating at a speed close to but greater than $\sqrt{2}\, c_S$. Following Andrews (1976) work, Burridge *et al.* (1979) studied the steady motion of a semi-infinite mode-II shear crack driven by a moving point load which remains at a constant distance $d$ from the crack-tip. Based on their analysis, they reported that for very large values of $d$, the sub-Rayleigh regime and the regime

17

between the shear wave speed, $c_S$ and the transition speed of $\sqrt{2}\, c_S$ is unstable for crack propagation.

Broberg (1989) used energy considerations and concluded that the crack-tip velocity regime between $c_S$ and dilatational wave speed, $c_D$ is forbidden for mode-I and the regime between $c_R$ and $c_S$ is forbidden for both mode-I and mode-II propagating cracks due to negative energy release rate in these regions. Freund (1979) used an asymptotic analysis for the steady state mode-II intersonic crack and determined that $\sqrt{2}\ c_S$ is the only stable intersonic crack propagation velocity. Rosakis *et al.* (1999) conducted experiments on fracture specimens with a weak plane successfully constraining a shear dominated crack to propagate along this weak plane under remote loading conditions. They observed crack-tip velocities in intersonic regime with crack pattern featuring shear shock waves and discussed the significance of the intersonic crack propagation at preferred velocity of $\sqrt{2}\ c_S$ which is consistent with the analysis by Freund (1979).

Although considerable work has been focused on rate-independent cohesive zone models, Knauss (1993) presented a rate-dependent cohesive surface relation incorporating viscoelasticity and studied crazing in thermoplastic polymers. Since then, many researchers have been working on rate-dependent cohesive zone models for analytical (Samudrala *et al.* 2002) and numerical solutions (Nguyen *et al.* 2004). Cohesive zone models are anticipated to have a significant potential in dynamic fracture modeling, including, fragmentation (Cirak *et al.* 2004), crack branching (Xu and Needleman, 1994, Belytschko *et al.* 2003), and kinking (Borst *et al.* 2006). At larger scales, geophysicists model earthquakes as shear cracks propagating along tectonic plates with faults, or weak interfaces (Xia *et. al.* 2005). Depending on the local topography and

the geological age of a fault, the wave speeds across a fault or inhomogeneity would vary. Thus the fault is modeled as a weak plane along which mode-II cracks would dynamically propagate (Rosakis, 2002). This is of particular interest to geophysicists who investigate intersonic fault rupture during shallow crustal earthquake events. Preferred weak planes exist even in earth's crust in which the dominant fault motion is unstable shear crack growth between tectonic plates during earthquakes.

MPM has been applied to analyze a wide range of problems, including dynamic material failure, such as spall failure in brittle materials using decohesion constitutive model (Sulsky and Schreyer, 2004). Nairn and Guo (2005) applied MPM for fracture problems in brittle materials. They used multiple velocity fields at nodes and allowed MPM to handle cracks by introducing a discontinuity in the single-valued velocity field. In their study, the crack propagation is based on critical stress intensity factors and energy criteria. They reported that MPM is able to model explicit cracks very well and also passes the crack patch test with good accuracy. In this investigation, we implemented cohesive zone model in MPM method to model crack propagation. This method can deal with cracks in both ductile and brittle materials. Additionally, the incorporation of a characteristic length scale in the cohesive zone model allows investigation of physics-based (Klein *et al.* 2001) crack propagation behavior.

## 3.3  Cohesive Zone Model Implementation in Material Point Method

### 3.3.1  Cohesive surface constitutive law

In this investigation, plane-strain conditions are assumed and the cohesive surface decohesion formulation of Needleman (1990) and Xu and Needleman (1994) is used. The

continuum is characterized by two constitutive relations, namely, one that relates stress and deformation in the bulk material using the generalized Hooke's law and the other that relates traction and displacement jump across a cohesive surface. Strength and work of separation per unit area are included as part of this latter characterization and thus a characteristic length enters the formulation. In addition to the material models mentioned above, appropriate balance laws together with the initial and boundary conditions define completely the boundary value problem. Crack initiation and crack growth are the natural outcome of the cohesive law of separation. The cohesive surface constitutive relation used allows for both tangential and normal decohesion.

The normal and tangential traction expressions are given as (Needleman, 1999)

$$T_n = -\frac{\phi_n}{\delta_n} exp\left(-\frac{\Delta_n}{\delta_n}\right) \left\{ \frac{\Delta_n}{\delta_n} exp\left(-\frac{\Delta_t^2}{\delta_t^2}\right) + \frac{1-q}{r-1} \left[1 - exp\left(-\frac{\Delta_t^2}{\delta_t^2}\right)\right] \left[r - \frac{\Delta_n}{\delta_n}\right] \right\}$$

$$T_t = -\frac{\phi_n}{\delta_n} \left(2\frac{\delta_n}{\delta_t}\right) \frac{\Delta_t}{\delta_t} \left\{ q + \left(\frac{r-q}{r-1}\right) \frac{\Delta_n}{\delta_n} \right\} exp\left(-\frac{\Delta_n}{\delta_n}\right) exp\left(-\frac{\Delta_t^2}{\delta_t^2}\right) \tag{3.1}$$

where, $\Delta_n = \mathbf{n} \cdot \boldsymbol{\Delta}$, $\Delta_t = \mathbf{t} \cdot \boldsymbol{\Delta}$, $T_n = \mathbf{n} \cdot \mathbf{T}$, and $T_t = \mathbf{t} \cdot \mathbf{T}$ with $\boldsymbol{\Delta} = \mathbf{u}^+ - \mathbf{u}^-$ is the difference between the displacement at the upper surface and the bottom surface; $\mathbf{n}$ and $\mathbf{t}$ are the unit normal and tangent vectors to the surface at a given point in the reference configuration. Further, the ratio $q = q = \phi_t/\phi_n$ and $r = \Delta_n^*/\delta_n$, where $\Delta_n^*$ is the value of $\Delta_n$ after complete shear separation with $T_n = 0$.

Figure 3.1 shows the normal and shear tractions across a cohesive surface. The normal work ($\phi_n$) and shear work ($\phi_t$) of separation are given as

$$\phi_n = e\sigma_{max}\delta_n , \qquad \phi_t = \sqrt{\frac{e}{2}}\tau_{max}\delta_t , \tag{3.2}$$
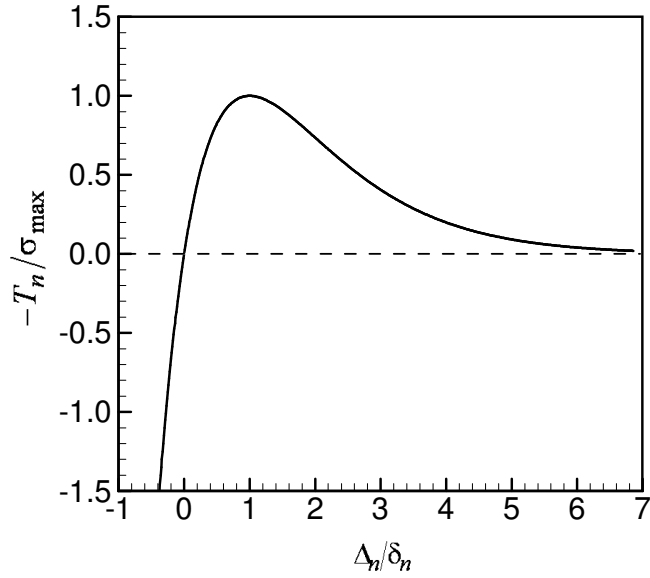
Figure 3.1 (a): Normalized traction, $T_n$, on the cohesive surface as a function of $\Delta_n/\delta_n$ with $\Delta_t = 0$. (after Needleman, 1999)
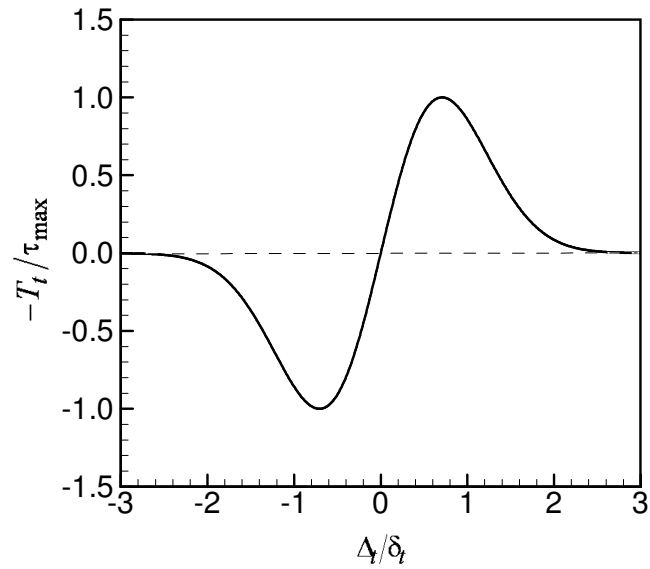


Figure 3.1 (b): Normalized traction, $T_t$, on the cohesive surface as a function of $\Delta_t/\delta_t$ with $\Delta_n = 0$. (after Needleman, 1999)

where, $\sigma_{max}$ and $\tau_{max}$ are the cohesive surface normal and shear strengths respectively, $e$ is

2.71828, and $\delta_n$ and $\delta_t$ are characteristic lengths corresponding to displacement jumps to

the cohesive surface in the normal ($\Delta_n$) and tangential directions ($\Delta_t$), respectively. The

21

traction components given in Eqn. (3.1) are integrated over the cohesive segments, or cohesive elements, which are part of the discretized interface in this case. It may be noted that we use four point Gaussian quadrature method to integrate the traction over the crack segments and neglect the effect of crack segment rotation assuming that crack opening displacements remain infinitesimal.

### 3.3.2 Modeling of cohesive zone in MPM

Cohesive segments (or elements) are separate from MPM background mesh elements. Thus, MPM can allow extension of new fracture surfaces without any restrictions from the background mesh elements. In this investigation, we focus on the crack propagation along the interface in the horizontal direction by defining a weak plane directly in front of the initial crack-tip. To reduce computational time, we avoid additional calculations pertaining to the classification of nodes and particles across the interface by letting the material points in the upper and lower parts of the plate (with respect to the interface) to convect in their own velocity fields. Thus, by adopting multiple velocity fields (Hu and Chen, 2003; Nairn and Guo, 2005), there is no interaction between the material points on either side of the interface and surfaces on both sides of the interface are connected to each other only through the cohesive zone model.

The interface is discretized into cohesive segments and, each segment is defined by two cohesive nodes, forming a line for 2D description of the crack surface. The more the cohesive nodes are within a particular length, the more accurate is the model of the crack surface. The length scales involve a macroscopic length scale characterized by the size of the body, a length scale associated with the computational background mesh size, $l_m$, and

the cohesive zone size length, $l_c$. The elastic properties of the bulk material ($E$ and $\nu$), the

cohesive zone strength ($\tau_{max}$), surface energy ($\gamma$), and the crack propagation velocity ($v_c$)

determine the cohesive zone size. In our simulations, we have considered a simple finite

traction separation potential at the continuum level, proposed by Morrissey and Rice

(1998) as an approximate expression for the cohesive zone length at zero crack velocity

given by $l_C \left( \text{for } v_c = 0 \right) \approx \dfrac{9\pi}{32} \left( \dfrac{E}{1-\nu^2} \right) \dfrac{2\gamma}{\tau_{max}^2}$, with $l_c$ being the cohesive segment (i.e.,

element) length. However, the cohesive zone length decreases as the crack-tip velocity

increases. In our final simulations, we used background mesh size of 62.5 µm for impact

velocities below 10 m/s and background mesh size of 31.25 µm for impact velocities

higher than 10 m/s (based on the convergence study). We fixed the cohesive segment

length to ~ 2 µm (< $l_m$, where $l_m$ is the background mesh size) for higher resolution of the

cohesive zone within the grid element. As a result, the grid size is ~ 15 times or higher of

the cohesive element size. This high resolution cohesive segment length along with

smooth interpolation functions over the background mesh elements resolves the cohesive

zone very well in all our simulations.

   We next consider an interface defined by cohesive nodes represented by smaller solid

black circles, as shown in Fig. 3.2. For simplicity, we shall consider an example of a plate

with separated interfaces forming the crack surfaces. The bigger solid grey circles are the

material points convecting over the background grid. While defining a vertical or slant

weak plane with this methodology is also possible, we restrict our investigation to

horizontal interfaces. Each of the surfaces, namely, upper and lower surfaces, has surface

nodes associated with them. These nodes overlap initially when there is no displacement

jump over the interface. The material points in the upper and lower plates are convected onto two different velocity fields. Thus, there is no interaction between the material points in the upper and lower plates. Both surfaces along the interface move in their respective velocity fields, defined by material points in the upper and lower plates, respectively. The crack opening displacement (COD) measured at each crack node corresponds to the displacement jump between two crack nodes on the opposite surfaces at the interface when they were originally (time = 0) overlapping.
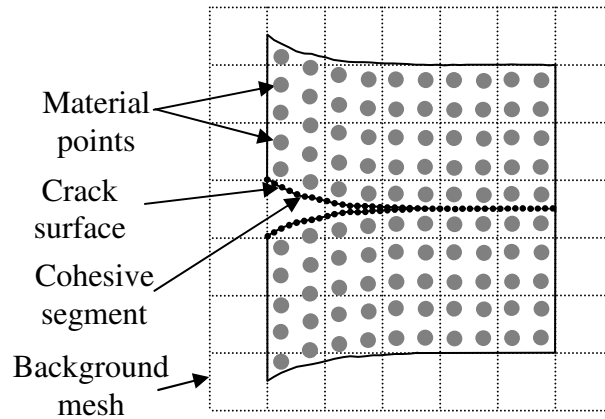


Figure 3.2: Plate with crack showing cohesive segments
(adapted from Tan and Nairn, 2002)

While carrying out the MPM calculations at each time step, we move the surfaces belonging to the interface in their corresponding velocity field. As the surfaces move, they contribute to displacement jump on nodes over the interface. We now consider a segment being formed between two crack nodes, initially joined in the reference state, which we will term as the cohesive segment. The cohesive tractions are integrated over cohesive segments forming the interface, using the procedure described in Needleman (1987). Thus, at the end of the time step, we have displacement jumps at the interface nodes along with the restoring forces acting on them at the interface. This restoring force

at crack nodes is interpolated to the surrounding background mesh nodes based on the weight functions and adds to the total nodal force for solving the governing equations for the next time step.

## 3.4  Simulation of Mode-II Crack Propagation in a Homogeneous, Isotropic, Linear Elastic Material

Rosakis *et al*. (1999) investigated experimentally the intersonic crack growth in homogeneous elastic solids subjected to remote shear loading, using Homalite plates with specimen geometry and loading conditions as shown in Fig. 3.3. They introduced a weak plane by bonding two Homalite plates with an adhesive having bonding modulus similar to bulk material. We use the same model geometry and introduce a weak plane using prearranged cohesive segments along a horizontal line and a predefined initial sharp crack of length 25 mm. Thus, the mode-II crack is constrained to propagate along this weak plane. Coker *et. al.* (2003) conducted simulations of crack propagation in bimaterials, and provided an estimate of static strength of the adhesive as $\sigma_{max} = \tau_{max} = 24$ MPa (or 0.4615 % of the Young's modulus of the bulk material) and we will use the same values in our simulations. The remaining parameters characterizing the cohesive surface used are, $\delta_n = 0.4$ μm, $r = 0$, and $q = 1$, which gives $\delta_t = 0.9327$ μm (Needleman, 1999). We assume elastic material behavior and plane strain conditions. Material properties used for Homalite are Young's modulus $E = 5.2$ GPa, Poisson's ratio $v = 0.34$, and mass density $\rho = 1246$ kg/m$^3$. These material properties correspond to Homalite's dynamic properties at a strain rate of $\sim 10^3$ s$^{-1}$. For this material, with plane strain

idealization, the dilatational ($c_D$), shear ($c_S$), and Rayleigh ($c_R$) wave speeds are given by (see, e.g., Freund, 1998 and Liu *et al.*, 2005)

$$c_D = \left(\frac{\kappa+1}{\kappa-1} \cdot \frac{\mu}{\rho}\right)^{1/2}, \qquad c_S = \left(\frac{\mu}{\rho}\right)^{1/2}, \qquad c_R = c_S \frac{0.862+1.14v}{1+v}, \tag{3.3}$$

where, $\mu = E/(2+2v)$ is the shear modulus, and $\kappa = 3-4v$ for plane strain deformation and $\kappa = (3-v)/(1+v)$ for plane stress deformation.

Thus, for Homalite material and plane strain conditions, $c_D$ = 2,534 m/s, $c_S$ = 1,248 m/s, and $c_R$ = 1,164 m/s. These wave speeds are represented in Fig. 3.4 along with the terminologies for each regime.
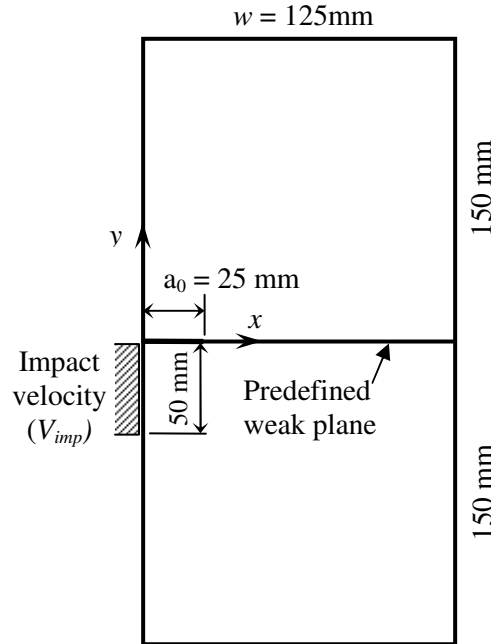


Figure 3.3:  Geometry of the specimen and loading conditions.

At time $t$ = 0, the body is stress-free and at rest. A normal velocity is prescribed at the edge $x$ = 0, and -50 mm $\leq y \leq 0$. The remaining external surfaces are traction-free. The applied velocity is given by

$$V(t) = \begin{cases} V_1 \, t/t_r, & \text{for } 0 \le t < t_r; \\ V_1 & \text{for } t_r \le t \le \left(t_p + t_r\right) \\ V_1\left[1 - \left(t - t_p\right)/t_s\right] & \text{for } t_p < t < \left(t_p + t_s + t_r\right) \\ 0, & \text{for } t \ge \left(t_p + t_s + t_r\right) \end{cases} \qquad (3.4)$$

where $t_p$ is the pulse time, and $t_r$, and $t_s$ are the rise time and step-down time, respectively. The velocity profile selected is a representative of experimental conditions. The pulse time in the experiments depended on the length of the projectile used. In our simulations, the times used were adapted from Needleman (1999) and Coker *et al.* (2003).
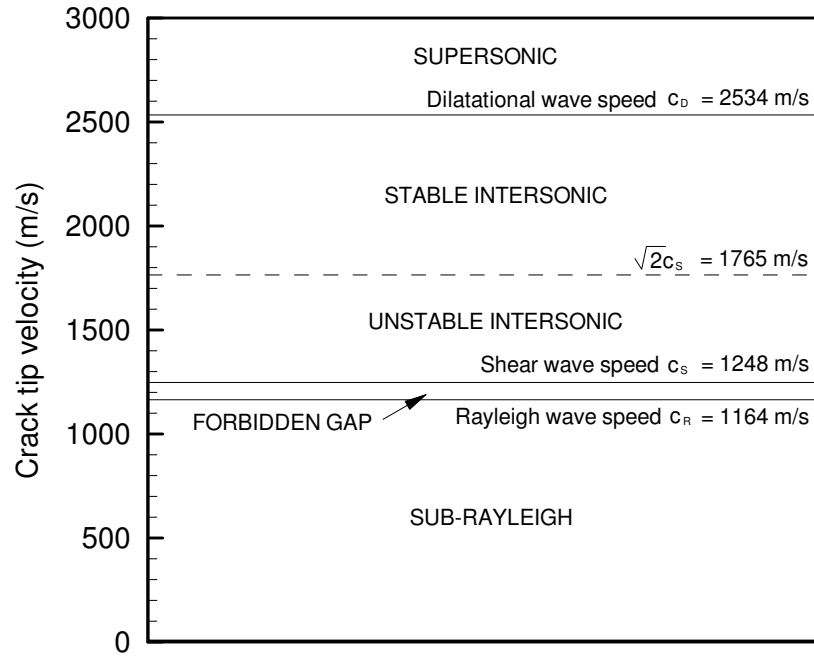


Figure 3.4: Representative plot showing wave speeds for Homalite-100 and nomenclature of various regions.

Numerical simulations of dynamic crack propagation were carried out using the methodology presented in Section 3.3 on an 8-node parallel computer cluster (processor speed of 3.8 GHz each) using the Linux operating system. Simulations were carried out until 19.2 µs time and took ~ 48 hrs of computational time to complete. The parallel

27

environment was provided by the Structured Adaptive Mesh Refinement Application Infrastructure (SAMRAI) (Hornung and Kohn, 2002) developed at the Lawrence Livermore National Laboratory (LLNL). The geometry of the plate is discretized using material points with different levels of refinement. The background mesh consists of two-dimensional, 4-node, square elements covering the entire region. Four material points are used to represent the material in each cell. Here, each material point area equals to a quarter of the area of each cell. Here, each material point area equals to a quarter of the area of each cell. Mesh convergence study is conducted using the sustained crack-tip velocity and interface cohesive forces. The smallest cell length used in these simulations was 31.25 µm. We make use of the structured mesh refinement scheme in MPM to communicate between successive levels (Ma, *et al.* 2005) with changing mesh size. Fig. 3.5 is a schematic of the geometric model used with six predefined levels of refinement. In this case, level 0 corresponds to the background mesh of cell-length 2 mm while each immediate finer level has a cell-length, half of the cell-length in the immediate coarser level. Thus, the finest level (level 6) has cell length of 31.25 µm. The pattern of refinement is chosen to accommodate the cohesive zone in the finest level so as to reveal the structure of the cohesive zone. The background mesh defined using the refinement pattern is fixed in all the simulations. A total of 12,000 cohesive segments are pre-defined between $x = 25$ mm to $x = 50$ mm, which defines the interface in front of the initial notch. The simulation time ends at 19.2 µs which is before the dilatational waves reach the end of the predefined cohesive segments (at $x = 50$ mm) on the right hand side.

The simulation results are presented in the form of shear stress contours, plots of crack propagation velocity and position histories, interface profile, and cohesive forces

along the interface. In Section 3.6, we also compare our results with the experimental results of Rosakis *et al.* (1999) in terms of photoelastic stress patterns.
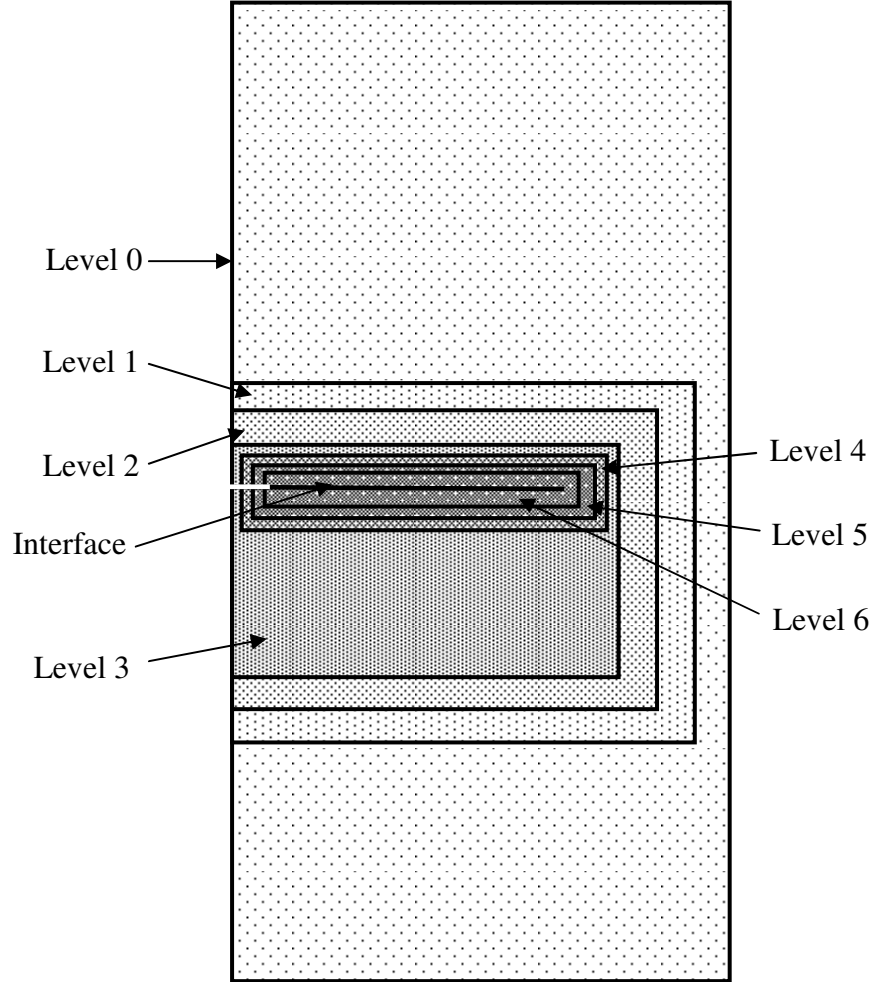


Figure 3.5: Specimen geometry showing structured mesh refinement levels used for the simulation of asymmetric impact of a projectile.

In their experiments, Rosakis *et al.* (1999) used dynamic transmission photoelasticity to determine the stress field around the interface. In this technique, isochromatic fringes are related to the contours of $(\sigma_1 - \sigma_2)$ through the stress-optics relation, with $\sigma_1$ and $\sigma_2$ being the maximum and minimum in-plane principle stresses. Thus

$$(\sigma_1 - \sigma_2) = \frac{NF_\sigma}{h} \tag{3.3}$$

where $F_\sigma$ is the stress optical coefficient of Homalite, $h$ is the specimen thickness, and $N$ is the bright isochromatic fringe order.

## 3.5 Results

Dynamic fracture simulations were carried out under the loading and geometry conditions identical to Rosakis *et al.* (1999) experiments (see Fig. 3.3 for details). The results are presented in terms of shear stress contours, crack-tip position and velocity histories, and cohesive forces at the interface. Also, features that are characteristic of intersonic crack growth, such as shear shock waves and transition mechanism from sub-Rayleigh to intersonic crack-tip velocities are presented. Next, a mesh convergence study is presented (Section 3.5.2) to demonstrate the convergence of results with decreasing mesh size. In the discussion part (Section 3.6), additional results of shear dominated crack growth with varying impact speeds and cohesive strengths are discussed. Finally, the stress contours are compared with the experimental results of Rosakis *et al.* (1999).

## 3.5.1 Intersonic crack growth at an impact speed of 30 m/s

Numerical simulations were conducted for asymmetric impact of a projectile at $V_{imp} =$ 30 m/s using the specimen geometry and loading conditions shown in Fig. 3.3 with normal and shear cohesive strengths of 24 MPa. Fig. 3.5 shows the mesh used in the simulations, where the smallest mesh size used is 31.25 µm. Isochromatic fringe patterns (contours of maximum shear stress, $\tau_{max}$) at different times are shown in Fig. 3.6.
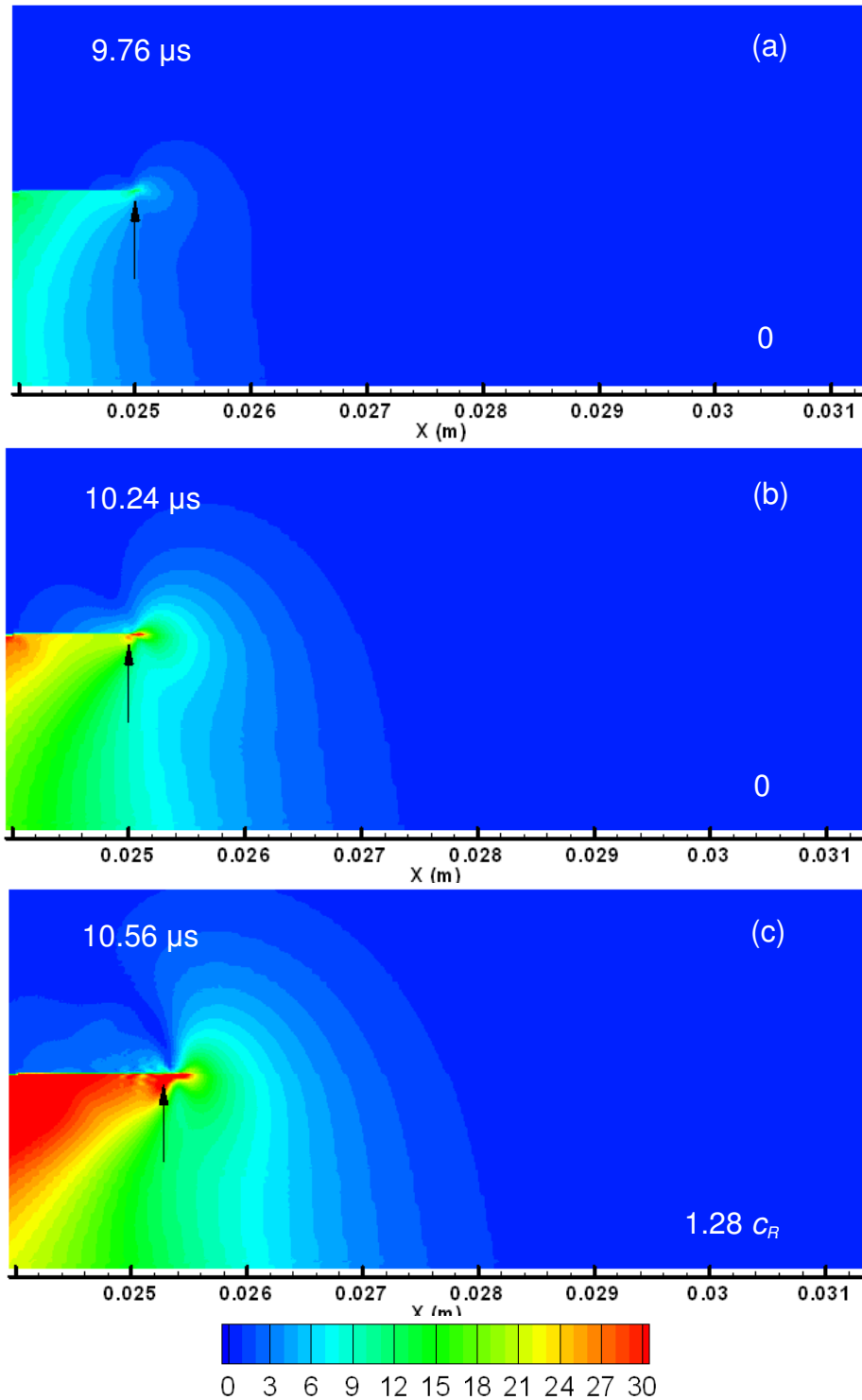
Figure 3.6: Snapshots of $\tau_{\max}$ (MPa), ($V_{imp}$ = 30 m/s) at various durations ($c_R$ = 1164 m/s)
  (a) Stress wavefront arriving at the initial crack-tip
  (b) Stress wavefront loading the initial crack in predominantly shear mode
  (c) Crack has propagated along the interface after initiation at 10.4 µs
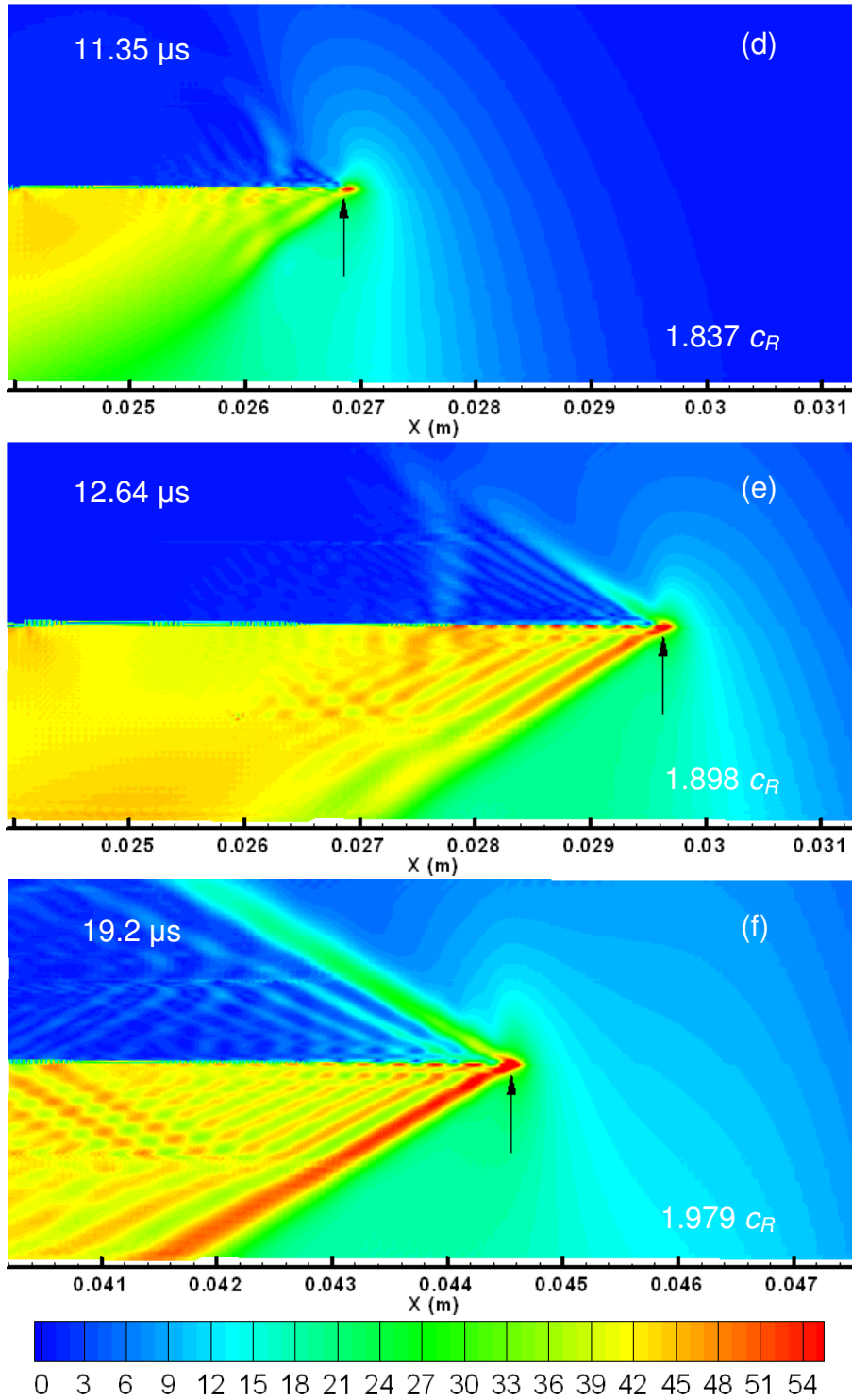
Figure 3.6: Snapshots of $\tau_{\max}$ (MPa), ($V_{imp}$ = 30 m/s) at various durations ($c_R$ = 1164 m/s)
    (d)  Maximum shear stress pattern immediately after the transition mechanism
    (e)  Formation of shear shock waves
    (f)  Crack propagation at a sustained crack-tip velocity in intersonic regime.

In each frame, the corresponding time and crack-tip velocities are shown along with the crack-tip position indicated by an arrow. In Fig. 3.6 (a), the traveling wavefront arrives at the initial crack-tip, loading the crack-tip predominantly in the shear mode. The stress wave travels over the interface onto the upper half of the workpiece and envelops the initial crack-tip [Fig. 3.6 (b)]. In the next frame [Fig. 3.6 (c)] (corresponding to time 10.56 µs), the crack has propagated along the interface after initiating at 10.4 µs. The maximum shear stress pattern is typical of a crack propagating at sub-Rayleigh speeds under shear dominated loading. The crack propagates at sub-Rayleigh speeds until 11 µs, after which it propagates at intersonic speeds, with the stress patterns shown in Figs. 3.6 (d), (e), and (f). For frames after ~ 11 µs time [Figs. 3.6 (d)-(f)] there is a significant change in the fringe pattern.
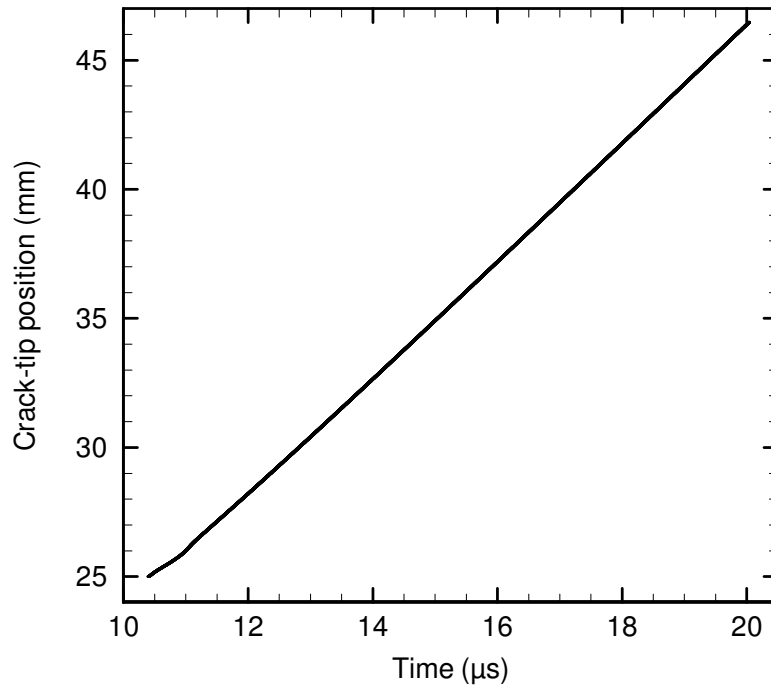


Figure 3.7: Plot of crack-tip position versus time for $V_{imp} = 30$ m/s

There are two lines of discontinuity (called the shear shock waves) emanating from the crack-tip in all these frames. Fig. 3.6 (f) is taken downstream from the initial notch. The inclination of these shear shock waves with the horizontal gives the velocity of the crack-tip. The crack-tip location and velocity history are shown in Figs. 3.7 and 3.8, respectively. The crack-tip is defined as the farthest point from the initial crack-tip where the displacement jump is $5\delta_t$. The crack-tip velocity at a particular time is obtained by the slope of the crack-tip history using the least square fitting of a straight line over 31 consecutive crack-tip positions.

At higher velocities, the angle becomes smaller. The expression relating the shear shock angle with the crack-tip velocity is given by

$$\beta = \sin^{-1}\left(\frac{c_s}{v_c}\right) \tag{3.4}$$
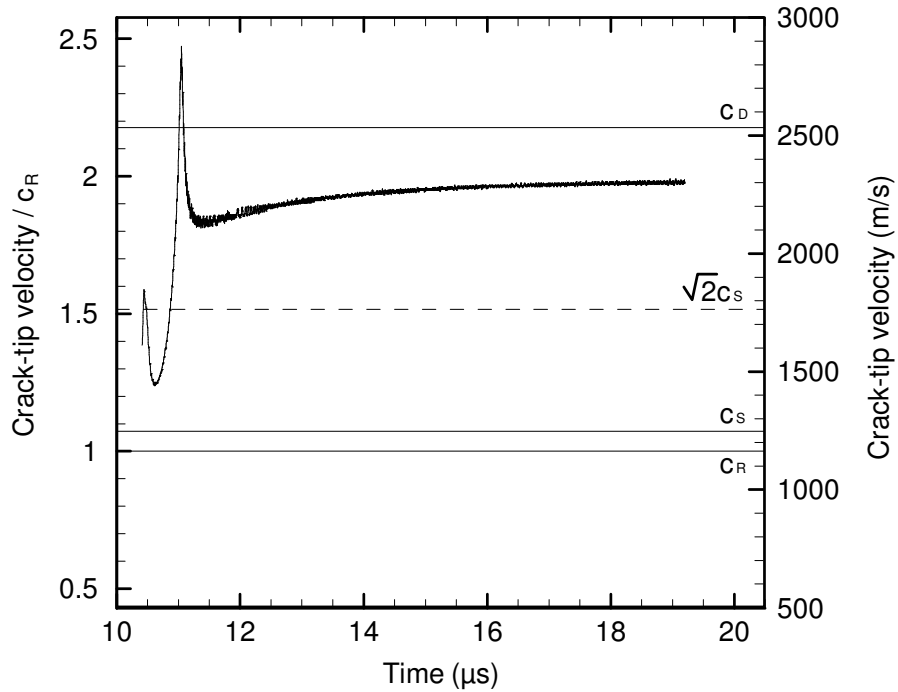


Figure 3.8: Plot of normalized (with $c_R$) crack-tip velocity with time for $V_{imp} = 30$ m/s

where $\beta$ is the angle made by the shear shock wave with the horizontal interface on the trailing side of the crack-tip and $v_c$ is the crack-tip velocity.

The crack-tip position as a function of time is shown in Fig. 3.7. The crack-tip is defined as the farthest point from the initial crack-tip where the displacement jump is $5\delta_t$. This corresponds to ~ 100 % of cohesive energy dissipated in the resulting cohesive zone. The crack-tip velocity history is shown in Fig. 3.8 and is presented in terms of the non-dimensional parameter $v_c/c_R$, where $c_R$ is the Rayleigh wave speed. The crack-tip velocity at a particular time is obtained by the slope of the crack-tip history using the least square fitting of a straight line over 31 consecutive crack-tip positions. These calculations of $v_c$ are conversant with those obtained from the shear shock angle using Eqn. (3.4). The crack-tip starts accelerating from time ~ 10.75 µs to ~ 11.5 µs. Correspondingly, the calculated crack-tip velocity increases transiently from sub-Rayleigh velocity to a velocity above the dilatational wave speed before settling down to a sustained intersonic speed of 2302 m/s (or $1.977 c_R$). This is facilitated by the formation of a microcrack at some distance ahead of the main crack followed by coalescence of the main crack with the microcrack (also called daughter-crack). This phenomenon, known as the Burridge-Andrews mechanism (after Burridge, 1973; Andrews, 1976), has been observed in the finite-element simulations by Needleman (1999) and in the experiments by Xia *et al.* (2004) for homogeneous materials as well as in the simulations in bimaterials by Coker *et al.* (2003). Through this mechanism, cracks transiently jump from sub-Rayleigh to intersonic speed regime without going through the forbidden region

between the Rayleigh wave speed and the shear wave speed. This mechanism will be discussed in detail in Section 3.6.

3.5.2    Convergence Study

In this study, the governing equations of MPM [Eqn. (3.7)] are solved on the background mesh. The effect of mesh size on the sustained crack-tip velocity and cohesive forces on interface nodes in both tangential and normal directions are investigated. Mesh is refined by a factor of two where the smallest mesh cell-length is varied from 1 mm to 31.25 µm. The crack-tip positions as a function of time for different mesh sizes are shown in Fig. 3.9, for $V_{imp}$ = 30 m/s and a cohesive strength of 24 MPa. The difference in the crack-tip position history for different mesh sizes is negligible.

We next examine the mesh convergence by plotting the normalized (with $c_R$) crack-tip velocities for different mesh sizes as shown in Fig. 3.10. As the mesh size is decreased from 1 mm to 62.5 µm, the transition from sub-Rayleigh to intersonic speeds becomes more abrupt. For the portion of the curves prior to 12 µs in Fig. 3.10, convergence was not attained for different mesh sizes because it is during this time interval that the transition mechanism from sub-Rayleigh to intersonic speed regime occurs aided by the formation of a microrupture (daughter-crack tip) ahead of the mother-crack tip.

Further, depending on the mesh size and how accurately the daughter-crack tip can be resolved, the crack-tip position and velocity histories at or near this transition mechanism changes with larger mesh sizes tending to average the position and velocity, respectively. Even though the velocity history plots show crack propagation through the forbidden zone, it is an artifact of poor grid resolution. At the smallest mesh size of 31.25 µm, an

overshoot of the velocity to supersonic speed was observed. It may be noted that this is an artifact, the result of calculation of the velocity from the crack-tip position.
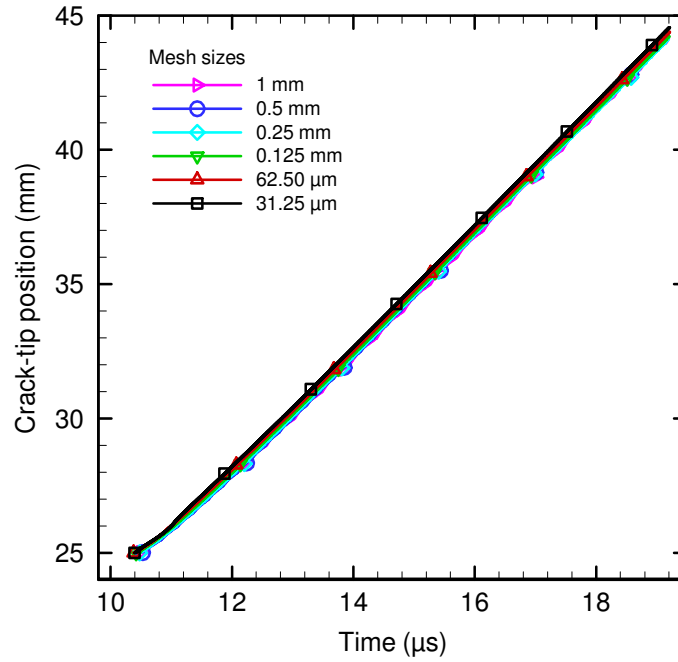


Figure 3.9: Variation of crack-tip position with time for different mesh sizes
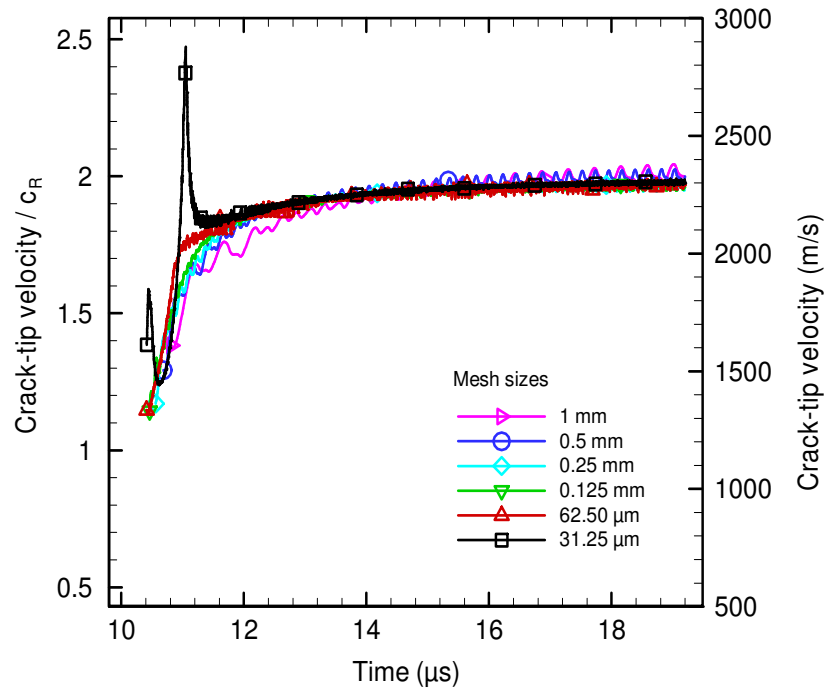


Figure 3.10: Plot of normalized (with $c_R$) crack-tip velocity with time for different mesh sizes for $V_{imp} = 30$ m/s
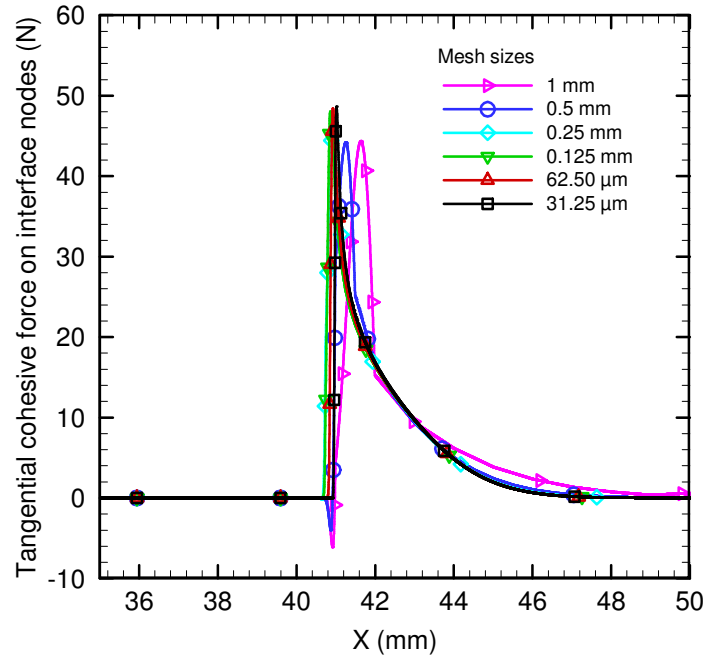
Figure 3.11 (a): Tangential cohesive force ($T_t$ integrated over cohesive segments) on the upper interface for $V_{imp}$ = 30 m/s at $t$ = 17.6 µs
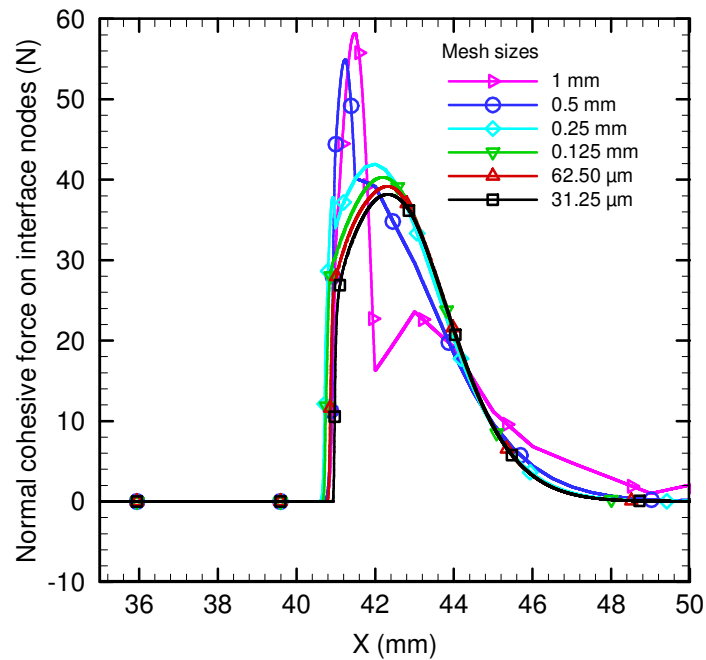


Figure 3.11 (b): Normal cohesive force ($T_n$ integrated over cohesive segments) on the upper interface for $V_{imp}$ = 30 m/s at $t$ = 17.6 µs
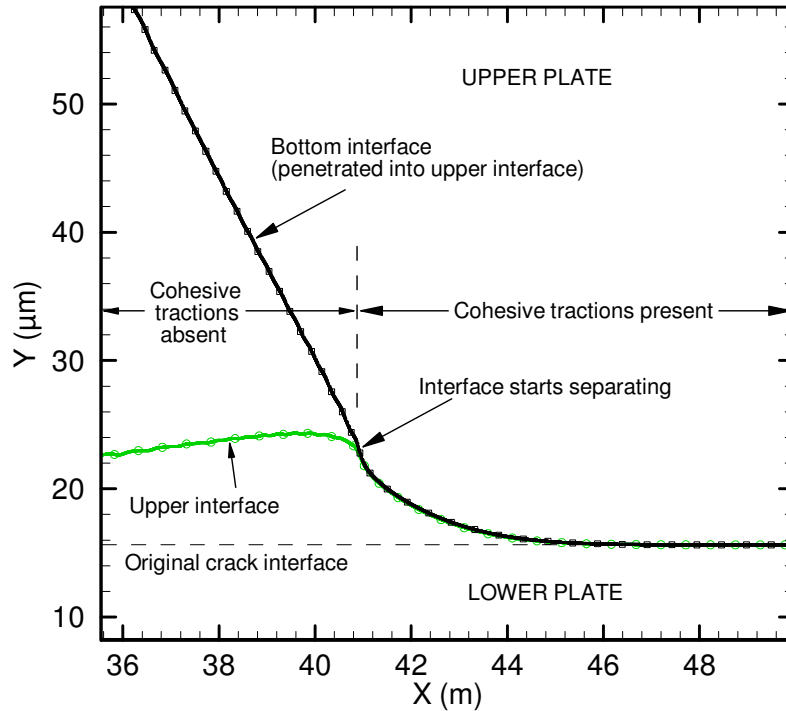
Figure 3.11 (c): Interface surface profiles for $V_{imp}$ = 30 m/s with a cell length of 31.25 µm and $t$ = 17.6 µs

When a daughter-crack is formed ahead of the main-crack, the crack-tip algorithm identifies wrongly the new crack-tip as the location of the newly formed daughter-crack. This feature is not captured by the coarser mesh sizes. However, in all cases, the same sustained crack-tip velocity is reached at 2300 m/s (or ~ 1.977 $c_R$). The coarser mesh sizes result in oscillations around this value. There is also a good agreement for all mesh sizes for the time at which crack initiation occurs (~ 10.4 µs).

For all mesh sizes, the shear and normal cohesive forces at the nodes along the interface are plotted in Fig. 3.11 at $t$ = 17.6 µs. The crack-tip is located at ~ 41 mm and both the shear and normal forces increase as the crack-tip is approached from the right and drops to zero when separation occurs. In the case of Fig. 3.11 (a), the values of the forces over the interface have a tendency to close the interface in the shear direction. In

the case of Fig. 3.11 (b), the nature of normal forces is compressive. In other words, the values of the forces over the interface have a tendency of interface opening in the normal direction due to bottom surface having a tendency of pressing onto the upper surface, due to Poisson's effect. This is illustrated by plotting interface surface profiles in Fig. 3.11 (c). In Figs. 3.11 (a) and (b), for the finer mesh sizes, the cohesive region size is equal ~ 7 mm, which is defined by 224 background mesh elements and 3360 cohesive segments. From these results it is reasonable to conclude that mesh convergence is attained for element size of 62.5 µm; to resolve the highly transient Burridge-Andrews mechanism, we investigated using a finer mesh size (31.25 µm) for $V_{imp} = 30$ m/s.

## 3.6 Discussion

The effect of the impact speed on the crack-tip velocities was studied by varying the impact speeds from 5 to 60 m/s. The normal and shear cohesive strengths of 24 MPa were used at the interface. Normalized crack-tip velocity histories for all cases are shown in Fig. 3.12 (a). A mesh size of 31.25 µm was used for $V_{imp}$ of 20 m/s and above. However, a mesh size of 62.5 µm was adopted for $V_{imp} \leq 10$ m/s because of the occurrence of a numerical instability during the formation of a microcrack, as a result of which the simulation quit.

A more detailed discussion pertaining to this issue is given in the latter part of this section. For $V_{imp} < 9.4$ m/s, the crack propagates at a velocity less than the Rayleigh wave speed of the Homalite. As the impact speed is increased (starting from 5 m/s), the crack-tip velocity approaches $c_R$ earlier in time. As the crack-tip velocity approaches $c_R$ with increasing impact speed, the crack either crosses $c_R$ and enters the intersonic regime ($V_{imp} > 9.4$ m/s) or it oscillates at values lower than $c_R$ (for $V_{imp} < 9.4$ m/s).
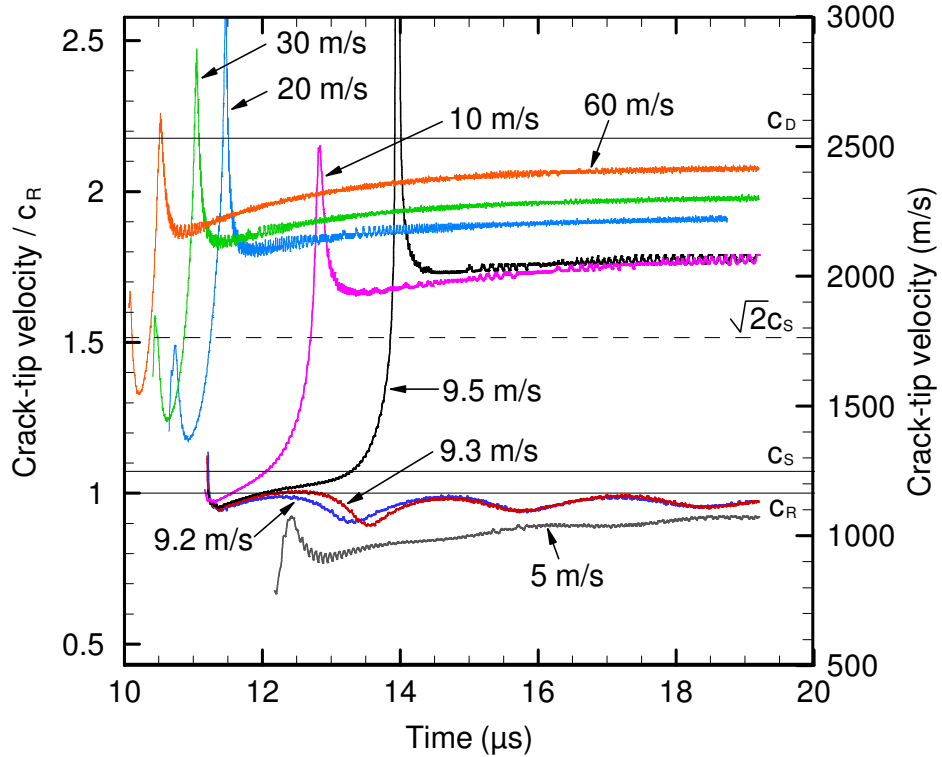
Figure 3.12 (a): Variation of the normalized (with $c_R$) crack-tip velocity with time for various impact speeds, considering cohesive strength of 24 MPa and plate modulus, $E$ of 5.2 GPa

In this latter case of sub-Rayleigh crack propagation, the crack-tip velocity approaches $c_R$ with time and the oscillations (maximum amplitude of ~ 40 m/s) decreases. The sustained crack-tip velocity is taken as the peak of the oscillating values. For the case of $V_{imp} > 9.4$ m/s, the sustained crack-tip velocity (at time ~ 19.2 μs, which more or less remains at a constant value with time) is found to be in the region between $\sqrt{2}\,c_S$ and $c_D$. Further, as the impact speed is increased, the transition Burridge-Andrews mechanism occurs earlier in time.

The transition of sustained crack-tip velocity from sub-Rayleigh to intersonic, with increasing impact speed is abrupt and occurs at $V_{imp} \approx 9.5$ m/s. This abrupt change can be seen in Fig. 3.12 (b) where the sustained crack-tip velocity is plotted as a function of the

41
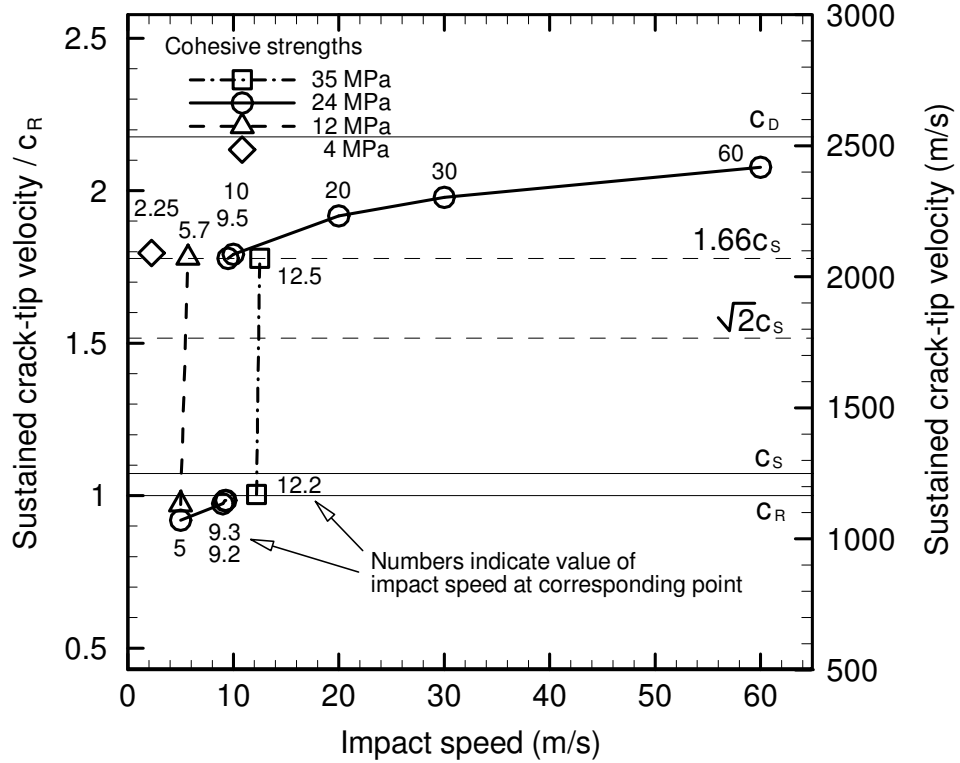
Figure 3.12 (b): Variation of normalized (with $c_R$) sustained crack-tip velocity for various impact speeds and cohesive strengths, for plate modulus, $E$ of 5.2 GPa

impact speed. The corresponding lowest value of the sustained crack-tip velocity in the intersonic regime is called the transition crack-tip velocity (Burridge *et al.* 1979) which, from our simulations is ~ 1.66 $c_S$. Thus, in all these cases, there was no steady-state crack-tip velocity observed between $c_R$ and $\sqrt{2}\,c_S$ which is consistent with the finite energy arguments of Freund (1979) and Rosakis *et al.* (1999). However, in our case, with the cohesive parameters selected ($\sigma_{max} = \tau_{max} = 24$ MPa), no sustained crack-tip velocity was observed between $\sqrt{2}\ c_S$ and 1.66 $c_S$ either. This result may be consistent with the analysis of Burridge *et al.* (1979) on the crack propagation under a step impact loading. In their analysis, Burridge *et al.* reported that for constant shear loading at a distance $d$ from the crack-tip, the transition crack-tip velocity of $\sqrt{2}\ c_S$ will occur only for very high

values (up to infinity) of distances, $d$, of the crack-tip from the point of load and that the transition crack-tip velocity increases as $d$ decreases. However, in similar simulations carried out by Needleman (1999) using FEM, he reported that by changing the pulse duration time (as well as cohesive strengths) he obtained crack propagation with velocities close to $\sqrt{2}\,c_S$. Thus, the lowest attainable stable intersonic crack-tip velocity of $\sqrt{2}\,c_S$ can still occur under such situations as reported by Burridge *et al.* (1979) (analytical work) and Rosakis *et al.* (1999) (experiments).

In our simulations, we used pulse duration time of 15 µs, and cohesive strength of 24 MPa, while in Needleman's simulations (1999) the time duration was 1 µs and the cohesive strength was 30 MPa, in which case Needleman observed sustained intersonic crack-tip velocity of $\sqrt{2}\,c_S$. In our simulations it might be possible that the lowest sustained crack-tip velocity could reach $\sqrt{2}\,c_S$, if the pulse duration time were reduced, or if the crack were allowed to propagate over a longer length. We further investigated the effects of cohesive strength of the interface and Young's modulus of the bulk material on the value of transition crack-tip velocity. Cohesive strength was varied from 4 to 35 MPa. Fig. 3.12 (b) shows the transition speed as a function of impact speed for cohesive strengths of 4, 12, 24, and 35 MPa. The transition speed remains at a constant value of ~ 1.66 $c_S$, independent of the cohesive strength. This transition speed is reached at impact speeds of 2.25, 5.7, 9.5, and 12.5 m/s, and for cohesive strengths of 4, 12, 24, and 35 MPa, respectively. Thus for the cases studied in our simulations the lowest sustainable crack-tip velocity in intersonic region was 1.66 $c_S$. Lastly, from Fig. 3.12 (b) we can also see that as the impact speed is increased, the sustained intersonic crack-tip velocity increases from 1.66 $c_S$ (or 0.82 $c_D$) to 1.94 $c_S$ (or 0.95 $c_D$) and tends to approach $c_D$ at a

decreasing rate with respect to the impact speed. Fig. 3.13 shows the normalized crack-tip velocity history plots for impact speeds corresponding to relatively lower Young's modulus of the plate ($E = 3$ GPa, $\nu = 0.34$) and cohesive strength of 4 MPa. It can be seen that the transition speed value remains more or less the same ($\sim 1.66\ c_S$) corresponding to an impact speed of 4 m/s.
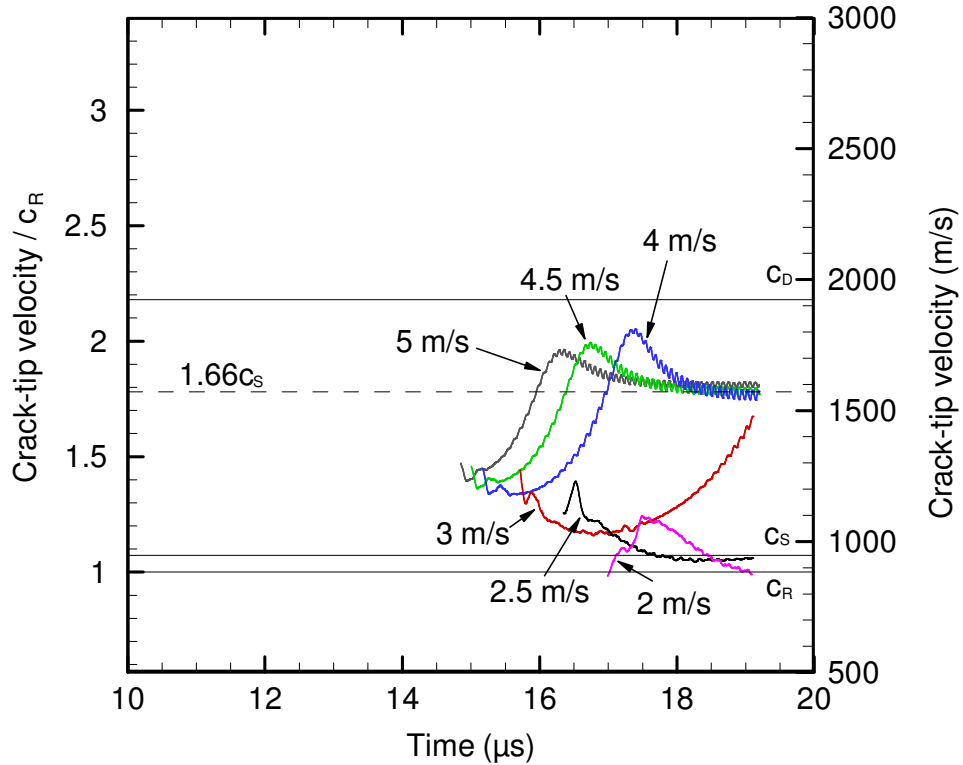


Figure 3.13: Variation of normalized (with $c_R = 883$ m/s) crack-tip velocity with time for various impact speeds, considering cohesive strength of 24 MPa and plate modulus, $E$ of 3 GPa

Next, simulations are conducted for an impact speed of $V_{imp} = 10$ m/s with cohesive strengths, $\sigma_{max} = \tau_{max} = 24$ MPa, and background mesh size of 62.5 µm, to observe the Burridge-Andrews mechanism. Figs. 3.14 (a) to (d) show sequential plots of maximum shear stress contours showing the transition mechanism. In Fig. 3.14 (a) only a single crack-tip can be seen (see black arrow) propagating at a velocity below the Rayleigh

wave speed. In Fig. 3.14 (b) a microrupture or a daughter-crack is formed ahead of the trailing mother-crack–tip as indicated by a white hollow arrow-head. The criterion used for the formation of the daughter-crack tip should be the same as that used for the main crack-tip, namely, when the displacement reaches a critical value of $5\delta_t$ ($\delta_t$ is the characteristic length corresponding to the cohesive surface in the tangential direction) the crack-tip is formed. However, in our simulations the daughter-crack was not fully developed at fine background mesh size (31.25 µm) as the simulation quit. We had to use a coarser mesh size (62.5 µm) so that the simulation could continue to run. However, at this coarser background mesh size, the crack-tip displacements in shear were unable to reach the value of $5\delta_t$ due to the effect of mesh averaging, so that the daughter-crack tip could not be recognized in this way. As a result, the initiation of the daughter-crack was determined approximately through the observation of the stress contour at a small distance ahead of the major crack-tip and from the jump in the velocity history plot [Fig. 3.12 (a)]. The mother-crack-tip then accelerates rapidly [Fig. 3.14 (c)] and joins the daughter-crack-tip as shown in Fig. 3.14 (d). It is during this process that the apparent crack-tip velocity increases abruptly to and above the dilatational wave speed. From this point, shear shock waves start developing from the crack-tip and after some time, the crack-tip velocity reaches a sustained value in the intersonic region.

This mother-daughter-crack transition mechanism has been explained theoretically by Broberg (1989) using the steady state analysis. In that work, Broberg pointed out that the crack-tip cannot travel steadily between $c_R$ and $c_S$ due to violation of the energy considerations. The accelerating crack-tip thus goes through a transition mechanism so as to pass from sub-Rayleigh to intersonic regime to avoid the forbidden region.
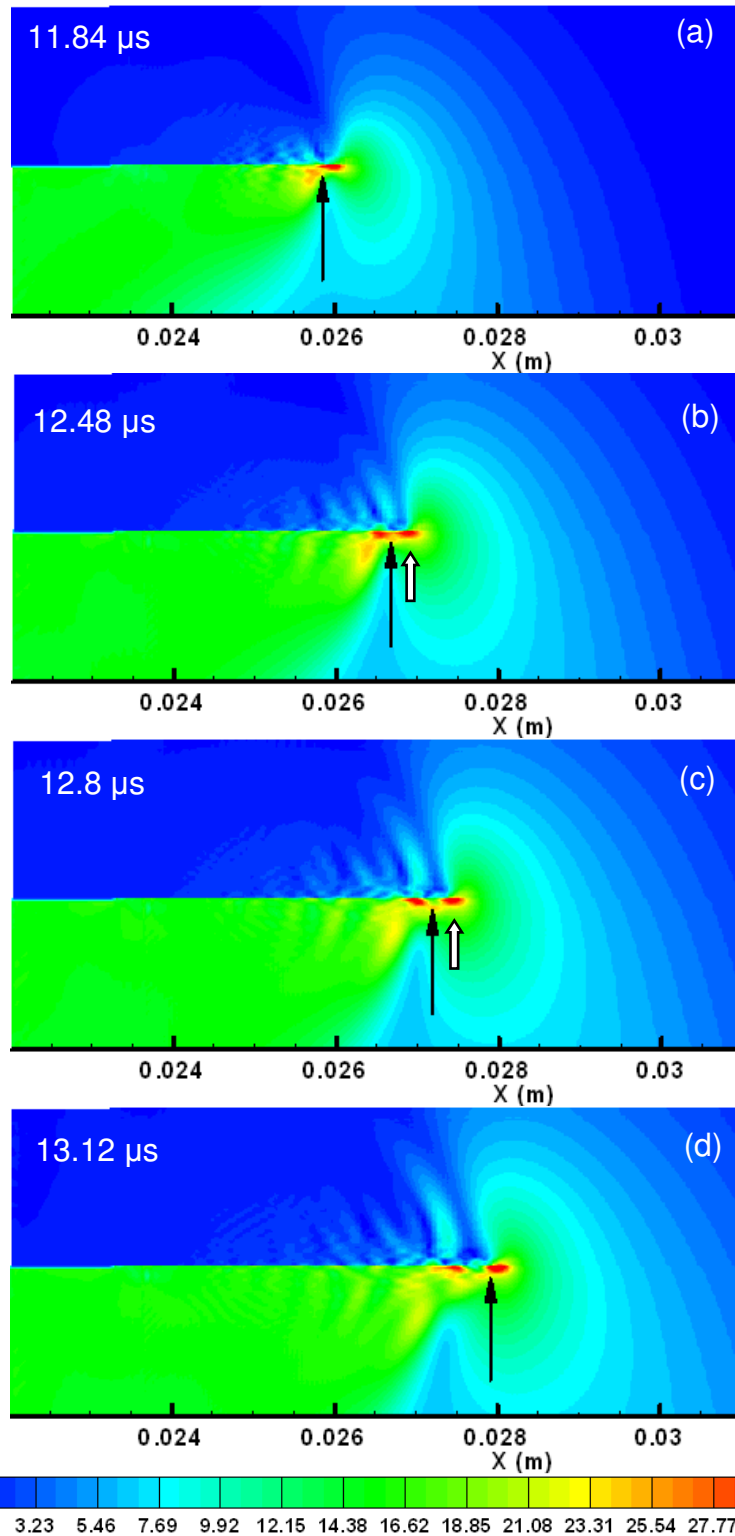
Figure 3.14: Snapshots of $\tau_{max}$ (MPa) for $V_{imp} = 10$ m/s (a) Main crack-tip propagation at a sub-Rayleigh wave speed, (b) Formation of microrupture ahead of the main crack-tip, (c) Coalescence of main crack-tip with microrupture, (d) Resultant crack-tip propagation at intersonic wave speed.

This transition mechanism is called the Burridge-Andrews or the mother-daughter crack mechanism.

In all the simulations conducted in this investigation of varying mesh sizes and impact speeds, we observed that even though mesh convergence may have been attained (based on the above considerations) identifying the mother-daughter (Burridge-Andrews) transition mechanism requires finer mesh sizes in order to observe an abrupt increase in the crack position history. However, for the case $V_{imp}$ = 10 m/s, we observed that the finest mesh size (cell-length of 31.25 µm) is limited by the instability in the simulation occurring during Burridge-Andrews transition mechanism after which simulation would quit. Fig. 3.15 shows the results obtained with a cell-length of 31.25 µm and $V_{imp}$ of 10 m/s. Fig. 3.15 (a) shows the distinct jump in the crack position history which is also the point where instability occurs. Fig. 3.15 (b) shows the corresponding plot of maximum shear stress contour at time 16.96 µs, just before the simulation quits. This instability, at the point where microcrack (daughter-crack) nucleates, could be attributed to elastic snap-back instability (Gao and Bower, 2004) occurring when the stress reaches the peak strength of the interface. The mesh size required to resolve the daughter-crack is different (less) than that required to obtain converged sustained crack-tip velocities, since daughter-crack formation occurs at a relatively smaller scale than the major (mother) crack with respect to the size of their cohesive zones. In our investigation, we have checked for convergence of the major crack-tip cohesive zone and not for daughter-crack tip cohesive zone. For potential intersonic cracks, depending on the mesh size and impact speeds, the daughter-crack tip cohesive zone is resolved to a certain level. The daughter-crack is better resolved at lower impact speeds, if we keep the mesh size the same at all

47

impact speeds. One such simulation at which we were able to resolve the daughter-crack (resolve the actual distance between the daughter-crack and major crack in conjunction with crack opening displacements) is at 10 m/s impact speed and 31.25 µm mesh size at which we observed the sharp jump (discontinuity) in the crack-tip position history instead of continuous increase, as in other cases of higher impact speeds.
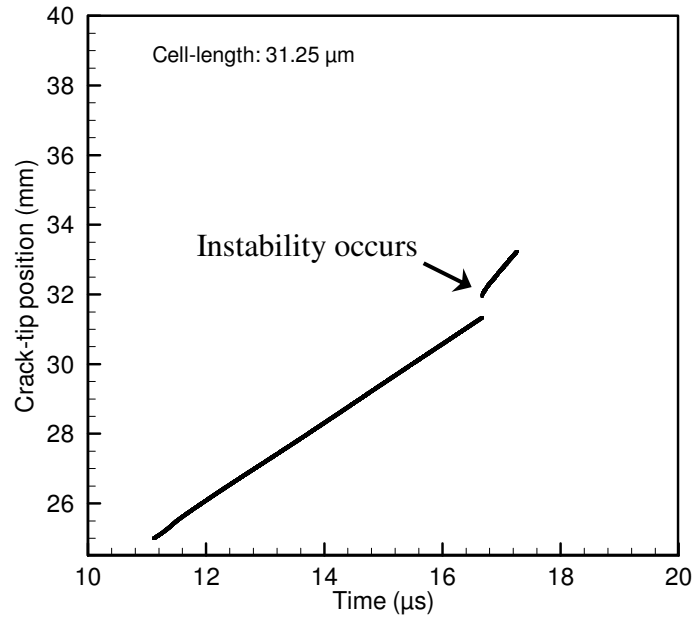


(a) Crack-tip position history
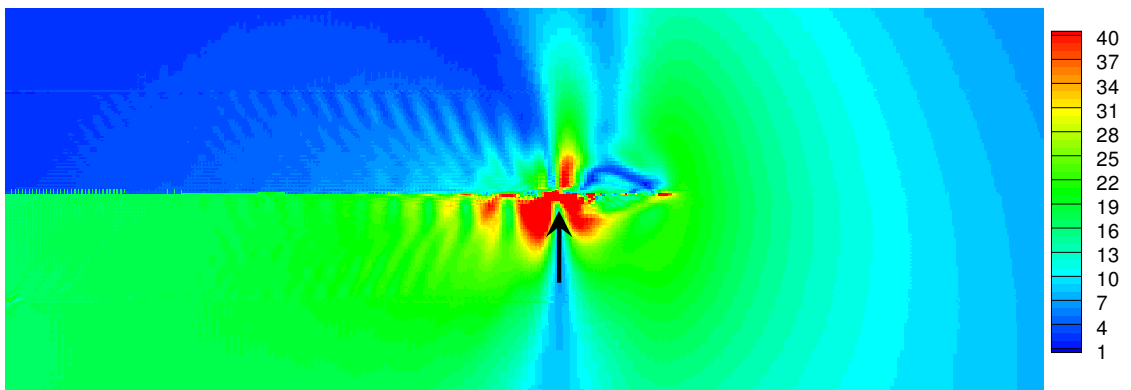


(b) Snapshot of $\tau_{max}$ (MPa) at time 16.96 µs

Figure 3.15: Results for $V_{imp} = 10$ m/s with cell-length of 31.25 µm, showing instability.

It is for this unique case (in our work) that the nucleation of daughter-crack was resolved. However, during nucleation, the simulation ran for some time and quit due to cohesive forces reaching very high values. Gao and Bower (2004) had observed a similar pathology in their simulations. In their work, they reported that by introducing a viscosity term in the constitutive equations for the cohesive law they were able to suppress the instability during crack nucleation and thus allow simulation to go further.

In our case, we simulated the results [Fig. 3.12 (a)] for the case of $V_{imp}$ = 10 m/s with the mesh size (cell-length of 62.5 µm) one level coarser than the one in which simulation becomes unstable (cell-length of 31.25 µm). However, this mesh size could not resolve the distinct jump near the crack-tip that otherwise propagates at the same sustained crack-tip velocity. Thus, we found mesh size of 31.25 µm to be appropriate for $V_{imp}$ of 20 m/s and above, while a mesh size of 62.5 µm for $V_{imp}$ of 10 m/s and below.

Our simulation results obtained for the case of $V_{imp}$ = 10 m/s with cohesive strengths, $\sigma_{max}$ = $\tau_{max}$ = 24 MPa, and background mesh size of 62.5 µm are compared qualitatively with the isochromatic fringe patterns obtained from experiments using photoelasticity by Rosakis *et al.* (1999), in Fig. 3.16. The general shape of the isochromatic patterns in front of the crack-tip matches with the experimental results of Rosakis *et al.* (1999), as shown in Fig. 3.16 (b) (from Rosakis *et al.*, 2000); and theoretical predictions based on a Dugdale type cohesive zone model, as shown in Fig. 3.16 (c) (from Rosakis *et al.*, 2000). It is somewhat difficult to compare the patterns quantitatively due to difficulty in extracting stress values from the fringe patterns obtained in the experiments. Furthermore, the velocity of the crack-tip is 1.66 $c_S$ for the numerical pattern and 1.47 $c_S$ for the experimental pattern. This can also be seen from the angles formed by the shear shock

waves; in the simulation the value is 37° and in the experiments it is 43°. Finally, due to the absence of contact algorithm in the numerical simulation model, we see complex stress patterns corresponding to waves traveling over the trailing crack surfaces, which are not exactly comparable with experiments.
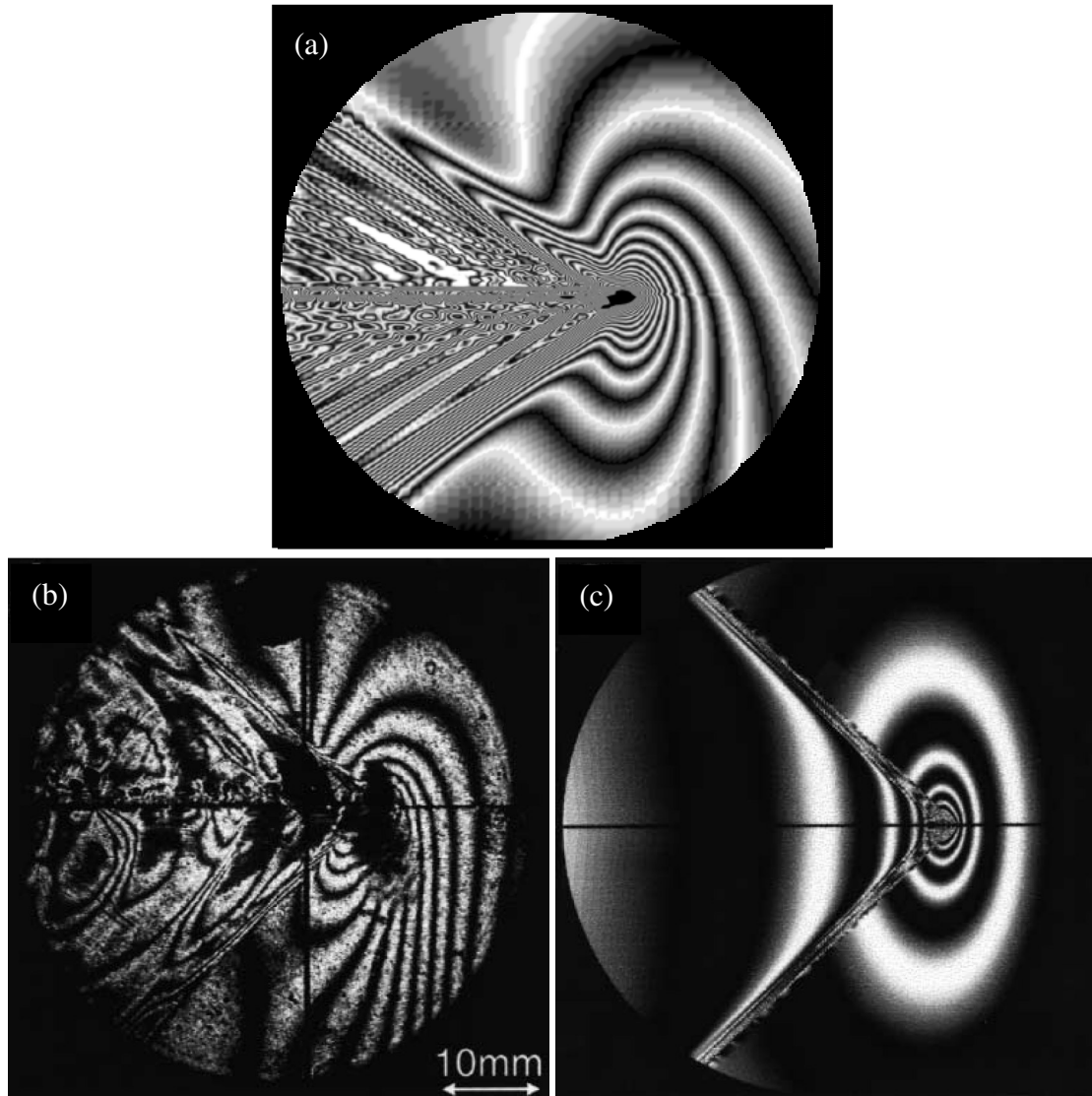


Figure 3.16: Views of (a) Simulated result showing maximum shear stress for $V_{imp} = 10$ m/s and $\sigma_{max} = \tau_{max} = 24$ MPa, compared with (b) experimental pattern, (c) theoretical predictions based on a Dugdale type cohesive zone model (after Rosakis *et al.* 2000).

From this, it appears that in actual experiments the crack surface contact plays some role and it could even influence the stress contours trailing the crack-tip.

It may be noted that numerical implementation of the normal cohesive law has to take into consideration the possibility of interpenetration of crack surfaces. Interpenetration in the cohesive zone has been prevented by the use of steep slope of the traction-displacement cohesive law in the case of negative (relative) displacements. The current simulation has taken this into consideration and prevented penetration of material points in the cohesive zone. In the wake of the crack-tip, where the cohesive law is turned off (due to difficulty associated with searching cohesive nodes within each cell, as a result of relatively large displacements at crack surfaces), algorithm has not been implemented to prevent interpenetration of the crack faces even if the displacements are negative. Based on published results (more details to follow), it is seen that the stress field in front of the crack-tip should not be affected by the interpenetration behind the crack-tip because the behavior of the crack-tip is governed by the asymptotic stress field around the crack-tip. It may be noted that the present work has focused on the stress-field in front of the crack-tip. Comparisons between experiments and finite element simulations (Needleman, 1999; Rosakis *et al.*, 1999, 2000; Coker *et al.*, 2003; Yu *et al.*, 2002) imply that the crack behavior for shear-dominated crack growth is not affected by the particular behavior in the wake of the crack-tip. In the FEM work cited by Needleman (1999) and Coker *et al.* (2003), the interpenetration was allowed and frictional contact was not considered in the wake of the crack-tip. In the 3D FEM work by Yu *et al.* (2002), the frictional contact was considered in the wake of the crack-tip. In all these cited FEM work, results were compared with experimental results by Rosakis *et al.* (1999, 2000). In the experiments,

interpenetration did not occur and frictional contact was present. Despite the differences in the conditions in the wake of crack-tip between FEM simulations, the global behavior (crack-tip speed) and the local behavior (fringe patterns in front of the crack-tip) showed good agreement between experiments (where there is contact and frictional sliding of the crack faces) and simulations. In this work, we have focused on implementing the cohesive zone model and did not implement the contact algorithm to prevent interpenetration behind the crack-tip because we are interested primarily in the crack-tip behavior.

Some discrepancy can be seen between the simulated crack initiation time and the experimental values, with the experimental values being slightly higher. This can be attributed to the geometry of the initial crack-tip, which is mathematically sharp in the case of simulations but not so in experiments. There is also a possibility that some of the impact energy may be consumed in material nonlinearities not considered in the numerical model. Further, since the sustained crack velocities in the experiments are lower than that of the numerical simulations, for relatively higher impact speeds, it is possible that the actual bonding strength might be higher than the cohesive strength used in the simulations. Overall, the combined MPM and cohesive zone model methodology are able to capture the salient features of the dynamic crack growth.

3.7 Conclusions

Cohesive zone model was implemented in MPM to simulate dynamic crack propagation. Dynamic crack growth was investigated by numerical simulations of shear dominated crack growth in a nominally brittle, homogeneous, linear-elastic solid under

plane strain conditions with the crack constrained to grow in the direction of the initial notch. Based on dynamic crack growth simulation results, the following conclusions are reached:

1. Dynamic crack propagation occurs in both sub-Rayleigh and intersonic crack-tip velocity regimes. A potential intersonic crack, after initiating, accelerates and experiences crack-tip velocities close to the Rayleigh wave speed. In order for the crack-tip velocity to increase from sub-Rayleigh to intersonic regime, it goes through a transition Burridge-Andrews mechanism, namely, formation of a microcrack at some distance ahead of the main crack, and coalescence of the main crack with the microcrack, after which it reaches a stable state of crack propagation.

2. Mesh convergence study was carried out by varying the smallest element size from 1 mm to 31.25 µm. There was a good agreement for the sustained crack-tip velocity and cohesive force distribution over the interface for 62.5 µm and 31.25 µm mesh sizes. However, the sub-Rayleigh to intersonic speed transition mechanism is only captured by the smallest mesh size of 31.25 µm used in the investigation.

3. The effect of impact speed was investigated for impact speeds ranging from 5 to 60 m/s. For a fixed set of cohesive properties, sustained crack-tip velocities increasing from sub-Rayleigh wave speeds to longitudinal wave speeds with increasing impact speed were obtained. In the case of crack propagation in the sub-Rayleigh regime, as the impact speed was increased sustained crack-tip velocities increased and approached the Rayleigh wave speed. In the case of crack

propagation in the intersonic regime, for the cases simulated, sustained crack-tip velocities were obtained in the region between 1.66 $c_S$ (or 0.82 $c_D$) and 1.94 $c_S$ (or 0.95 $c_D$), with 1.66 $c_S$ as the lowest intersonic crack-tip velocity obtained in simulation. The lowest crack-tip velocity obtained in these simulations did not reach $\sqrt{2}\,c_S$ as reported from the analytical work by Burridge *et al.* (1979), experiments by Rosakis *et al.* (1999), and FEM simulations by Needleman (1999). Further, in our simulations, as the impact speed was increased, the sustained crack-tip velocity increased at a decreasing rate with respect to the impact speed.

4. A transition crack-tip velocity of 1.66 $c_S$ was observed, which remained the same (for simulations in this work) for different cohesive strengths of 4, 12, 24, and 35 MPa (for both shear and normal strengths) and corresponding impact speeds of 2.25, 5.7, 9.5, and 12.5 m/s.


Good qualitative agreement was observed between the numerical results presented here and the experimental results of Rosakis *et al.* (1999) in terms of the photoelastic stress patterns ahead of the crack-tip.

CHAPTER IV

SIMULATION OF MICROSTRUCTURE EVOLUTION OF A CLOSED-CELL

POLYMER FOAM IN COMPRESSION

4.1   Introduction

Polymer foams have been of particular interest in many applications due to their low

thermal conductivity, high specific strength, high specific energy absorption, and high

acoustic damping than continuous material. Introduction of voids leads to very low

density, on the order of 0.1 $g/cm^3$ for the polymethacrylimide (PMI) or Rohacell foam,

allowing control over homogenous stiffness, strength, and energy absorption properties.

It is currently used as cores for composite sandwich structures used in launch rocket,

missile shells, military helicopter blades, and other energy absorbing packaging

applications.

The Rohacell foam is a closed-cell foam. A typical stress-strain curve for such foams

in compression is characterized by three regions (Gibson and Ashby, 1997). An initial

(nearly) linear elastic region occurs at low stress. The stress experienced in this region is

due to cell-walls bending, stretching or contracting. The elastic region is followed by a

long collapse plateau region or compaction region in which cells collapse by buckling,

bending and fracture. In some foams, such as ductile metallic foams, yielding is

experienced due to formation of hinges (Gibson and Ashby, 1997). In the third region,

densification occurs in which almost all the voids collapse and disappear; as a result the neighboring cell-walls are compressed against each other, leading to stiffening in material response. Before the plateau region, a yielding portion is observed which may or may not show a drop in the stress as the strain increases. The mechanical properties of such foams depend on material properties of the solid cell-walls and the microstructure of the foam. It may be noted that the cell-wall properties can be different from those of the monolith or bulk material due to size effect and processing conditions.

Typically, modeling of foams through microstructure can be used to serve the following purposes (Bardenhagen *et al.* 2005; Brydon *et al.* 2005):

(a) Optimization of overall foam mechanical properties which depend on the microstructure and properties of the parent material.

(b) Predicting unit cell, representative volume element, or parent material properties. Particular examples where this can be useful are where such unit-cell properties cannot be directly measured, for example in nanofoams such as cross-linked aerogels (Katti *et al.* 2006; Leventis *et al.* 2007, 2008; Luo *et al.* 2006).

(c) Identify deformation mechanisms for development of phenomenological or constitutive models, considering the microstructural evolution during deformation.

While work has been conducted in using the material point method (MPM) to simulate deformation of open-celled foams (Bardenhagen *et al.* 2005; Brydon *et al.* 2005), there is essentially no work reported using MPM to simulate closed-cell foams. In this part of the work, the material point method is used to model deformation of closed-cell foams. Analysis of the foam by $\mu$-CT provided the microstructure input to the MPM model. In addition, the simulation results were qualitatively compared with in-situ $\mu$-CTs

of the microstructural evolution during deformation along with the compressive stress-strain curve. Attention is focused on the deformation mechanisms in closed-cell foams such as initiation of collapse, formation of shear bands, and representative volume element for such foams.

4.2  Background

In simulations on the response of foams under compression, phenomenological approach is often used. In this approach, an equivalent constitutive law for the foam modeled as a homogeneous material is used. Although phenomenological models in the form of power-law relationships exist for both Young's modulus and strength of foams with mass density of foams (Gibson and Ashby, 1997), those models do not explicitly address the relationship between microstructure and macroscopic properties; hence their value in guiding the design of the microstructures is limited. However, simulations of complex foam microstructures in compression have always been a challenge due to the large distortions involved and extensive contact of the cell-walls. This is particularly true in the simulation of the compaction and densification regions of the stress-strain curves where large deformations and rotations occur, which require efficient handling of the contact between cell-walls. To date, major efforts have been focused on finding analytical solutions.

MPM can handle, relatively easily, the modeling of realistic microstructures of foams and multiphase materials. In the case where the material points move in a single-valued velocity field, no-slip contact between the surfaces can be handled automatically. Bardenhagen *et al.*, (2005) demonstrated the advantage of this numerical method in

57

compression simulations of open-celled foam structure, with large material deformations over a full range of densification up to 90% compressive strain. They determined the 3D geometry using μ-CT and passed the information on to the MPM to build a discretized model using material points. They demonstrated the dependence of stress-strain curves in compression on microstructure irregularity and its material properties. A separate meshing requirement of such complex structure was eliminated with the use of the particle representation of the microstructure. They reported that, the presence of residual porosity (porosity at a particular strain after compression) needs to be considered for evaluating dynamic material response of such materials. Brydon *et al.* (2005) simulated quasi-static densification of polyurethane (polymeric) open-cell foams assuming elastic properties for the parent material and using no-slip contact. A representative volume element was used to represent the bulk response, dynamic effects, and microstructure evolution during deformation. In another case, Nairn (2006) used information from a scanning electron micrograph of wood and carried out two-dimensional MPM simulations of transverse compressions and densifications in softwood and hardwood. He reported that he was able to reproduce many features of wood under compression.

In this study, we have carried out compression experiments on closed-cell PMI (Rohacell) foam and observed the foam in compression, undergoing elastic, compaction, and densification stages of deformation using μ-CT. A customized load frame allowed for simultaneous real-time compression, over 360º observations using X-rays, and recording the *in-situ* microstructure evolution (Hanan *et al.* 2007). In addition, the undeformed three-dimensional image reconstructed from the μ-CT data was converted into material points for simulation using the MPM. We used the MPM originally

developed by Sulsky *et al.* (1995), with $C^1$ continuous shape functions (Bardenhagen and Kober, 2004). Direct measurement of cell-wall moduli using conventional testing techniques such as tensile or bending tests is difficult due to the small size of the cell-walls and variation observed in cross-sectional area along the length. Hence, nanoindentation tests were carried out to determine the material properties of the solid polymer. These material properties along with appropriate constitutive model for the material points were used as input in the MPM simulation. The numerical output from MPM includes snapshots of the 3D deformed configurations as well as the stress-strain curve. These are compared qualitatively with the deformation observed under *in-situ* µ-CT.

## 4.3   Methodology

### 4.3.1   Compression of PMI foam with *in-situ* micro-computed tomography

Rohacell closed-cell foam samples were manufactured by Degussa. The parent (or cell-wall) material is polymethacrylimide (PMI). Such foams are typically manufactured by hot forming of methacrylic acid/methacrylonitrile copolymer followed by curing, which generally improves its mechanical properties. During foaming, this copolymer is converted to polymethacrylimide. The samples used for compression and µ-CT imaging were cylinders of 5 mm diameter and 5 mm height. Another set of samples were cut in a cube shape with side length of 12.7 mm and were used for confirming the stress-strain curve. Samples of required dimensions were cut without the use of lubricants. The samples were kept inside a sealed envelope with aluminum foil liner before testing to protect from UV light exposure and moisture.

Micro-Computed Tomography (μ-CT) images were obtained with a Scanco μCT-40. For *in-situ* observation, μ-CT was obtained at Argonne National Laboratory's Photon Source synchrotron facility. However, the radiographs included significant phase contrast, which upon reconstruction for μ-CT showed too much noise to directly generate an MPM model but the *in-situ* tomography was used to qualitatively compare with simulation results.
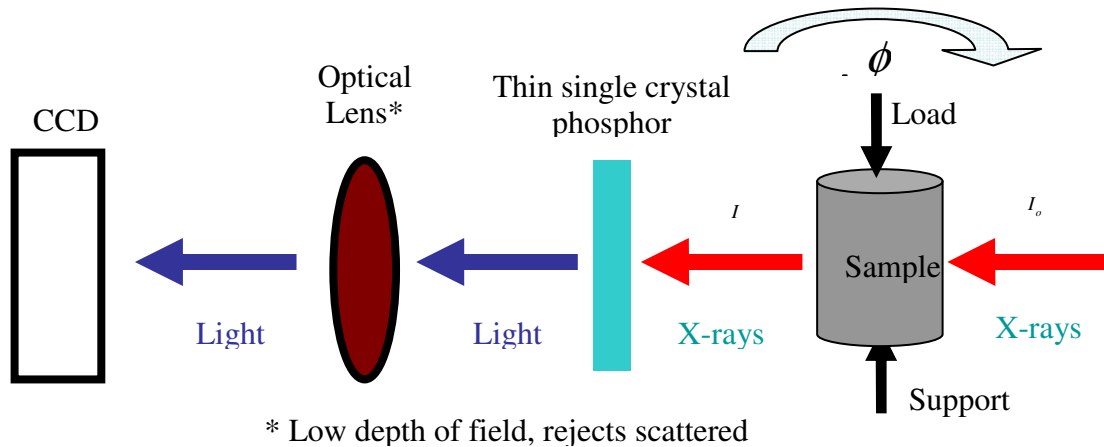


Figure 4.1: Schematic of μ-CT setup with *in-situ* compression

In the *in-situ* μ-CT measurements carried out at the Advanced Photon Source (APS), the beamline XOR-2-BM-B was used for simultaneous radiography and microtomography imaging under stress (De Carlo *et al.* 2006). Tomographs of the foam were taken at a resolution of 2.6 µm/voxel. Fig. 4.1 shows a schematic diagram of the *in-situ* μ-CT setup used for compression testing. During each scanning step, X-rays are projected on the foam sample with an initial intensity $I_0$. As the foam absorbed part of this energy, the original intensity of the X-ray was thus attenuated to *I*. The X-rays then passed through a scintillator (thin single crystal phosphor), which converts the X-rays to visible light. The optical lens focuses the visible light on a CCD camera. CCD exposures were taken at quarter degree increments from 0° to 180° and appear as radiographs [Fig.

4.2 (a)]. These radiographs were reconstructed to tomographs (De Carlo *et al.*, 2006) [Fig. 4.2 (b)], representing the volume density distribution of the foam.

A customized loading frame was used which allowed for simultaneous real-time compression and 360° observations using X-rays. The entire load frame was placed on a precision rotation and translation stage which was integrated with the μ-CT setup. A load cell (capacity 315 N) attached to the frame gave the applied force (bulk response of the foam), and the engineering stress was calculated based on the undeformed (original) sample cross-sectional area. Nominal strain was calculated from the cross-head displacements recorded by *in-situ* radiography. The foam sample was compressed up to 75% strain in seven pre-selected steps. At each step μ-CT scans were carried out to observe the deformed structure. As a first step, to determine the strains (or top platen displacements) for μ-CT scanning, a preliminary test was executed giving the stress-strain curve, without stopping for μ-CT scans. Seven strains were then chosen (based on the platen displacements). Each strain level was selected to represent a characteristic feature in one of the three regions in the foam stress-strain curve. The first μ-CT scanning was carried out for as received foam (0% strain). The second and third scans were in the elastic region, with the third scan specifically chosen before the yield stress, nearly at the end of the linear elastic region. This approximation was estimated based on the previous trials on compression of the same foam material and were carried out separately. The fourth scan was carried out just after a drop in stress was observed; it was also the beginning of the plateau region of the stress-strain curve. The fifth and the sixth scans were taken at the end of the collapse region and within the densification region, respectively. Finally the seventh scan was made when nearly all the cells had collapsed.

Figure 4.2 (a): Typical radiography image showing the entire foam material
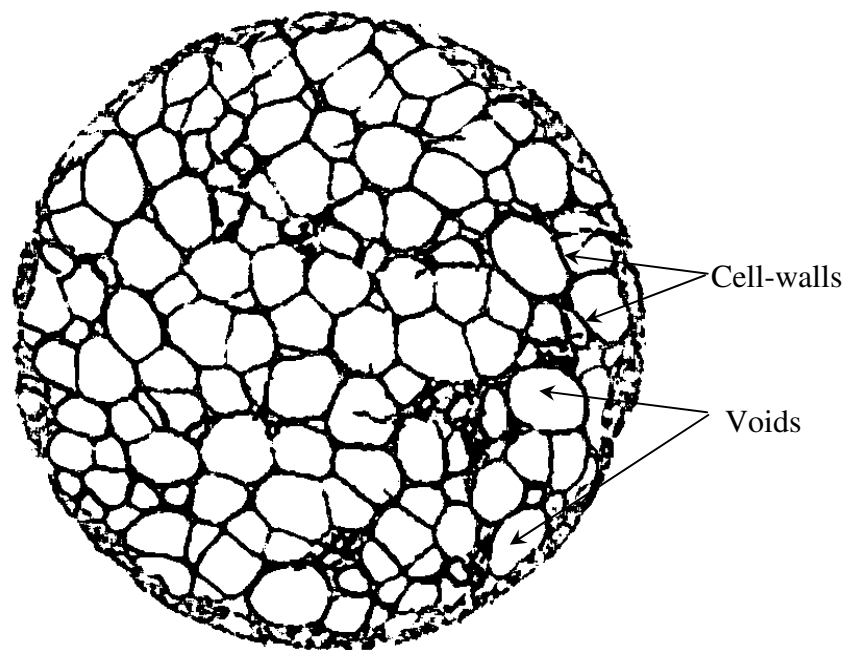


Figure 4.2 (b): Typical micro-computed tomography (µ-CT) image showing a section of the foam material

Assembly of 3D μ-CT images at selected strain levels was then used to provide the 3D deformation history of the entire sample under compression and microstructural analysis, and to compare with the MPM simulation results.

4.3.2   Modeling of closed-cell PMI foam in compression using material point method

Two-dimensional sections in the form of digital images were obtained from the 3D μ-CT information, and material points were assigned to the locations of the pixels forming cell-walls. In this way, complex microstructures can be easily converted to discretized MPM models. Further, MPM models naturally the no-slip contact between MPM particles, which eliminates the requirement for a special contact algorithm and is a reasonable approximation for such polymer based foams (Brydon *et al*, 2005). These features make MPM a reasonable choice for modeling and simulation of foams.

From the regenerated 3D solid image (procedure described in Section 4.3.1), a cubic foam sample with side length of 4 mm was selected for analysis [Fig. 4.3 (c)]. While the actual specimen is a circular cylinder, in simulation it was modeled as a cube for the convenience of applying displacement boundary conditions. This 3D solid cube of foam was created with 900 2D square digital images with a size of $900 \times 900$ pixels. Since each pixel will be assigned with a material point in MPM, in order to include more cells in simulation to reach representative results with the available parallel computer cluster (limited to 16), the resolution of the original images was reduced by 3-times to a size of $300 \times 300$ pixels [Fig. 4.3 (a)] ($3 \times 3 \times 3$ voxels in μ-CT to 1 voxel in MPM). With this resolution, on average, cell-walls along their thicknesses were represented using four material points.
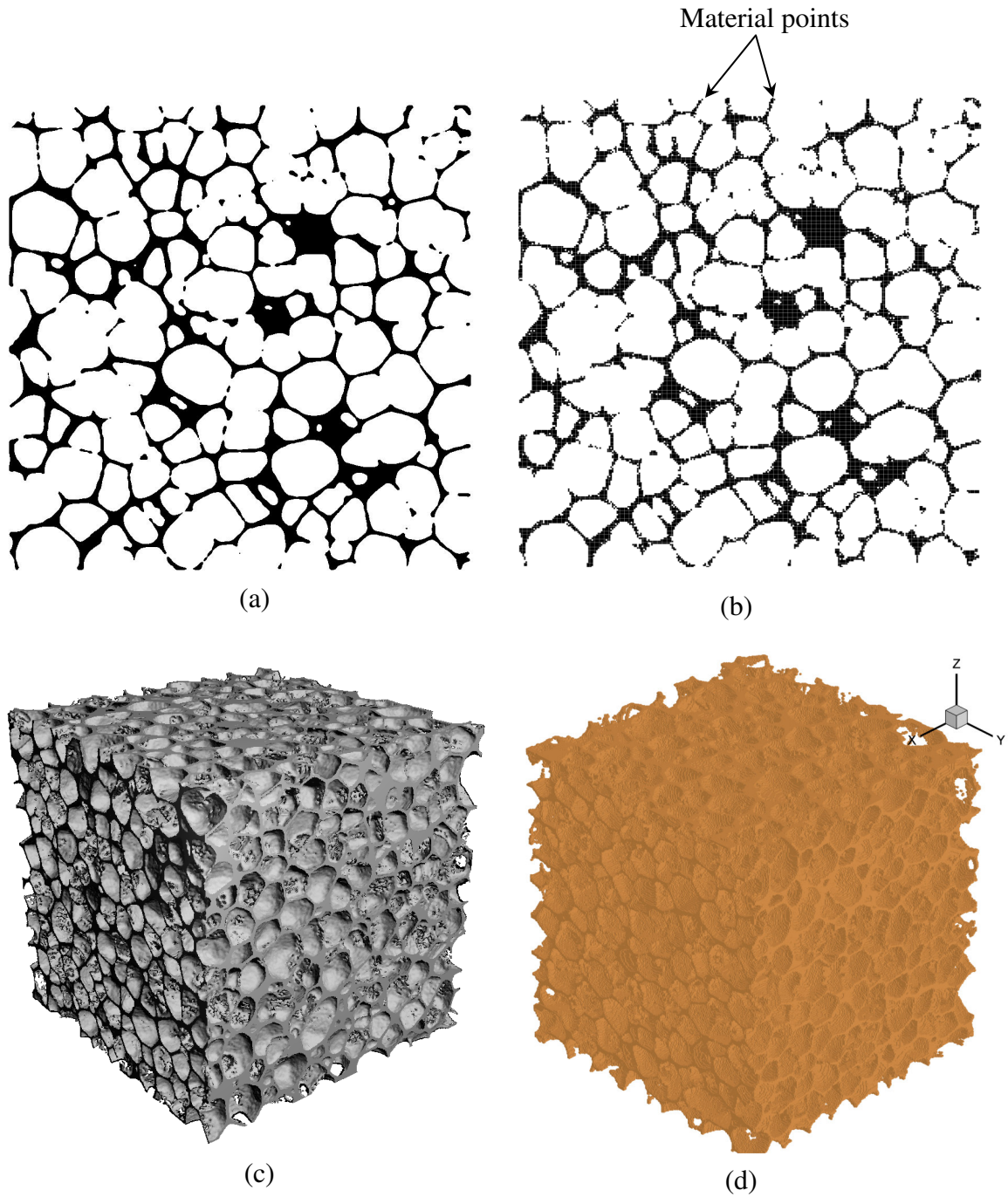
Figure 4.3: (a) Digitized image of a foam section from µ-CT (b) Discretized MPM model showing a section of material points obtained from voxels (c) 3D reconstruction of foam microstructure from µ-CT information (d) 3D discretized MPM model obtained from µ-CT information

Each pixel in these images corresponds to 14.7 µm/pixel in dimension along both *X* and *Y* axes. Within the cell-walls, the material was found to be nearly uniform. This was obtained through evaluation of the grayscale of the tomographs representing the densities of the material; the parent material was thus assumed homogeneous and isotropic. The pixels from the 2D images were then converted to material points by applying a threshold to the gray scale values of the pixels. The intensity of the pixel (black or white in Fig. 4.3) represents presence of parent material (cell-walls) or absence of material (voids), respectively. From these images, each black pixel was converted to a material point [Fig. 4.3 (b)] for MPM analysis and was assigned material properties. Such numerous 2D MPM sections were combined to form a 3D discretized foam model [Fig. 4.3 (d)] for analysis using MPM. The density and Poisson's ratio of the parent plastic material were taken as 1.2 g/cm$^3$ and 0.35, respectively, which are typical for an amorphous polymer at temperatures below the glass transition temperature (Lu *et al.* 1997).

We assigned the value of Young's modulus based on the nanoindentation measurements. The nanoindentation technique, suitable for measurements of mechanical properties of small volumes of materials, is an effective tool to measure parent material properties of such foams. Nanoindentation has been used to measure elastic (Oliver and Pharr, 1992) and plastic properties (Knapp *et al.*, 1998). Methods have been developed to measure viscoelastic properties.

Lu *et al.* (2003) and Huang and Lu (2006) developed methods for measuring creep compliance, Young's relaxation modulus, complex modulus in the frequency domain (Huang *et al.*, 2004), as well as both bulk and shear relaxation functions in the time-domain (Huang and Lu, 2007). The requirement here for sample preparation was to find a

suitable flat parent material site supported by a filler material around it to make nanoindentations. For this, small pieces of foam sample material (small enough to create an open structure with no closed pores) were embedded into epoxy. The foam with pores filled with epoxy was held at room temperature for a considerable amount of time (1 week) to allow the epoxy to harden. A Berkovich indenter with tip radius less than 50 nm was used to indent into the material. Nanoindentations were made at numerous sites over the polished cross section of parent material of the foam cell-walls. Indentations were made under a constant loading rate (47.5 µN/s), up to a maximum load of 2 mN.

Fig. 4.4 (a) shows the nanoindentation load-displacement curves with maximum depth less than 500 nm. These maximum displacements were acceptable since the nanoindents (less than 3 µm in size) were made on considerably larger sites (wall thickness > 50 µm), thus satisfying the semi-infinite workpiece approximation for analysis. The curves obtained were reasonably consistent. Based on the unloading stiffness[1] as used by Oliver and Pharr (1992) the Young's modulus of the material was 10 ± 1.3 GPa. However, since the parent material is a polymeric (time-dependent) material, this modulus obtained is incorrect and one needs to find the creep compliance through viscoelastic analysis, following the method developed by Lu *et al.*, (2003), and invert it to obtain the Young's relaxation modulus. Using this approach, the Young's relaxation modulus relation for PMI as parent material in the foam was obtained and is plotted in Fig. 4.4 (b). The steady-state value was 3.7 ± 0.2 GPa. In our simulation, the governing equations are solved in an explicit way. Simulation of such complex microstructures usually needs huge computational power. Use of a viscoelastic constitutive model would have required additional computational time per step. To reduce computational time in

---

[1]MTS Nano Indenter XP system with TestWorks (version number 4.08) software.

this work, the material model of the parent material is approximated as linear elastic-plastic (time-independent), with a constant value of 3.7 GPa for Young's modulus. The intensity of each voxel in a µ-CT is related to the density of the material at that point and is assigned a grayscale value. The material particles in MPM can be assigned proportional values of Young's modulus (or density), but for these Rohacell foam µ-CT scans, the intensities obtained were almost uniform, indicating a uniform density of the parent material throughout the foam. Hence, a constant value of Young's modulus and density, for all material points, were assigned to the foam model.

In the simulation of foam compression using MPM, a cube with side length of 2.1 mm was used. The bottom side of the foam was fixed using displacement boundary conditions. Additionally, the foam material points were confined on all four sides of the cube faces; they can slide along the side surfaces but cannot move outside of the cube faces. On the top face, four layers of material points (with material properties, $E$ and $\rho$, for these layers 1000 times higher than foam parent material properties) were added to model as a rigid platen. A velocity boundary condition was applied to the top-most layer of the platen material points. To reduce computational time the platen velocity and the simulated strain rates used in simulations are considerably higher than those used in actual experiments. A velocity of 3 m/s was applied, and this velocity was initially ramped-up linearly from 0 to 3m/s in 5µs. The time step ($\Delta t$) used in the simulations was $\Delta t = kL / c_d$, where $L$ is the background mesh grid length, $c_d$ is the dilatational wave speed of the parent material, and $k$ is a positive constant satisfying $k \leq 1$. A smaller $k$ leads to improved accuracy in the solution, and typically $k = 0.1$ was used in our simulations.
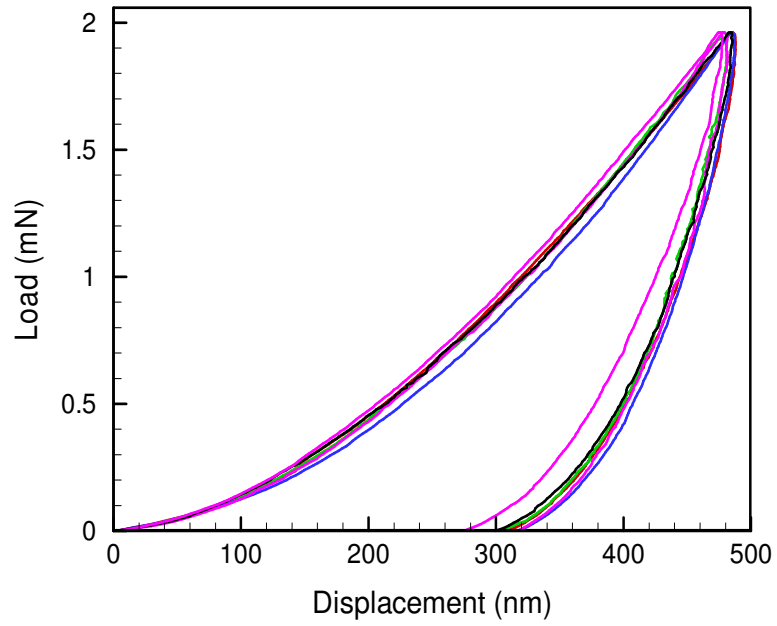
(a)
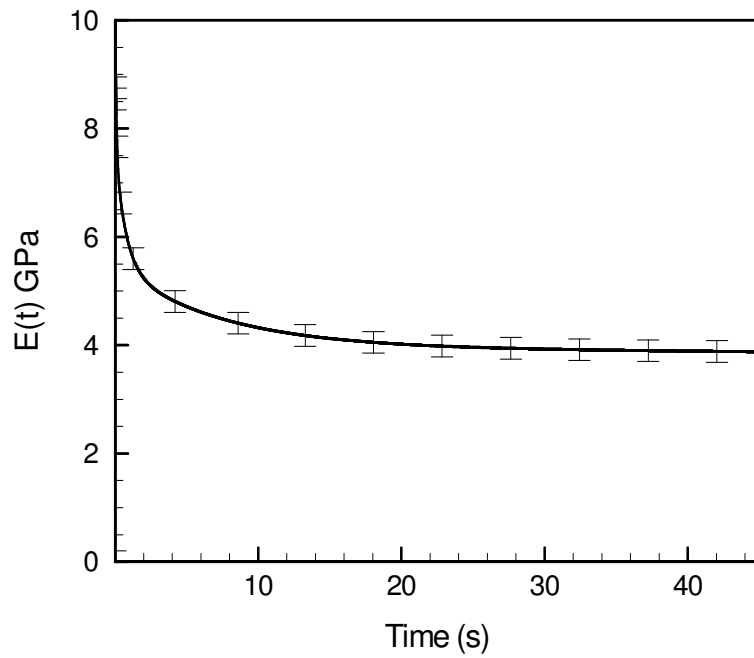


(b)

Figure 4.4:  Direct measurement of matrix mechanical properties using nanoindentation on cell-walls of the foam (a) Nanoindentation load-displacement curves (b) Young's relaxation modulus of PMI foam parent material.

With this consideration, the resulting time step was 3 ns which made the task of running the simulations at experimental quasistatic strain rates time consuming. Thus an increased velocity was used in simulations, and corresponds to ~ 0.18% of the longitudinal wave speed of the parent material. The loading may thus be considered as quasistatic (Bardenhagen *et al.*, 2005; Nairn, 2006).

In the simulation of such a dynamic problem, the force is applied at the top, while the bottom side of the sample does not initially feel the force. The compressive wave will travel to the bottom and reflect back. It normally takes three to five cycles of reflections for the stresses applied on both top and bottom to reach dynamic equilibrium. Hence, one has to check for the forces applied on both top face (moving platen) and bottom (fixed) face to determine whether the dynamic equilibrium state has been established. The net force on the bottom face was obtained by summing up the forces on the background grid nodes (at which the displacement boundary condition was applied), which were further obtained from the interpolated material point forces. The net force on the top face was calculated by summing up the force acting on the bottom-most layer of material points forming the rigid moving platen. The stresses for deducing the stress-strain curve were calculated based on the undeformed cross-sectional area of the foam. Each time, when the material points on the platen move, their average displacement was registered. This was then divided by the original length of the undeformed foam to calculate the nominal strain.

For the MPM simulations, a 16-node cluster (each with a 2.8 GHz processor) was used to simulate an RVE of the foam structure. During the compression, the faces on the five sides surrounding the foam (except the top face where the velocity boundary

condition was applied) were constrained to prevent material points from moving outside of the faces of the cube, following the approaches taken by Brydon *et al.*, (2005), and Nairn (2006). To simulate the failure of foam cell-walls, von Mises plasticity with isotropic bilinear hardening along with a stress based failure criterion was used. An attempt was made to determine the values of these parameters using inverse-problem solving methodology to allow the simulated stress-strain curve to correlate with the experimental curve.

Simulations were run until a compressive strain limit of 75 % was reached. Each simulation took at a minimum 5 days of computational time for a foam size of $2.1 \times 2.1 \times 2.1$ mm$^3$ using a background computational element size of 30 µm. The parallel environment was provided by the Structured Adaptive Mesh Refinement Application Infrastructure (SAMRAI) (Hornung and Kohn, 2002) developed at the Lawrence Livermore National Laboratory (LLNL). The geometry of the foam is discretized using cubic material points having dimensions $14.7 \times 14.7 \times 14.7$ µm$^3$. The background mesh consists of three-dimensional solid, 8-node, cubic elements covering the entire region, with element-length of 30 µm which is approximately twice the particle size used for discretization. With this, the number of particles per background grid element is approximately eight, which is an appropriate number for such problems (Nairn, 2006). Considering the limitations in the available computational capacity, in order to determine the behavior of the larger foam structure from a smaller model, simulations need to be carried out on a representative volume element (RVE). An RVE study is conducted to find an appropriate size, based on the convergence of the initial portion of the foam strain-strain response.

4.4   Results

4.4.1   Experiments on compression and *in-situ* µ-CT imaging of closed-cell PMI foam

Fig. 4.3 (c) shows the 3D rendering obtained from X-ray µ-CT imaging using a Scanco µCT-40. A threshold value of 25 was used for 3D model regeneration. The 3D rendering software[2] had integrated post-analysis capabilities, which gave values of porosity, and average values of cell-wall thickness and cell-size. The porosity of the foam was found to be ~ 70 %. The average values of cell-size and cell-wall thickness were 0.3 mm and 0.05 mm, respectively. Synchrotron X-rays were used for the *in-situ* µ-CT scans while the foam was under compression. An initial scan was taken for the undeformed (0 % strain) foam with a scanning resolution of 2.6 µm/voxel. As the compressive experiment progressed, six more scans were made by stopping the moving piston (platen). It took 3 hours to complete X-ray scanning of an entire sample at a given strain. Simultaneous radiograph images, which could be acquired relatively quickly, gave the information of global strain in the sample corresponding to the moving platen position.

Fig. 4.5 (a) shows a typical stress-strain curve obtained from the compression tests on a cube of foam. Similar curves were observed on the cylindrical samples used in the synchrotron µ-CT with *in-situ* compression, which also provided radiography capabilities. The stress-strain curve of a typical foam as pointed out earlier, is characterized by three regions, initial linear elastic (up to 5.5 % compressive strain), a plateau region (between 5.5 % and 53 %), and densification region (greater than 53 %). The Young's modulus of this foam, as measured from the slope of the linear elastic region, was 247 MPa.

---

[2] From Scanco, www.scanco.ch
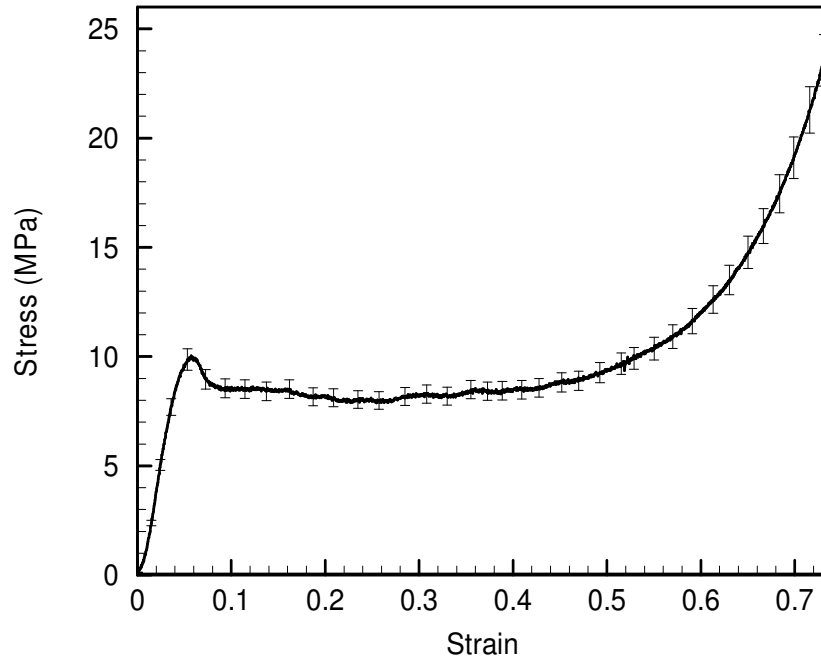
Figure 4.5 (a): Experimental stress-strain curve from Rohacell foam in compression
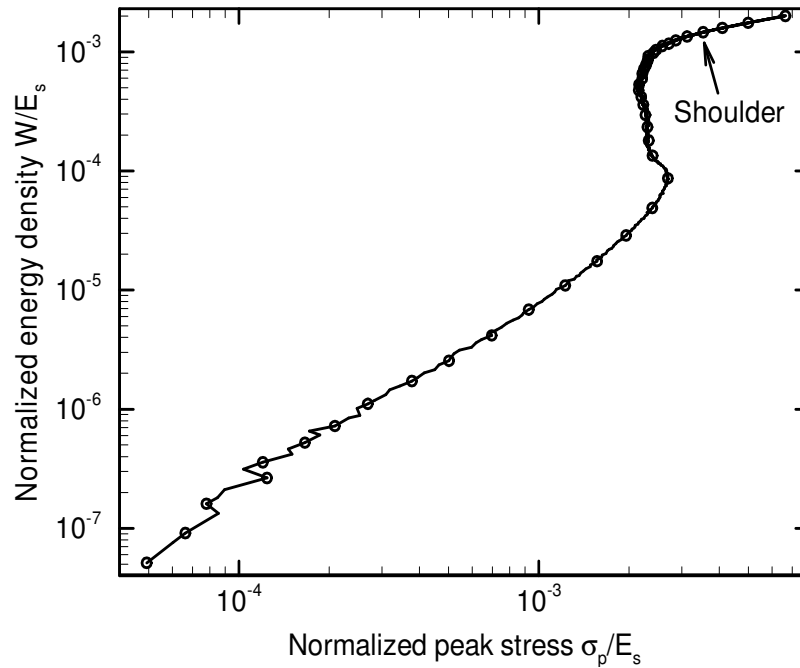


Figure 4.5 (b): Energy absorption diagram for Rohacell foam, The skeletal
Young's modulus $E_s$ = 3.7 GPa.

It is seen that this foam has a considerably higher modulus as well as higher yield stress (10 MPa), compared to other similar polymer foams. The specific energy absorption obtained was 35.2 J/g. Fig. 4.5 (b) shows the normalized energy absorption ($W/E_s$) as a function of normalized peak stress ($\sigma_p/E_s$). Here, $E_s = 3.7$ GPa, is the skeletal Young's modulus, $W$ is the energy density calculated as area below the stress-strain curve up to a strain corresponding to the peak stress, $\sigma_p$. The lower strain limit of the densification region is termed as the densification strain ($\varepsilon_D = 0.62$) and is indicated as shoulder. The specific energy absorption up to $\varepsilon_D$ is 25.5 J/g.

Fig. 4.6 shows the central 2D sections of the 3D X-ray μ-CT corresponding to compression of foam carried out in seven steps, each corresponding to an increased strain. Many cell-walls, on both the top and bottom bend and buckle during deformation. Localized buckling of cell-walls was observed even in the initial elastic regime of foam compression. This microstructure deformation pattern can be seen clearly in Figs. 4.6 (a) – (c), which shows 2D sections of the deformed foam for strains less than 5.5 %. At a point midway through this elastic region, at 2% compressive strain the deformed microstructure is shown in Fig. 4.6 (b). This image shows localized bending and buckling of cell-walls, as compared to the initial undeformed image [Fig. 4.6 (a)]. Some buckled sites are circled in the figure. Further, Fig. 4.6 (c) shows deformation at slightly higher strain ($\varepsilon = 4$ %), which corresponds to the end of the linear elastic region, and prior to the yield point. At this stage, it is seen that a number of cell-walls have buckled, and these are mostly the ones which are parallel or which form small angles with the loading axis (vertical in Fig. 4.6). Further, comparing Fig. 4.6 (c) with Figs. 4.6 (a) and (b), it can be seen that the shape of the cells has changed.
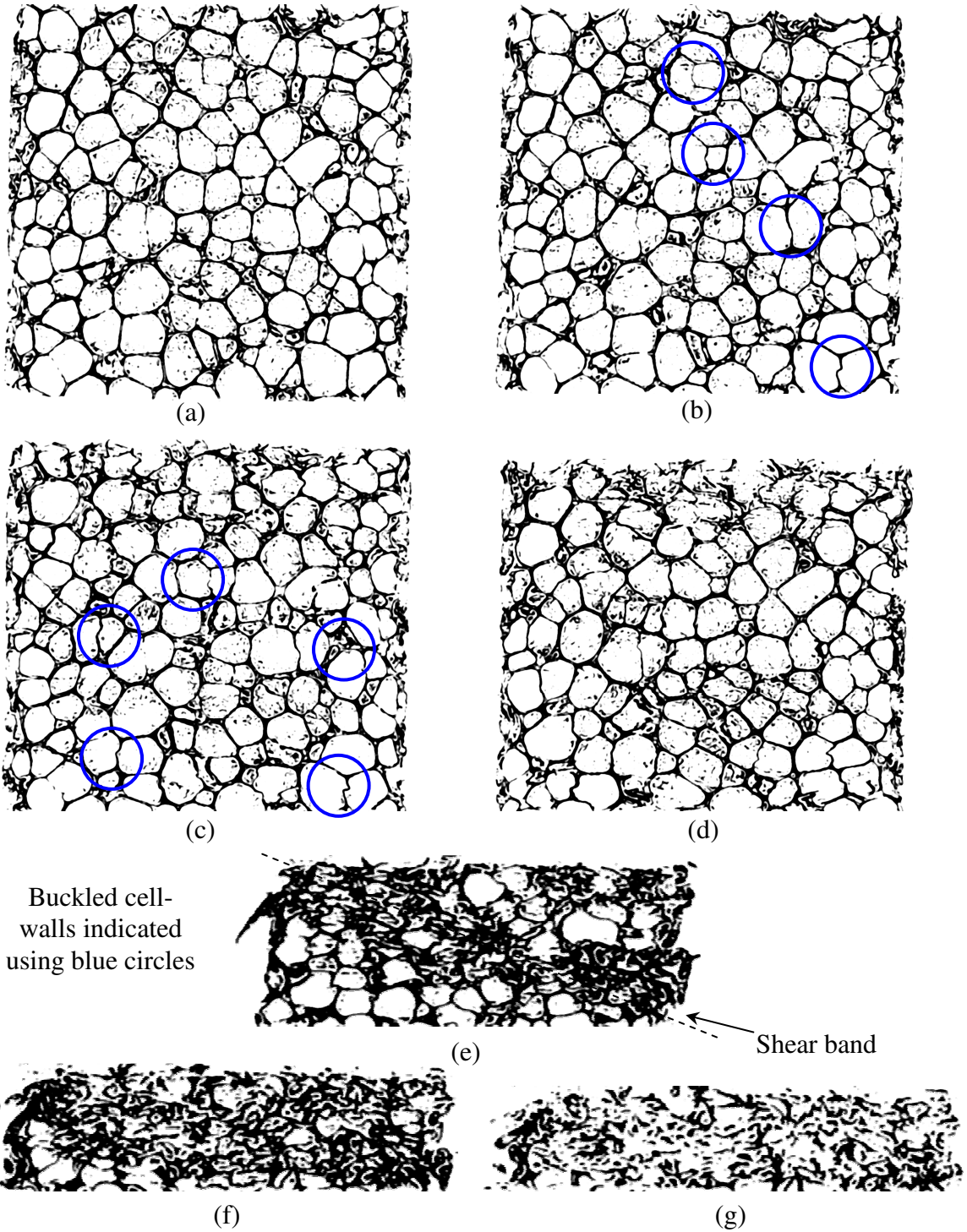
Figure 4.6: Snapshots showing sections along the loading axis from *in-situ* μ-CT of foam at different compressive strains (a) Undeformed (b) Initial linear elastic region, with some localized buckling of cell-walls, at 2% strain (c) Cells change shape at 4% strain, before first collapse (d) Immediately after first collapse in the stress-strain curve at 9% strain with relatively many buckled cell-walls (e) Visible shear band at strain of 57%, approximately corresponding to the end of plateau region (f) Flattening with residual cells (strain of 68%) (g) Densified foam structure at compressive strain of 74%

After a strain of 5.5 %, a yield point is observed and it is reflected as a dip in the measured stress in the stress-strain curve. During this yielding, the stress decreases from 10 MPa at 5.5 % strain to 8.5 MPa at 9 % strain. This stress-dip with increase in strain is similar to the behavior of brittle metal foams (Gibson and Ashby, 1997). Fig. 4.6 (d) shows the μ-CT image immediately after this dip in the stress is observed, corresponding to the compressive strain of 9 %. From the μ-CT image, it is seen that the number of buckled sites has increased. At this point, the buckled sites were observed not only on vertical walls, but even on the some inclined walls which formed an angle as much as 45° with the loading axis. Further, in this case, a sufficient number of localized buckling (weak) sites existed prior to a strain of 5.5 %, which may have linked together to form a weak zone.

Compression beyond the yield stress initiated a collapse along this weak zone. During this process, it was observed that, the cell-walls which formed smaller angles with the loading direction showed a tendency to bend, buckle, or even fail; and twist, while the cell-walls forming higher angles (close to being perpendicular) with the loading direction showed a tendency to stretch and twist or even bend. As a result of stretching, bending, or twisting of these cell-walls in the weak zone, neighboring cells (which may have been subjected to higher compressive stress) were affected, and as a result, the neighboring cells may have started to collapse. The neighboring cells besides the shear strain-localization zone continued to collapse, and a collapse wave, was observed travelling on both sides of the initial weak zone. Fig. 4.6 (e) shows one such instant showing the shear band formed due to collapsed cells after a considerable compressive strain of 55 %. In this figure, some of the residual cells can be seen on the top-right and bottom-left region

across the shear band. Further compression made almost all the cells in the foam collapse. Consequently, the foam approached densification as seen in Fig. 4.6 (f), and corresponds to a compressive strain of 68 %. Further compression flattens almost all the cells at 74 % strain. Further compression of this structure was seen associated mostly with neighboring cell-walls pushing against each other, somewhat similar to compressing the parent material itself.

A few points that should be noted are mentioned here. In Fig. 4.6, observations were made on a fixed spatial plane. From Fig. 4.6 (d) onwards, as the deformation increases some material comes in and goes out of the selected central section. Therefore, some of the cells from Figs. 4.6 (a) – (c) may not correspond or show up in Figs. 4.6 (d) – (g). Additionally, since the foam compressed under *in-situ* X-ray imaging was not laterally constrained, the overall deformation of the sample turned out to be somewhat similar to shear failure without material separation. In this case a tilted band of cell collapsed first, and due to this the top-half of the residual (non-collapsed cells) foam shifted with respect to the bottom portion of the foam in the transverse direction. As the compressed foam widens, in order to maintain the field of view, the optical magnification was halved to 1.25x and this in-turn doubled the pixel to length scaling factor within the latter three tomographs [Figs. 4.6 (e) – (g)].


4.4.2   Simulation of compression in foam using MPM

4.4.2.1   Representative volume element (RVE) study

Compression simulations were carried out on closed-cell foam structure discretized using cubic material particles. We have considered approximately eight material points

76

per cell belonging to the background grid and has been a suitable number for 3D MPM simulations (Nairn, 2006). Sizes of foam microstructure that can be simulated were limited by the available computational capacity. In order to reproduce the behavior (stress-strain curve) of the entire foam model, in this study, simulations were carried out on an RVE of the foam microstructure. Thereby, results such as the stress-strain curve and microstructural evolution during deformation for sizes greater than the RVE can be predicted by repeating the RVE over the desired volume.

To find the representative volume from the available 3D μ-CT information [Fig. 4.3 (d)], increasing the volume of the foam cube was considered. The smaller of these was given a side length of 2x. Here 'x' represents the average foam cell diameter determined form μ-CT (0.3 mm). For purpose of convergence, the linear elastic region of the stress-strain curve (up to a strain of 5%) was selected for comparison. Stress-strain curves were obtained for five different sizes of foam, namely 2x, 3x, 4x, 5x, and 7x, and are plotted in Fig. 4.7. In all cases, the platen velocity was kept the same. It was seen that, as the model size increased from 2x to 4x, different values of stresses are obtained for a given value on the strain axis. However, the difference in stress decreases as the sample size increases to 7x. For the stress-strain curve obtained at the 7x side length, it took relatively more time to establish dynamic equilibrium within the sample, and hence initially some higher stress oscillations are seen in the stress-strain curve. The results obtained from foam sizes 5x and 7x are comparable. Thus the size of foam with minimum side-length of 7x (2.1 mm) gives a true RVE.
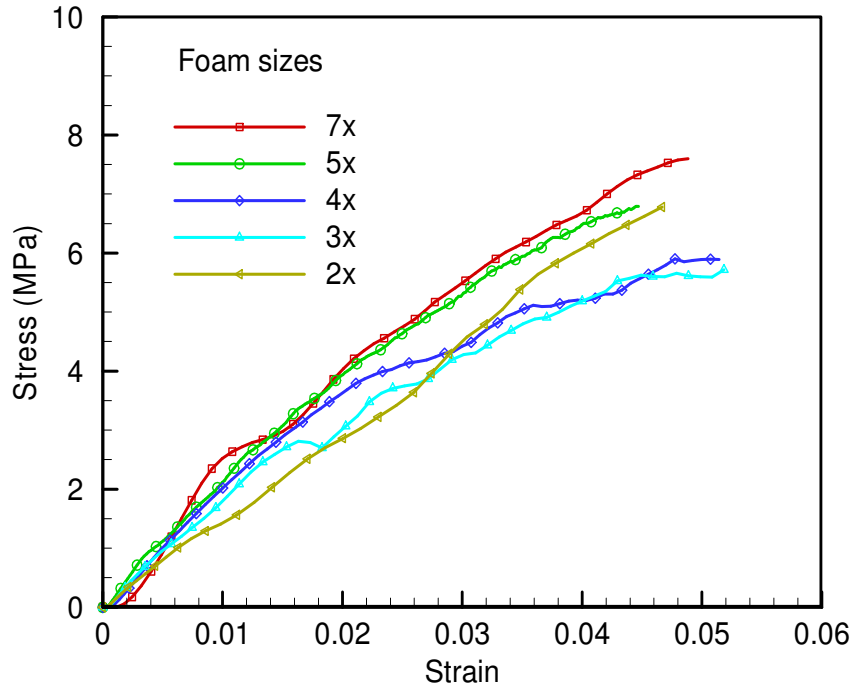
Figure 4.7: Comparison of stress-strain curves obtained using MPM simulation from different sizes of volume elements of the foam

### 4.4.2.2  Results from compression of the foam's RVE

The foam used for compression simulations was a cube with 2.1 mm side length. A moving top platen was used to compress the foam against the fixed bottom platen. Velocity applied to the top platen was 3 m/s. The global stress, calculated from loads experienced on both the top (moving) and bottom (fixed displacement) platens were archived. In experiments, the parent material in the foam showed elastic-plastic as well as viscoelastic material response, along with some material failure. In MPM simulations, a von Mises elastic-plastic constitutive material model with isotropic hardening was used for the parent (cell-wall) material. Failure criterion based on von Mises stress exceeding a pre-defined critical failure stress value was used to model the material failure. It should be noted that, in obtaining the numerical stress-strain curve an inverse methodology was

used to match the experimental results by varying the failure stress, yield stress, and the hardening coefficient for the parent material. Initially, the parent material was assigned a linear purely-elastic constitutive model with no material failure. Fig. 4.8 shows the stress-strain response obtained from the foam with an elastic material model for the parent material.
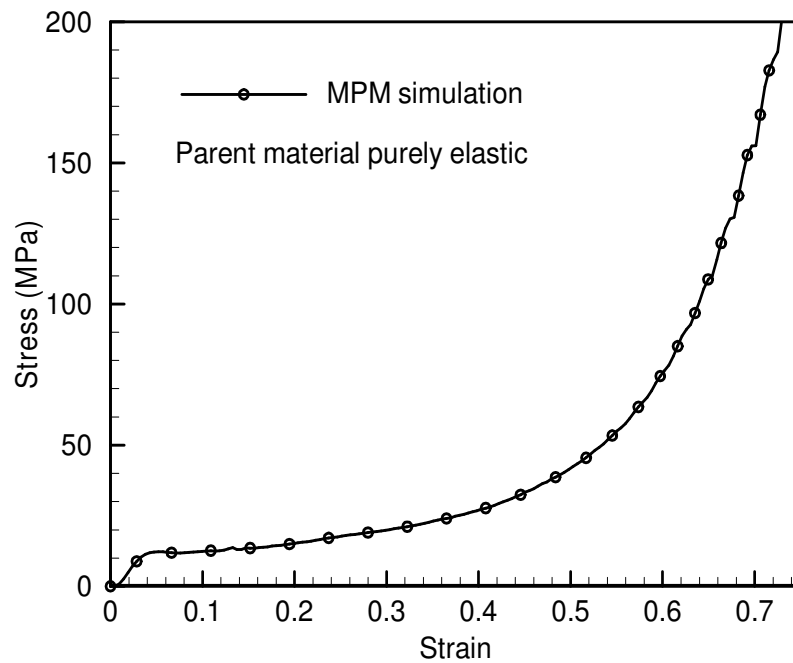


Figure 4.8: Stress-strain curve obtained from numerical simulation using purely elastic properties for the parent material. The three stages of deformation are captured in this simulation

It is seen that the typical features of a foam response were very well reproduced, with an initial elastic region, then yielding, followed by a stress plateau with slight hardening, and finally the densification region. The initial linear elastic region of the stress-strain curve from simulation compares well with the experimental data. The yielding occurs at a stress of 10 MPa, which is very close to the experimental value. However, in the stress plateau

and densification regions the stress response is considerably higher than experimental results.

In order to allow the stress-strain curve to correlate with experimental results, the parent material was then assigned an elastic-plastic material model that allowed material failure. Fig. 4.9 (a) shows the nominal stress plotted as a function of strain; the strain is calculated from the displacement of the platen divided by the undeformed length of the foam. As the foam was compressed, there was initially a nearly linear elastic increase in the stress corresponding to the increase in the strain. After a few cycles of wave reflections, within a short period, dynamic equilibrium was established. It is seen that the stress-strain curve starts to yield at a compressive strain of 5.5 % and after which it flattens. The elastic modulus recovered from the slope of the initial linear elastic region was 303 MPa.

Fig. 4.9 (b) shows the comparison of stress-strain curves from the numerical simulation with the experimental result. The material properties used for this particular simulation were 120 MPa for yield stress, 290 MPa for hardening modulus, and 300 MPa for the failure stress. However, with the limited computational capacity, each of such simulations took a minimum of 5 days. As a result, the inverse methodology approach to find the elastic-plastic material model properties of the parent material, by fitting the simulated curve through refining three parameters against the experimental curve remains ongoing. Fig. 4.10 shows 3D views of the simulation of foam undergoing compression. The material points are colored according to their value of stress ($\sigma_{zz}$) in MPa. Fig. 4.10 (a) is the initial undeformed foam structure. The foam undergoes elastic deformation and compaction during compression.
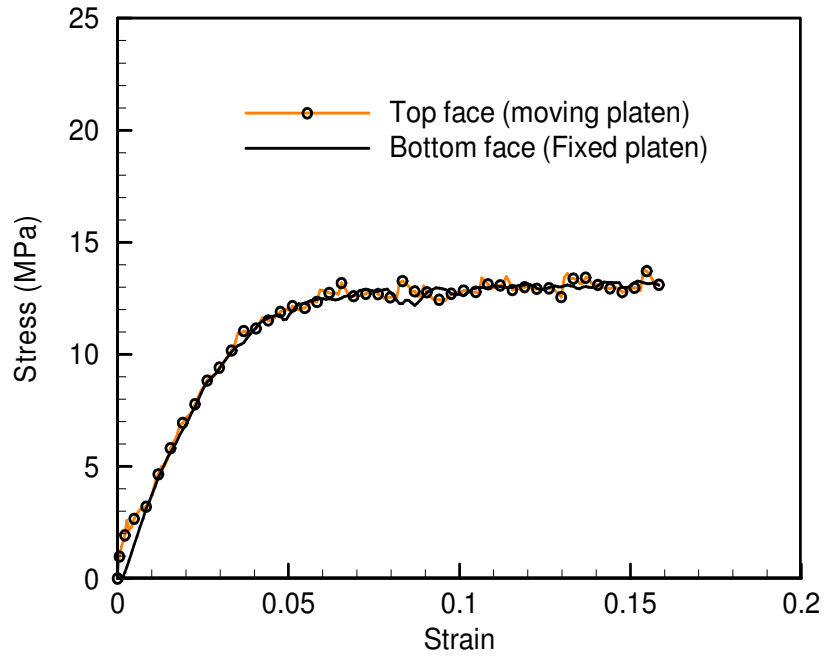
Figure 4.9 (a): Comparison of stress-strains curves from MPM simulation
indicating dynamic equilibrium
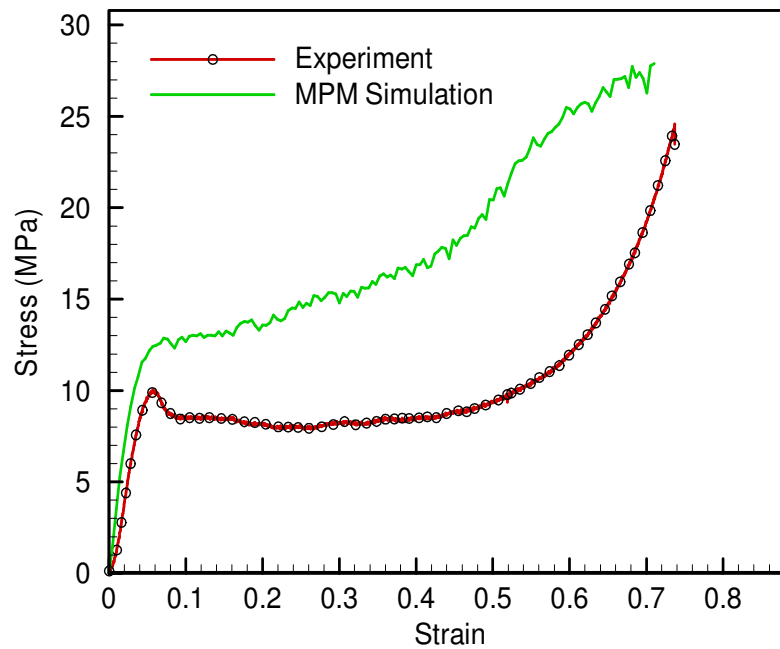


Figure 4.9 (b): Comparison of stress-strain curve obtained from numerical
simulation using MPM with experimental data

Fig. 4.10 (b) shows the deformed microstructure (with collapsed cells), nearly at the end of the stress plateau, corresponding to 57 % compressive strain. Finally, Fig. 4.10 (c) shows the fully densified foam structure at 75 % compressive strain.

Figs. 4.11 and 4.12 show 2D sectional snapshots of microstructural deformation during compression. The location of sections shown in Fig. 4.11 correspond to a depth of 67.5% of the thickness of the foam in simulation. The sections in Fig. 4.12 correspond to a depth of 42.5% within the model along the *X*-axis [indicated in Fig. 4.3 (d)]. In both the figures, the thickness of the section is 0.1 mm (5% of the total depth along *X*-axis, measured from the *Y-Z* plane) and Figs. (a) to (g) (of Figs. 4.11 and 4.12) correspond to compressive strains of 0, 2, 8, 12, 57, 68, and 75%, respectively. As the top platen starts compressing the initial undeformed foam microstructure [Figs. 4.11 (a) and 12 (a)], an initial loading (stress) wave travels through the foam wall material and reflects within the cells and from the fixed boundaries, back and forth. After some simulation-time, the stress waves are superimposed and dynamic equilibrium was established. After which the foam experienced almost uniform loading at a constant strain rate.

During compression, most of the cell-walls forming smaller angles with the loading axis act as a load path and carry the majority of the stress. Some of these cell-walls, inclined at a relatively higher angle with the loading axis, start bending and show tendencies of buckling even at low overall strains levels. At 2% global compressive strain corresponding to the initial elastic portion of the stress-strain curve Fig. 4.11 (b) shows some of the cell-walls undergoing bending and Fig. 4.12 (b) shows locally buckled cell-walls.
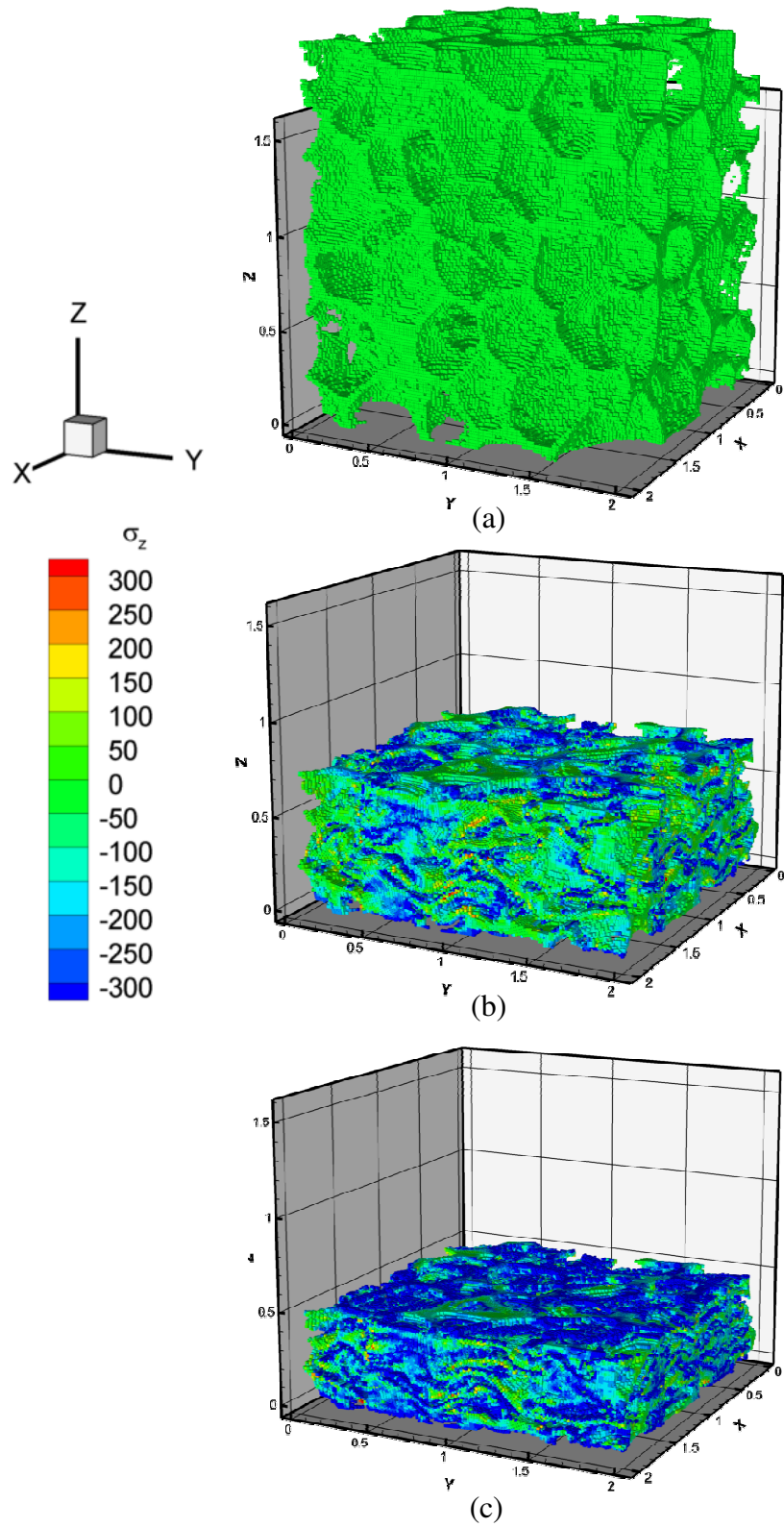
Figure 4.10: Snapshots showing 3D views of foam RVE in compression from MPM simulation, and contours indicate stress $\sigma_{zz}$ (MPa) (a) Undeformed (b) At 57% compressive strain (c) At 75% compressive strain
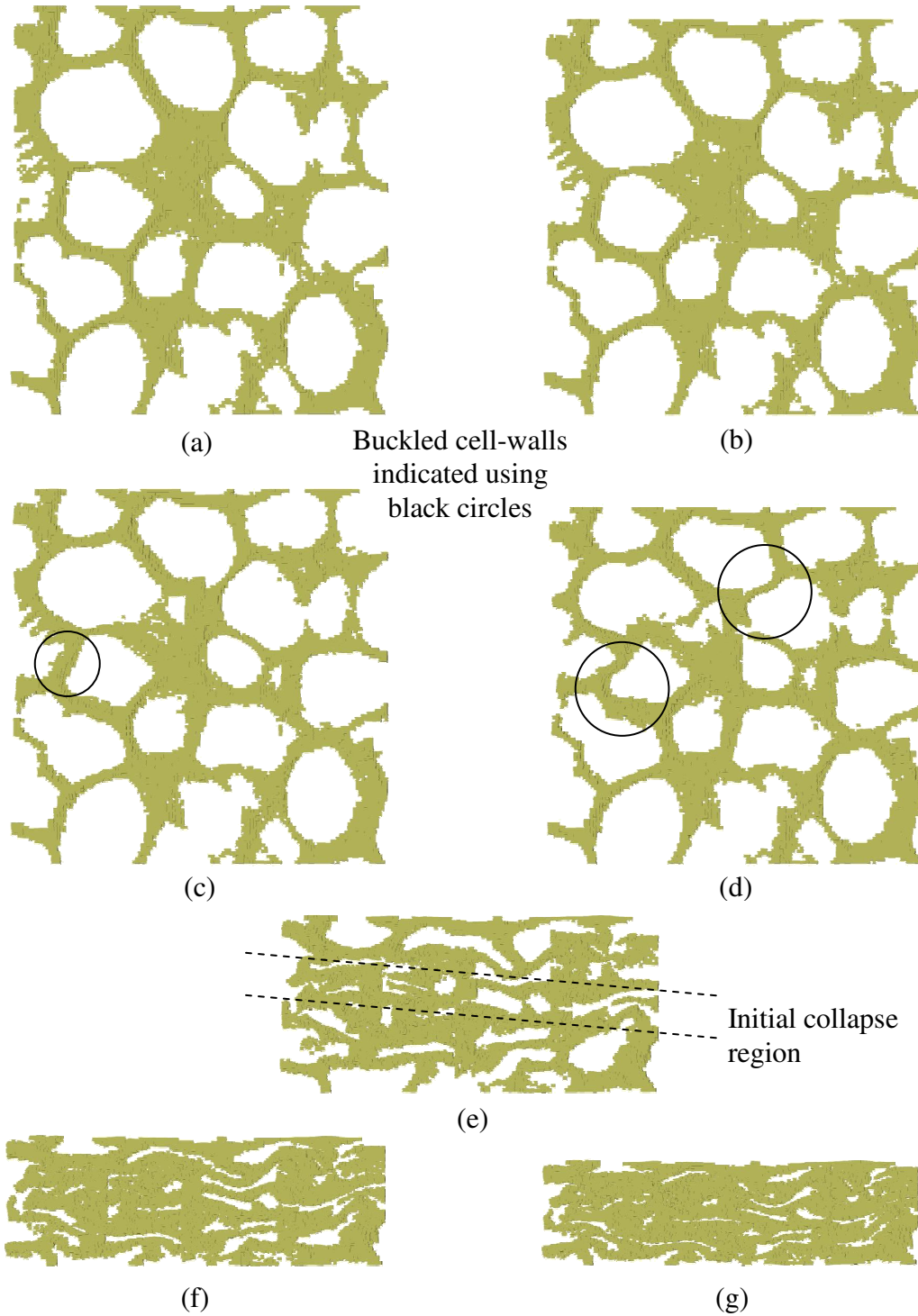
Figure 4.11: Snapshots showing sections (thickness 5% of the model length and located at a depth of 67.5% within the model along the *X*-axis) along the loading axis from MPM simulation of foam RVE in compression (a) Undeformed (b) Initial linear elastic region, at 2% compressive strain (c) Cells change shape at 8% compressive strain (d) After yielding, at 12% compressive strain (e) At compressive strain of 57% (f) Flattening with residual cells (compressive strain of 68%) (g) Densified foam structure at compressive strain of 75%
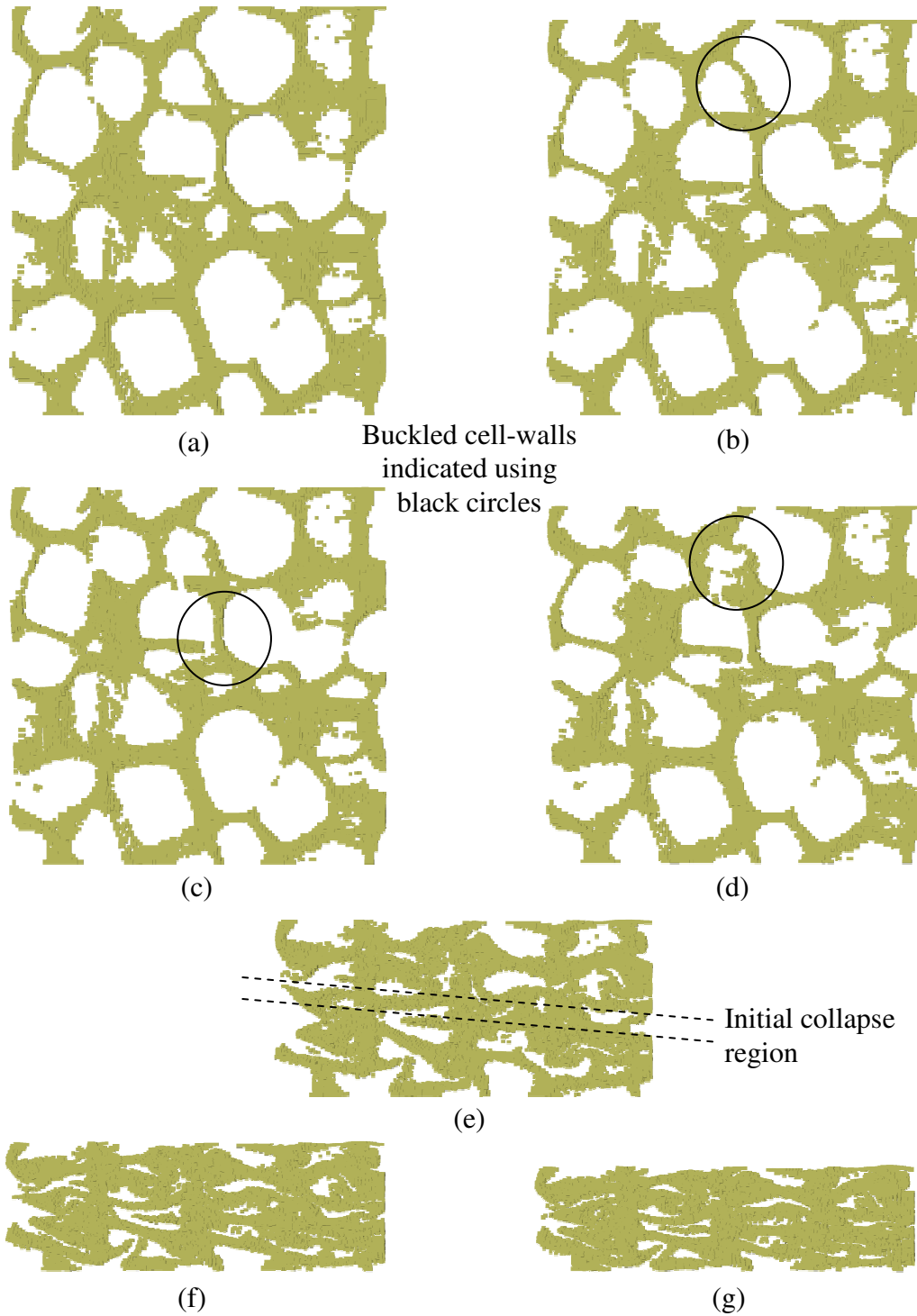
Figure 4.12: Snapshots showing sections (thickness 5% of the model length and located at a depth of 42.5% within the model along the *X*-axis) along the loading axis from MPM simulation of foam RVE in compression (a) Undeformed (b) Initial linear elastic region, at 2% compressive strain (c) Cells change shape at 8% strain (d) After yielding, at 12% compressive strain (e) At compressive strain of 57% (f) Flattening with residual cells (compressive strain of 68%) (g) Densified foam structure at compressive strain of 75%

Further increase in the compressive strain would have increased the stresses in the cell-walls which carry the majority of the stress, and thus an increasing number of localized cell-walls were seen to buckle [Figs. 4.11 (c) and 4.12 (c)]. At a certain stress value, the weakest zone formed by aggregates of locally buckled cell-walls was no longer able to support the load and it collapsed.

Figs. 4.11 (d) and 4.12 (d) show snapshots just after yielding was observed in the simulated stress-strain curve. The cell-walls corresponding to the collapsing cells were seen to bend, extend, and twist thereby weakening the surrounding intact cells. The initial collapsed cell-walls forming a weak zone (region) can be observed in Figs. 4.11 (e) and 4.12 (e), and are indicated between the dotted lines. The cells within these dotted lines are relatively highly collapsed, while in the regions above and below this weak region, many sites of residual uncollapsed cells can be seen. With further increase in the compressive strain, eventually, the entire structure collapses. The residual voids vanish [Figs. 4.11 (f) and 4.12 (f)] leading to a densified structure with extensive contact between the cell-walls [Figs. 4.11 (g) and 4.12 (g)].


4.5   Discussion

From the microstructure deformations observed in Figs. 4.11 and 4.12, it was clear that many of the cells walls that initially underwent buckling or bending were inclined forming angles as much as 45° with the loading axis. These were a part of the structure which carried the majority of the stress. Fig. 4.13 shows 2D sections of foam located at a depth of 67.5% and 42.5%, along the *X*-axis, and the color of the material points indicating the value of stress component along the loading axis, $\sigma_{zz}$. The blue color

indicates material points with relatively higher compressive stress (< -40 MPa). From both the sections, it can be seen that, the areas with higher stress are mainly the cell-walls which are either almost vertical or they make angles as much as 45° with the vertical, which together act as load paths for the foam undergoing compression. In order to determine out the amount of material which actually carried a majority of the load, calculations were made for the entire model to determine the number of material points having a compressive stress higher than the cut-off stress. This cut-off stress was selected based on the average compressive stress in the section, which was approximately -32 MPa for 8% strain and -18 MPa for 2% global strain, corresponding to deformation in the elastic region. The ratio of this number to the total number of material points was obtained. It was inferred from these calculations that, at both strains 35% of the material (with compression stresses greater than -40 MPa in case of 8% strain and -20 MPa in case of 2% global strain during foam simulation) carried nearly 75% of the load in compression. It should be noted that, in the simulation of foam in compression, the sides of the cube were constrained. Simulations were also conducted on unconstrained foam.

Fig. 4.14 shows a comparison between the two simulated cases and the experimental measurements. It shows that in the case of constrained foam, the stiffness and the yield stress are approximately twice that for unconfined case. In the constrained case, the confinement pressure (lower than axial compressive stress) will induce compressive stress in the lateral direction to resist the buckling of highly inclined cell-walls, compared with the unconstrained case. The foam cell-walls are thus able to delay the onset of buckling, and hence increase the plateau stress associated with buckling and collapse of cell-walls and stiffen the response.
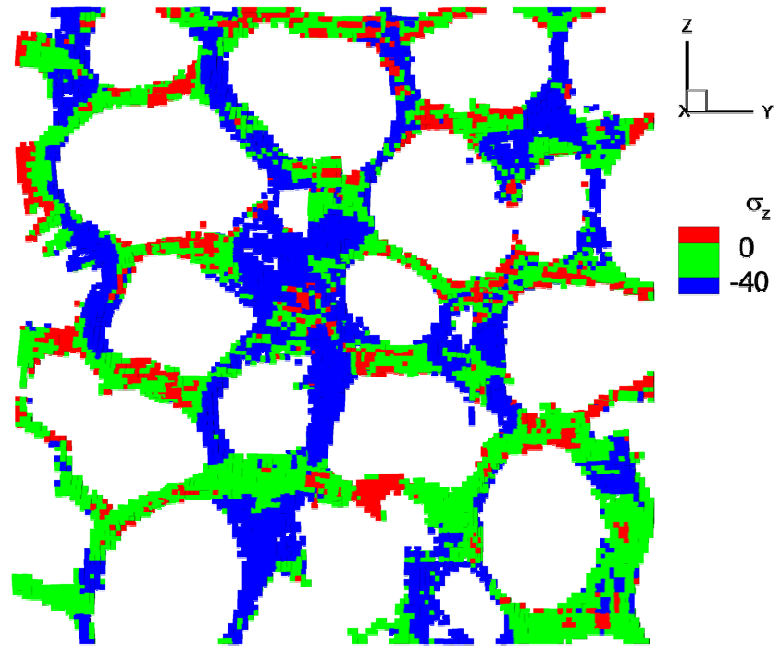
(a)
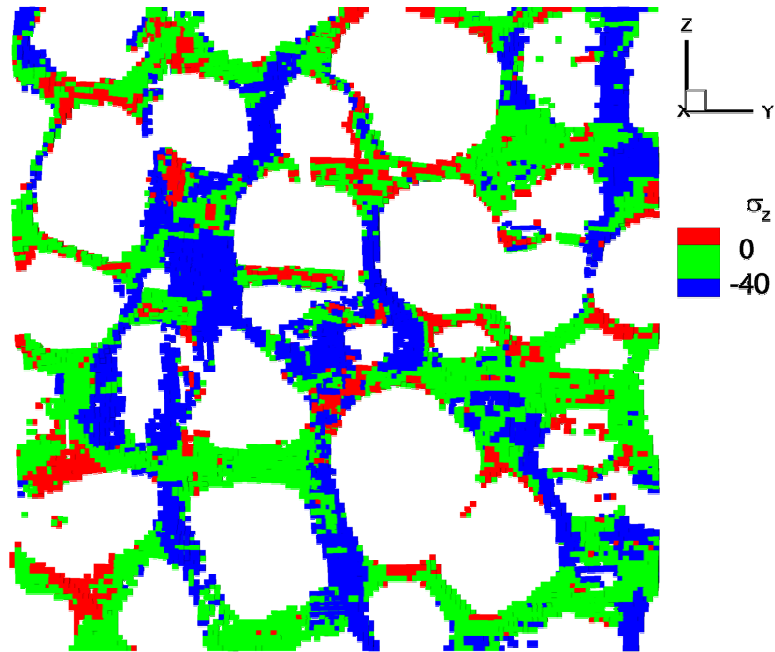


(b)

Figure 4.13: Snapshots showing stress component $\sigma_{zz}$ (MPa) on the sections (thickness 5% of the model length) aligned along the loading axis (Z), at 8% compressive strain, and located at a depth of (a) 67.5% (b) 42.5% of the entire model length, along the *X*-axis

The results indicate that the elastic-plastic constitutive model used in this study was capable of simulating the features in the stress-strain curve and the microstructure evolution. However, the stress-dip in the stress-strain curve after yielding was not captured. Future work will involve use of other phenomenological based material constitutive models for the parent material (cell-walls). Models such as viscoelastic, viscoplastic, or power-law hardening are under consideration including failure criteria, in order to obtain simulation results closer to the observed values. The value of Young's modulus obtained using the linear elastic region from simulation was found to be higher than the one obtained from experiments. This might be due to the higher strain rate used in the simulations which may have induced higher inertial effects, or even due to constrained side walls. Secondly, the same background mesh element-length as that of material particle size, would have been able to model the cell-walls with sharper boundaries at the cost of increased requirement of computational capacity. To save on the already lengthy computational time, the mesh element-length used in this study was coarse (twice of the particle size), which in-turn might have caused a stiffer material response in the collapse and densification regions.

Simulation of foam in compression is a challenging task. While MPM has demonstrated its potential to capture major features of foam compaction (Bardenhagen *et al.*, 2005, Brydon *et al.*, 2005), to date, no results have been reported to give excellent agreement between simulation and experimental results. In our current work, we have conducted compression experiments with *in-situ* micro-computed tomography to observe the microstructural evolution during compression of closed-cell Rohacell foam.
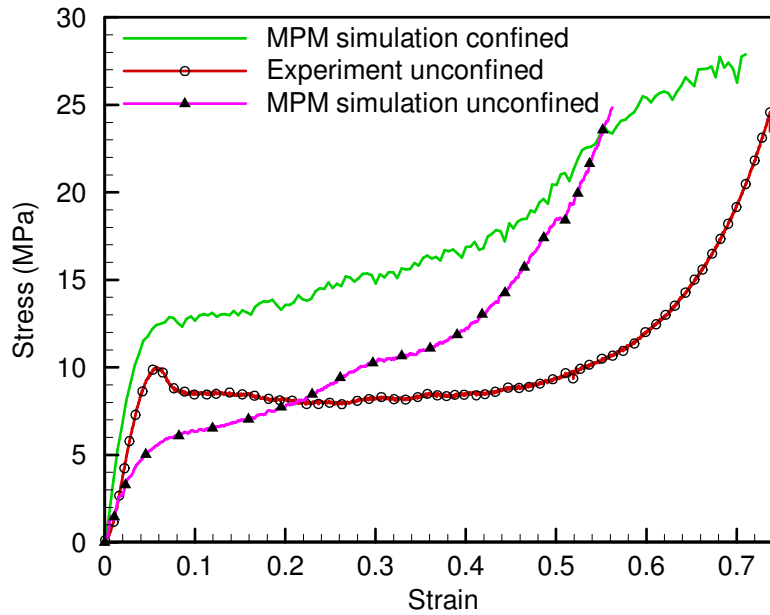
Figure 4.14: Comparison of stress-strain curve obtained from numerical simulation using MPM between confined and unconfined foam in compression

A stress-strain response was also obtained from these experiments. MPM simulations were carried out for finding a RVE of Rohacell foam. Microstructural deformations obtained from simulations were qualitatively compared with experimentally observed deformation in 3D. The simulations were able to reproduce many of the features in the stress-strain curve and microstructural deformations observed in experiments. However, further work in foam compression is needed to close the gap between simulations and experiments.

## 4.6  Conclusions

In this work, the material point method (MPM) has been used to simulate the compression of foam using the actual microstructure determined from micro-computed tomography. The essential features of the stress-strain response have been reproduced by

simulating the foam microstructure without the use of any special hyperfoam constitutive material model. This method can handle deformations at large compressive strains (greater than 75 %) within the densification region.

A RVE of the foam was found to be seven times the average cell-size. The simulations of microstructure evolution, which occurred during deformation, were able to capture many features observed in the experiments, such as occurrences of localized elastic buckling even in the elastic regime of compression, collapse of cells on a weak zone, stretching and bending of cell-walls, and propagation of a compaction wave. Further analysis from the simulated deformation history indicated that, within the elastic regime of compression, not all the cell-walls take part in carrying the stress and only a certain number of walls carry a majority of the compressive load. From our simulations, 35 % of the material points carried 75 % of the compressive load.

Additionally, inverse problem solving methodology was employed with an attempt to determine the parent material properties by correlating the simulated foam stress-strain curve with the experimental curve using a bilinear hardening elastic-plastic constitutive material model with von Mises stress-based failure criterion. The predicted elastic modulus of 3.7 GPa reproduces satisfactorily the initial linear elastic region of the stress-strain curve. While simulations were capable of capturing features in foam compression, there are still differences between the simulated stress-strain response and the experimental results. With additional simulations, the MPM method has the potential to determine the optimal material parameters to represent the stress-strain relation and microstructure evolution by direct comparison with measurements. Thus it can provide an

accurate microstructure-property relationship to guide in foam microstructure design for

optimal mechanical performance.

CHAPTER V

MEASUREMENT OF MECHANICAL PROPERTIES OF SAND GRAINS

USING NANOINDENTATION

5.1  Introduction

Granular materials, such as sand, are conglomerates of discrete particles held together (but not bonded) with significant void space in between. They are unique in that they behave in some respects similar to the other familiar forms of matter, namely, solids, liquids, and gases and in other respects in a dissimilar form. For example, they pack like solids but flow like liquids. Like liquids, they take the shape of the container but unlike them they can adapt to a variety of shapes when they are free standing. Similarly, like gases, they are made of discrete particles with negligible cohesive forces between them. Like solid, they can support load, but unlike solids, they (almost) cannot support a tensile force. In view of their unique behavior, some consider granular materials as the fifth state of matter, alongside, solids, liquids, gases, and plasma. They cannot strictly be modeled as continuum, yet it is done by considering the movement of particles in the void space under load akin to the deformation and flow in solids.

Sand is formed largely by erosion and disintegration of larger rocks into particles by natural forces, such as wind, pressure, water, ice, friction, and heat. Over millions of years, such processes have led to the formation of sand of various grain sizes ranging

from a fraction of a micrometer to several hundred micrometers. Investigation of the mechanical behavior of sand from granular (meso scale) to macro (continuum) scale can contribute towards a fundamental understanding of the underlying mechanisms of deformation, flow, and fracture of granular materials under load and ultimately realize the underlying science-base for large scale phenomena, such as the motion of an impacting solid with sand, and the size (typically a few mm) of the influential shearing zones in tectonic plates in sliding during earthquakes and landslides.

Mechanical properties of sand grains, such as the Young's modulus, hardness, fracture toughness, and stress-strain relations are of particular importance since their individual behavior dictates the overall behavior of the sand at macroscale. Moreover, the mechanical properties of the grains can vary with the mineral composition of sand, size, defect structure, and crystal orientation. The effect of grain size is due to the fact that larger grains would contain higher number of defects in the form of voids and ridges as well as cracks which may yield mechanical properties different than the smaller grain sizes and hence cannot be directly used to imply the behavior of finer sand grains. As far as larger (on the order of a centimeter or more) sand particles (rocks) are concerned, measurement of their properties using tensile/compression testing machine can be carried out to determine their mechanical properties. However, small sand grains can hardly be tested in compression or pulled in tension for measurements of mechanical properties due to difficulties involved in holding the specimen or in the preparation of the sample.

For the past two decades, nanoindentation has been used for measurement of mechanical properties of different types of materials (e.g. elastic, viscoelastic). The instrumented nanoindenter is widely accepted as a standardized testing method for

94

characterization of properties for elastic-plastic materials. The resolution in such a testing can reach a fraction of nanometer in displacement and µN in load. The added advantage of such testing is that in some cases, wherein the materials exhibit length scale dependent properties, it becomes possible to characterize such materials and extract the moduli and hardness at different depths of indentation and the material properties extracted will be a function of the maximum indentation depth reached or the deformation zone beneath the indenter tip. Such easiness in characterization of length-scale dependent material properties can be very challenging and tedious using conventional tensile testing procedures. Thus, extracting the material properties by indenting at depths less than 100 nm would essentially give mechanical properties at nanoscale. As a result, nanoindentation technique is widely used to extract mechanical properties of very small volume of materials, such as thin films, wires and coatings, MEMS, and NEMS components.

In this investigation, we used the nanoindentation technique to determine the nanoindentation force-displacement relation and extracted the mechanical properties, such as Young's modulus, hardness, fracture toughness, and stress-strain relationship of sand granules at microscale. We have conducted nanoindentations on several grains to assess the variance in the mechanical properties. Furthermore, by adopting an inverse methodology approach, i.e., by using the experimental load-depth information in combination with Finite Element (FE) numerical simulations, we predicted the stress-strain response of the sand grains. By using cube-corner indenter tip to induce cracks in the sand grain, we characterized the failure behavior of the sand particles.

## 5.2  Background

The mechanics of granular materials, such as sand, or particulate materials, has been an area of increasing interest in the past decade or so, due mainly to the challenges it poses in addressing this problem as well as the opportunities provided by the emerging technological instruments as well as the rapidly increasing computing power available that facilitates in addressing this difficult problem. However, this area still remains to be relatively insufficiently understood.

Considerable work had been reported in the literature on the mechanical behavior of sand. Poorooshasb *et al.*, (1966) and Lade and Duncan (1973) conducted triaxial compression tests on sand to determine the nature of deformation and attempted to describe it using a constitutive law. Triaxial compression tests were also carried out by others to investigate anisotropy (Arthur and Menzies, 1972), softening and preshearing effects (Lade and Prabucki, 1995), and shear band formation (Wang and Lade, 2001). Additionally, simple shear tests were conducted (Haythornthwaite, 1997) to determine shear locus of sand. However, for small systems of grain size scales, the stress is claimed to propagate in a manner described by wave-like (hyperbolic) equations (Goldenberg and Goldhirsch, 2005, Geng *et al.*, 2001, Oda *et al.*, 1980) rather than the elliptic equations of static elasticity. For small-scale systems, the localization of deformation (Desrues *et al.*, 1985), such as the formation of force-chains is more pronounced and deformation mechanisms at meso/micro scales need to be considered (Oda and Konishi, 1974).

Most of the literature on characterization of mechanical properties of sand or rocks has focused on either compressive behavior of sand as bulk or macroscale properties of rocks by pulling them in a tensile testing machine. For geomechanics applications and

96

simulations, it is necessary to know the mechanical properties of individual grains. There have been many efforts on characterizing mechanical behavior, including, failure behavior of rocks. For example, Liao *et al*. (1996) conducted direct tensile tests on transversely isotropic cylindrical argillite specimens and reported the stress-strain relationships. They determined the material properties and found significant variations depending on the amount and orientation of the micro-fissures. However, the data for larger rocks cannot be extended directly for individual sand grains mainly due to the difference in the length scales. The mechanisms of deformation and fracture in individual sand grains can be different from their larger counterparts. Ulm and Abousleiman (2006) conducted nanoindentation measurements on shales, a type of sedimentary rock, and concluded that shales are nanogranular composite materials with their mechanical properties dictated by particle-to-particle contact and packing density.

Nanoindentation provides an effective technique to measure the local material response in terms of hardness and Young's modulus at micro- and nano- length scales (for e.g. see Refs. Pethica *et al.*, 1983; Oliver *et al.*, 1986; Li and Bhushan, 2002; Pethica and Oliver, 1987). Methods for measuring the elastic-plastic properties, such as dynamic Young's modulus and hardness have been well established (Doerner and Nix, 1986, Oliver and Pharr, 1992). The wide acceptance of nanoindentation technique stems from the improvements in the technique incorporated by Oliver and Pharr (1992). They eliminated the need for knowing the residual indentation impressions. Instead, they used the unloading curve to extract the elastic properties of an elastic-plastic material, namely, elastic modulus and hardness. This method is very well established and has been implemented in commercial instrumented nanoindenters for use on elastic-plastic

materials. Inverse methodologies using numerical techniques in combination with experimental results have been developed effectively to predict the material properties and even the stress-strain relationships (Liu *et al.*, 2005). In addition to the measurement of elastic modulus and hardness, nanoindentation can also be used to determine the fracture toughness of brittle materials (Pharr *et al.*, 1993). This procedure was found to be adequate for estimating the fracture toughness in homogeneous materials.

In this investigation, we have carried out nanoindentation tests using a Berkovich indenter tip on several (~ 250) different sand grains of ~ 1 mm size and recorded the load-displacement data. Young's modulus and hardness were obtained directly from the MTS Testworks software output based on analysis of unloading segment using the method developed by Oliver and Pharr (1992). A representative stress-strain curve was obtained, corresponding to the average modulus obtained, for solving an inverse problem to determine the stress-strain curve using FEM. Nanoindents were also made using a cube-corner indenter tip to generate cracks for estimation of fracture toughness. In all the cases the indent impressions were obtained using Nanovision (MTS) setup. The lengths of the cracks developed were used to predict the range of fracture toughness values for the sand grains. Statistical analysis was conducted to determine the variability in the mechanical properties of sand grains.

5.3  Nanoindentation tests on sand grains

A sample of sand, collected locally, was washed and subsequently dried in an oven at ~ 55 ºC. It was sieved to collect sand grains of ~ 1 mm size. The sand grains were embedded in an epoxy matrix and mounted in a sample holder. The samples were cured

in an oven resulting in a composite of sand grains in a hardened epoxy matrix. Fig. 5.1 (a) shows sand grains embedded in an epoxy matrix exhibiting different colors due to differences in density, crystal orientation, defect structure, and mineral content. No particular analysis was carried out to determine the type of sand within this sample size, as the main objective of this investigation is to determine the mechanical properties of individual grains by nanoindentation. The samples were wet polished using an alumina abrasive powder (from Buehler Inc.) in a water slurry. To obtain a smooth surface suitable for nanoindentation, the maximum abrasive size used in the final polishing was 50 nm. Fig. 5.1 (b) shows a polished sand surface with different grains oriented in different directions. Small pits and ridges observed are attributed to the presence of defects within the sand grains.

An MTS Nano Indenter XP system was used for the nanoindentation measurements. This indenter can reach a maximum indentation depth of 500 μm and a maximum load of 500 mN. The displacement and load resolutions are 0.2 nm and 50 nN, respectively. Both Berkovich and cube-corner indenter tips, made of single crystal diamond, were used in this investigation. Nanoindentations were made on flat, polished sand grain surfaces under constant rate of loading. The applied load on the indenter tip was increased until it reached a user-defined value. At this point, the load may be held constant for a period or removed. Since, we do not extract any information from the hold segment of the cycle, the holding time in our experiments is zero. The load-displacement curves obtained thus would be characteristic for that particular sand grain. Analysis can be carried out on the load-displacement output to determine the mechanical properties of the sand grains. This is achieved, based on contact mechanics of nanoindentation.
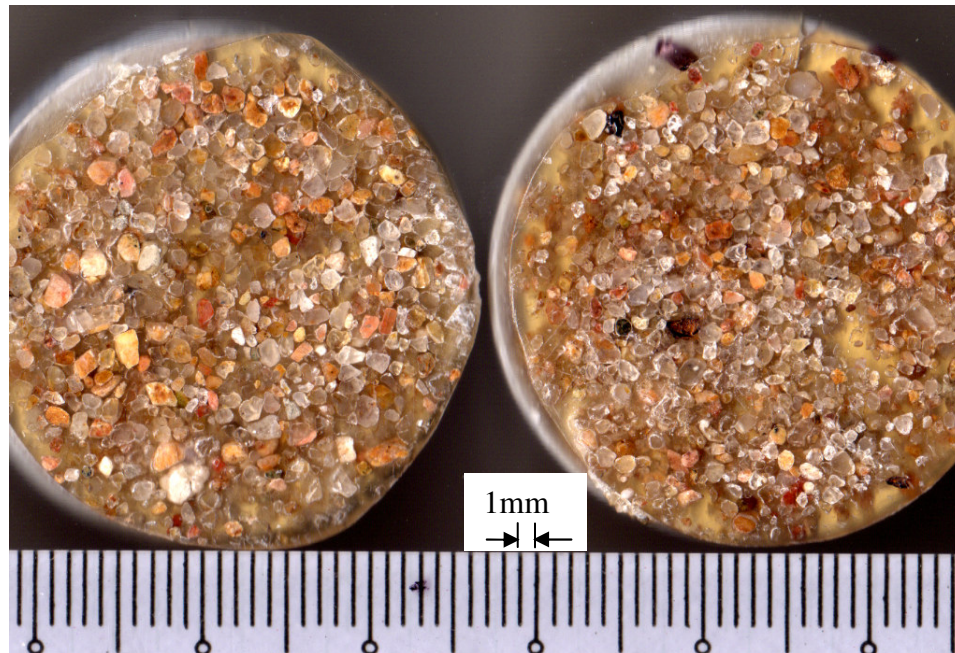
Figure 5.1 (a): Embedded sand grain samples in an epoxy matrix
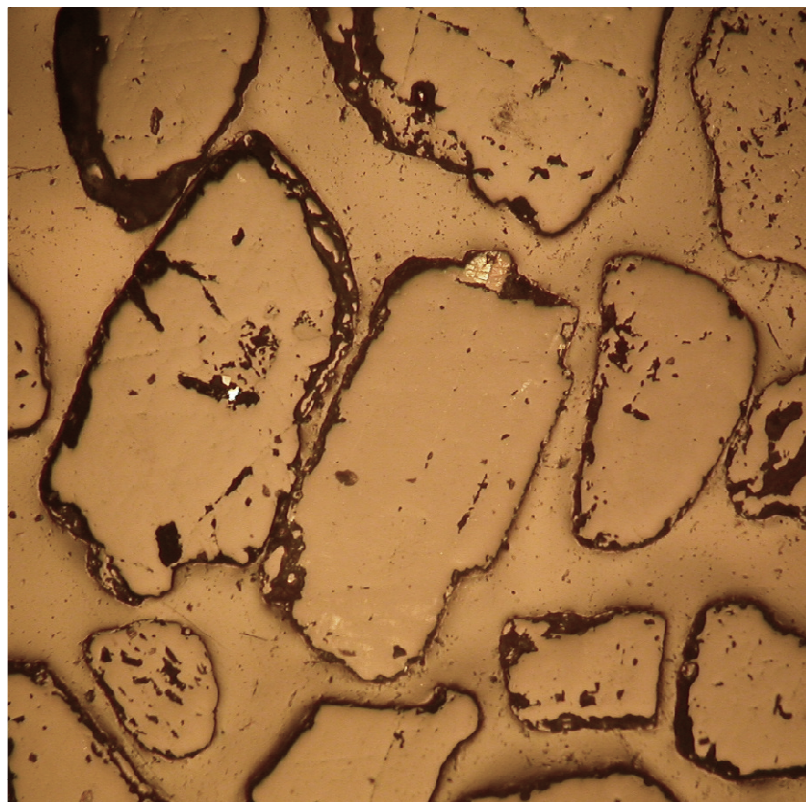


Figure 5.1 (b): Magnified image of polished sand grains in an epoxy matrix

Hardness ($H$) is obtained using,

$$H = \frac{P_{max}}{A_c} \tag{5.1}$$

where $P_{max}$ is the maximum indentation force and $A_c$ is the contact area corresponding to the contact depth ($h_c$) at maximum load, and is calculated based on the tip area function. The modulus of the specimen ($E$) is obtained using (Oliver and Pharr, 1992),

$$\frac{1}{E_r} = \frac{1-v_s^2}{E_s} + \frac{1-v_i^2}{E_i}, \tag{5.2}$$

where $E_s$ and $v_s$ are the Young's modulus and Poisson's ratio of the specimen, respectively, while $E_i$ and $v_i$ are the Young's modulus and Poisson's ratio of the indenter tip (made up of diamond), respectively. Due to finite stiffness of the indenter tip, its modulus has to be considered in the expression for the calculation of specimen modulus from the contact stiffness. The contact stiffness, $S$, is provided by the slope of the initial unloading curve. Thus,

$$S = \frac{dP}{dh} = \frac{2}{\sqrt{\pi}} E_r \sqrt{A_c(h_c)} \tag{5.3}$$

Eqns. (5.2) and (5.3) along with the known values of the area function, slope of the unloading curve, and modulus and Poisson's ratio values for the indenter tip can be used to determine the elastic modulus for a specimen corresponding to its Poisson's ratio.

5.4  Results and Discussion

5.4.1  Young's modulus and hardness of sand grains

For measurement of modulus and hardness, a force was applied by the nanoindenter using a Berkovich tip on the sand grain. Fig. 5.2 (a) shows an inverted image (3D) and a

typical nanoindentation residual impression obtained using Nanovision, a part of the MTS Nanoindenter system. The inverted image enables the determination of the depth of the indent more accurately and delineates its topographical features. Fig. 5.2 (b) shows a typical nanoindentation load-displacement curve. Nanoindentations were carried out under load-control, in which the indenter-tip was pressed onto the sample and the load on it was increased (linearly). The initial part of the load displacement curve, characterized by an increase in the load from zero to maximum load is termed, the loading segment. Once the user-defined maximum load was reached, the load was removed, again in a controlled manner (linearly) and is termed, the unloading segment. Fig. 5.3 shows residual indent impressions from a Berkovich tip for maximum loads varying from 100 mN to 400 mN. These indents were carried out at different locations on the sand grain. It can be seen, in general, as the maximum load increases, the corresponding indent sizes increases. It can also be seen that no cracks were formed when indented with a Berkovich indenter-tip. Hence, the continuum approximation can be applied and Eqns. (5.1) to (5.3) can be used to determine the modulus and hardness of the samples.

In order to determine the variability in properties over a single sand grain (size ~ 0.7 mm), nanoindentations were carried out for a sand grain having the same maximum load. Figs. 5.4 (a) and 5.5 (a) show histograms of the distribution of Young's modulus and hardness, respectively, for a single sand grain. Figs. 5.4 (b) and 5.5 (b) show Weibull plots for the data obtained on Young's modulus and hardness, respectively. The median value (corresponding to P50 probability) for Young's modulus and hardness are 66.9 GPa and 10.74 GPa, respectively.
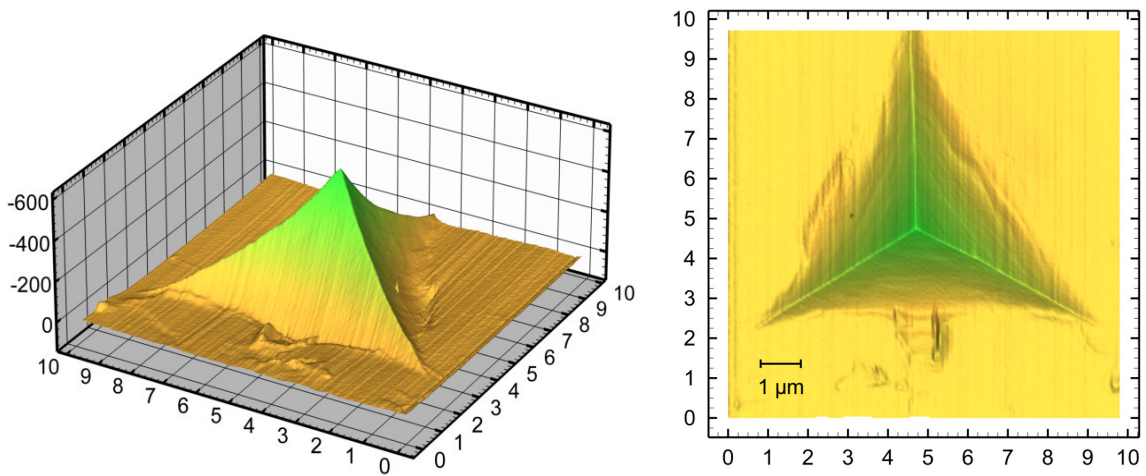
(a) 3D inverse image and 2D residual indent impression from nanoindentation.
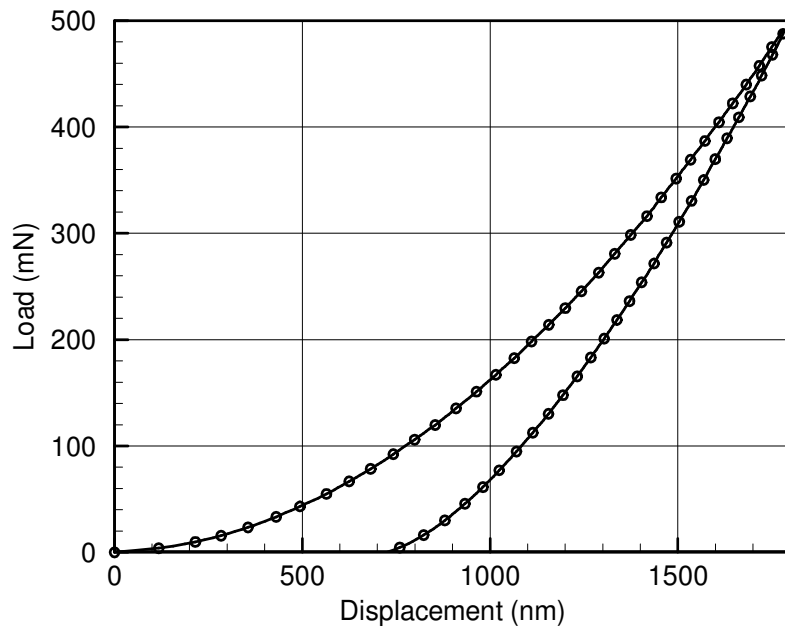


(b) Load-displacement relationship

Figure 5.2: Typical results from nanoindentation test on sand grain using Berkovich tip
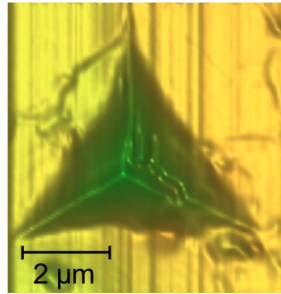
(a) 100 mN
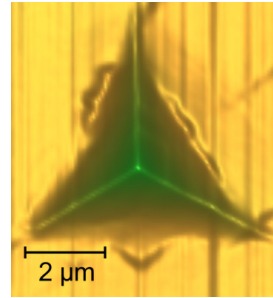
(b) 150 mN
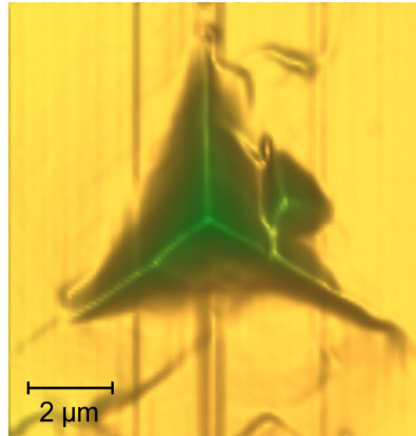
(c) 200 mN
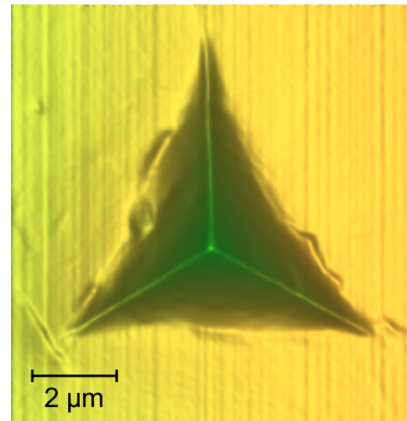
(d) 300 mN
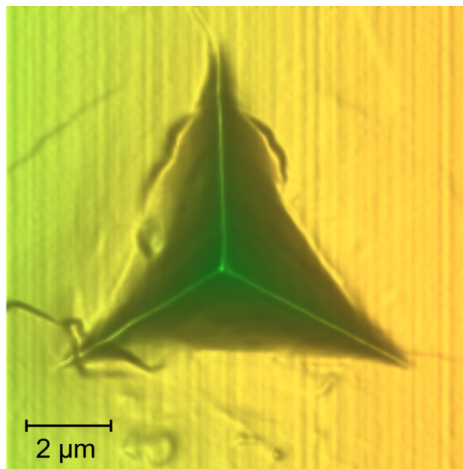
(e) 350 mN
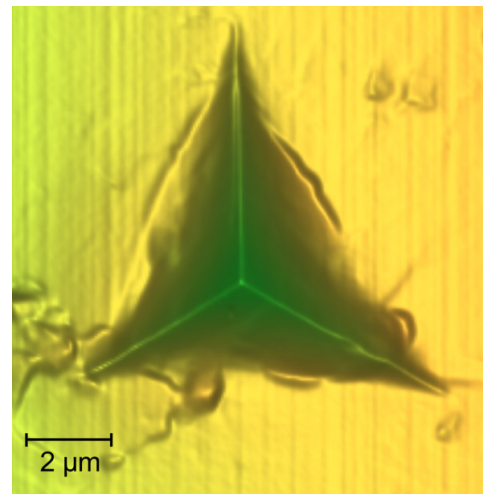
(f) 400 mN

Figure 5.3: Residual indent impressions from Berkovich tip for maximum loads from 100 to 400 mN
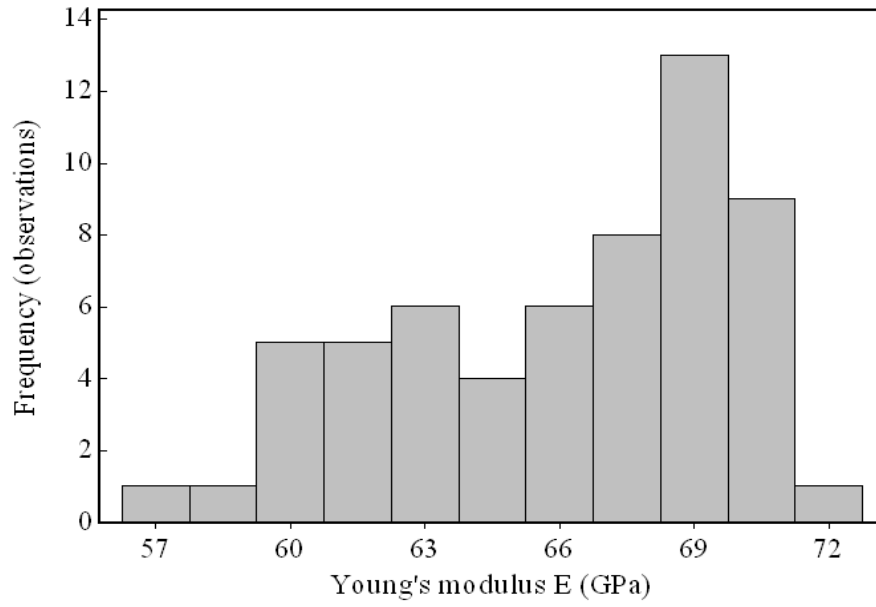
Figure 5.4 (a): Distribution of Young's Modulus for nanoindentations on a single sand grain
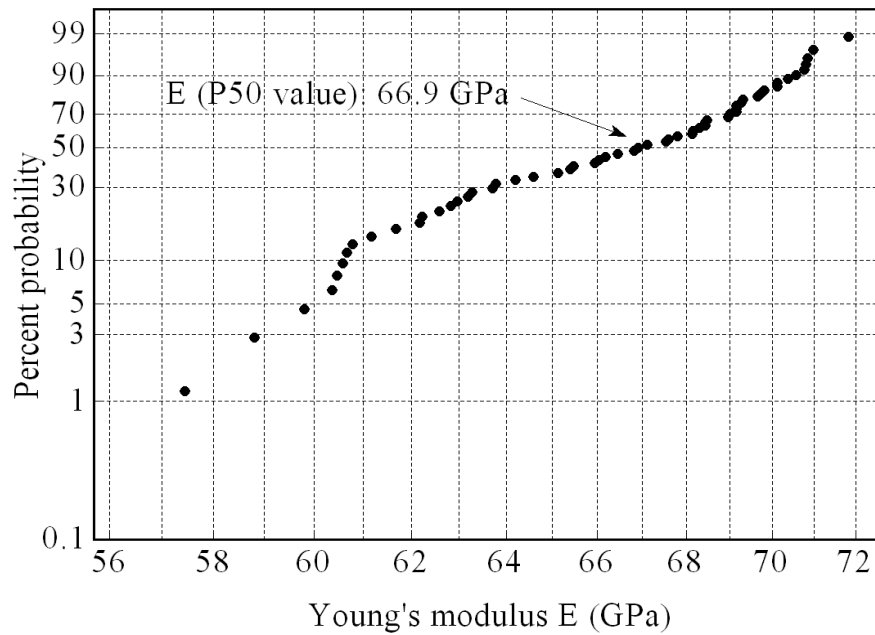


Figure 5.4 (b): Weibull plot for the Young's modulus for nanoindentations on a single sand grain

105
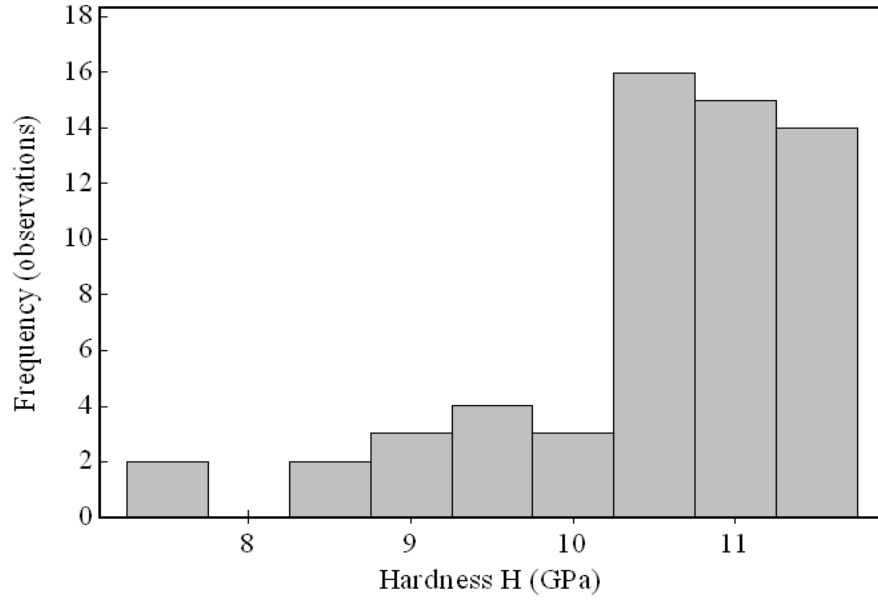
Figure 5.5 (a): Distribution of hardness for nanoindentations on a single sand grain
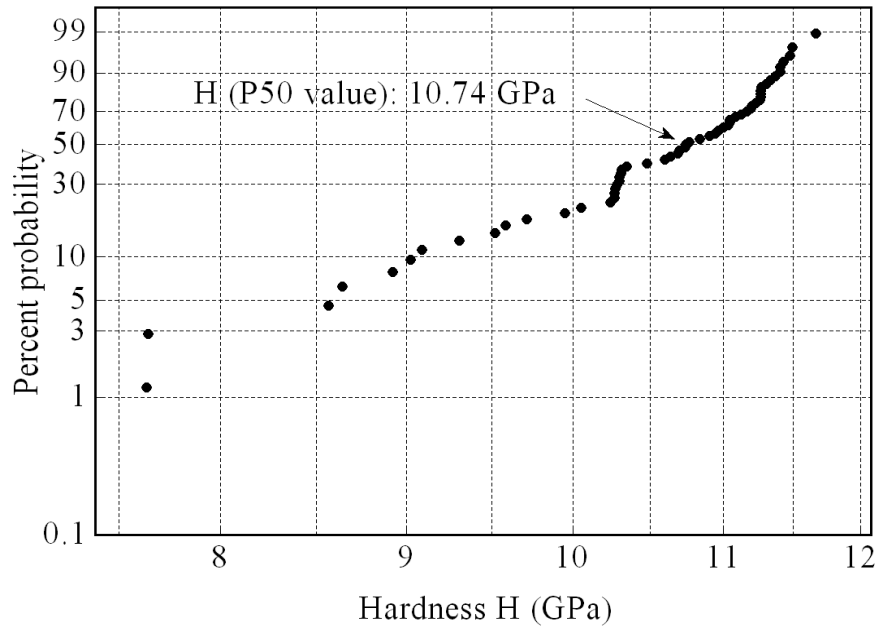


Figure 5.5 (b): Weibull plot for hardness for nanoindentations on a single sand grain

106

The variations in the measured modulus and hardness at different locations, in Figs. 5.4 and 5.5 are attributed to the anisotropy and heterogeneity in the sand grain.

Once an estimate was obtained for a single grain (of representative size ~ 0.7 mm), nanoindentations were carried out on 250 different grains with two tests per grain. The results from the two tests were averaged and taken as the mean value for that grain. Young's modulus and hardness were obtained using the slope of the unloading curve and the values of load and contact area at maximum indentation depth. These were a direct output from the nanoindentation software. The distributions of modulus and hardness values are plotted in Figs. 5.6 and 5.7, respectively. Using Weibull distribution function, we determined the median value (corresponding to P50 value) for Young's modulus of the sand to be 90.1 GPa (range 41.4 to 115.8 GPa) and hardness to be 10.7 GPa (range 5.4 to 13.7 GPa). Scatter in the data is attributed to different types of sand grains due primarily to variations in the material constituents, defect structure, and crystal orientations.

## 5.4.2   Stress-strain response of sand grains

The solution for the indentation problem has been well established (Prandtl, 1920; Hill *et al.*, 1947; Ishlinskii, 1944; Shield, 1955; Tabor, 1970; Johnson, 1970). Inverse methodologies, which use experimentation in combination with numerical techniques to aid in characterizing the material properties are used in situations where it is difficult to extract the properties using analytical solutions alone due to non-linearities or complexity in material, geometry and loading conditions. In such cases, it is easier to simulate the equivalent model using a numerical method, such as Finite Element Method (FEM).
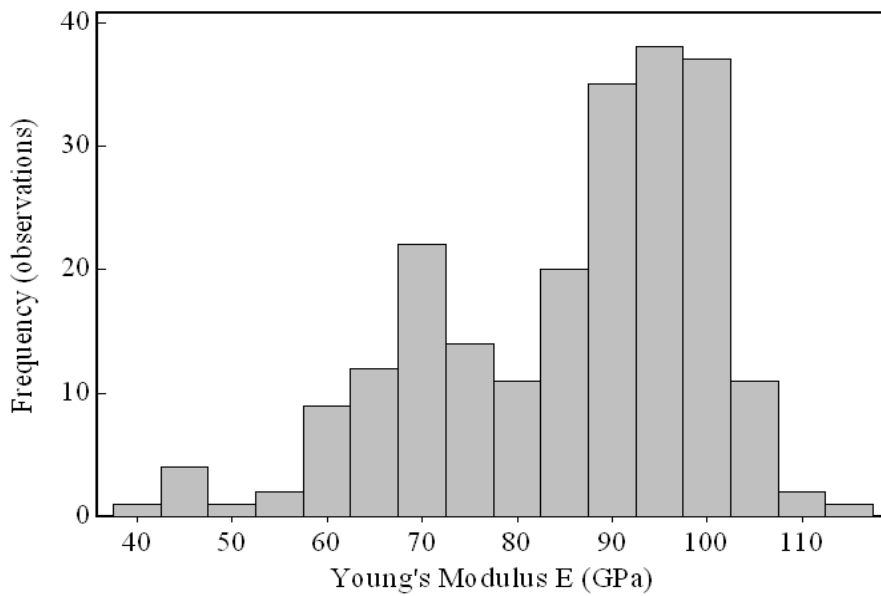
Figure 5.6 (a): Distribution of Young's Modulus for nanoindentations on different sand grains
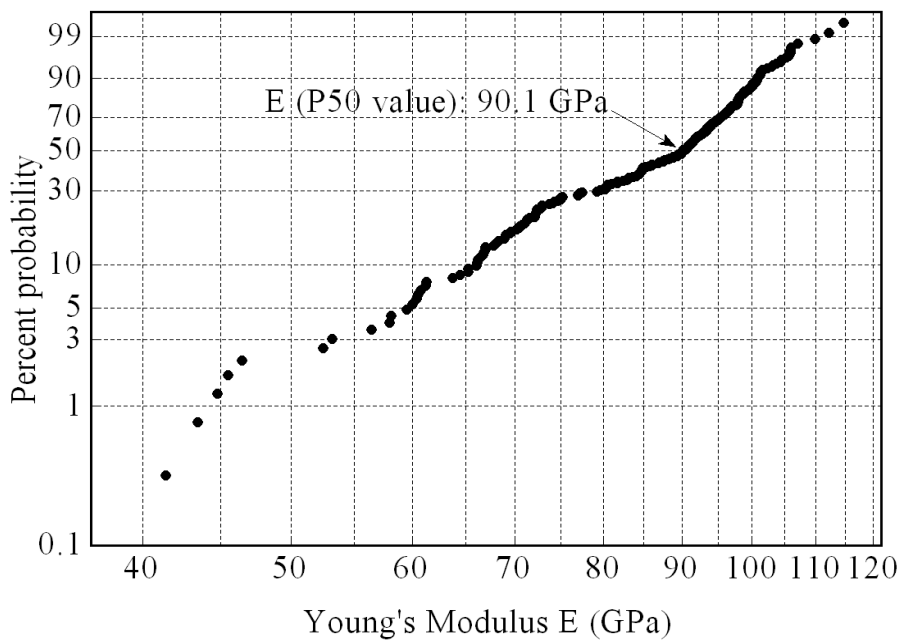


Figure 5.6 (b): Weibull plot for the Young's modulus from nanoindentations on different sand grains

Figure 5.7 (a): Distribution of hardness for nanoindentations on different sand grains
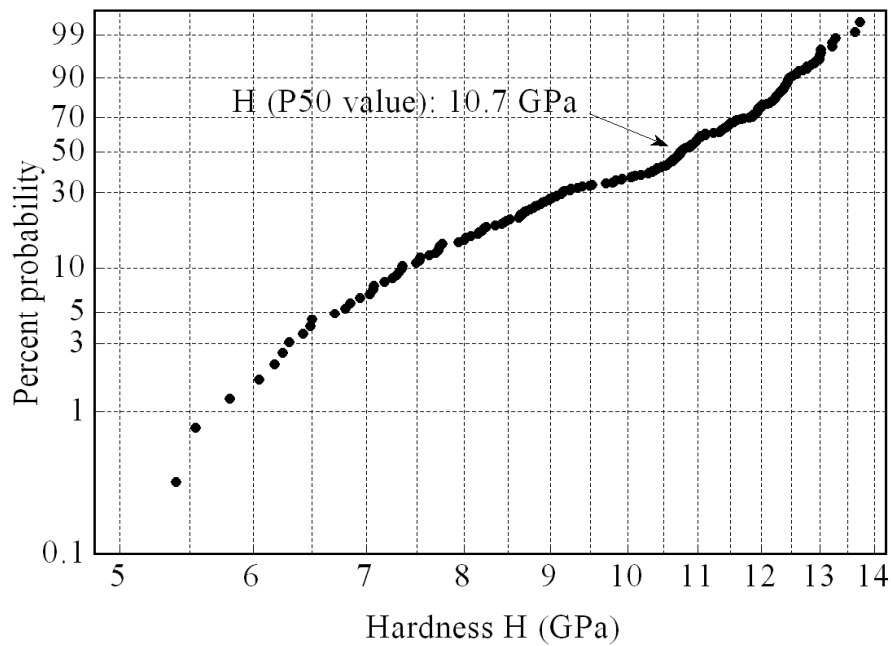


Figure 5.7 (b): Weibull plot for the hardness from nanoindentations on different
    sand grains

Initially, we can start with certain assumed values of material parameters for e.g. plastic flow. The values are adjusted so that numerical results obtained can be comparable with the experimentally obtained values, for e.g. by comparing the load-displacement curves, in the case of nanoindentation. It may be noted that FEM has been applied successfully in the simulation of nanoindentation problem (Bhattacharya and Nix, 1988, 1991; Wang and Bangert, 1993; Sun *et al.*, 1995; Lichinchi *et al.*, 1998; Fivel *et al.*, 1998; Knapp *et al.*, 1998).

For determining the stress-strain relationship for granular sand, nanoindentation was modeled using FEM. To predict the elastic-plastic properties, von Mises yield criteria was used along with isotropic hardening to simulate the deformation characteristics of a sand grain. The plastic behavior under compression was approximated by a power law as

$$\sigma = R\varepsilon^n, \qquad \text{for } \sigma \geq \sigma_y \tag{5.4}$$

where $n$ is the strain hardening exponent, $R$ is the strength coefficient, and $\varepsilon$ is the equivalent strain, $\varepsilon = \sqrt{\varepsilon_{ij}\varepsilon_{ij}} = (\varepsilon_y + \varepsilon_p)$, where $\varepsilon_y$ is the yield strain and $\varepsilon_p$ is the plastic strain. The von Mises equivalent stress is given as, $\sigma = \sqrt{\dfrac{3}{2}\sigma_{ij}\sigma_{ij}}$ .

Within the elasticity limits,

$$\sigma = E\varepsilon, \text{ for } \sigma \leq \sigma_y \tag{5.5}$$

where $E$ is the Young's modulus.

From (4) and (5), we get

$$\sigma = \sigma_y \left(1 + \frac{E}{\sigma_y}\varepsilon_p\right)^n, \text{ for } \sigma \geq \sigma_y \tag{5.6}$$

ABAQUS standard was used to perform the calculations, assuming finite deformation characteristics. The von Mises yield criteria can be written as

$$(\sigma_1 - \sigma_2)^2 + (\sigma_2 - \sigma_3)^2 + (\sigma_3 - \sigma_1)^2 = 2\sigma_y^2 \tag{5.7}$$

where, $\sigma_1$, $\sigma_2$, and $\sigma_3$ are the principal stresses and $\sigma_y$ is the yield strength measured in uniaxial tension test.
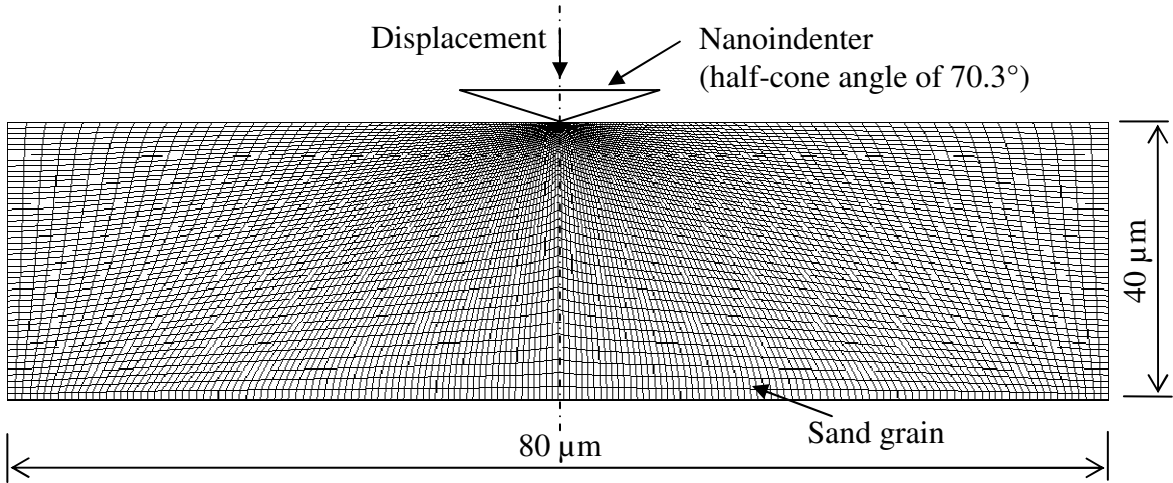


Figure 5.8: Axisymmetric Finite Element Analysis model for nanoindentation

The configuration for the FEM simulation of nanoindentation is shown in Fig. 5.8. The Berkovich indenter was approximated to an equivalent conical indenter with a half-cone angle of 70.3°. This value was obtained by equating the Berkovich tip cross-sectional area as a function of depth equals to that of a conical indenter (Fischer-Cripps, 2002). The displacement history from the experiment was given as input for the Finite Element (FE) analysis. Poisson's ratio was taken as 0.17. The output of the FE analysis was the resulting reaction force or load. This numerical load was plotted versus the displacement into the surface, to give load-displacement curve from the simulation. The mesh size selected was tested for convergence of the load-displacement curve.

111
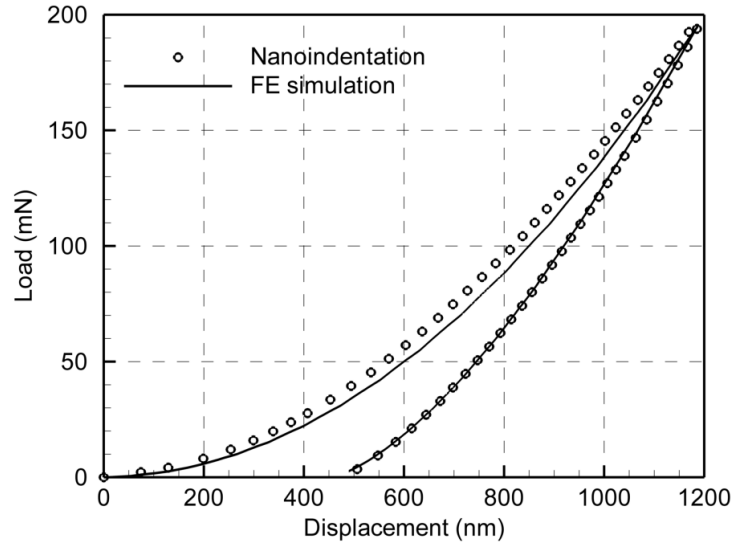
Figure 5.9 (a): Comparison of load-displacement curves from nanoindentation and
FE simulation
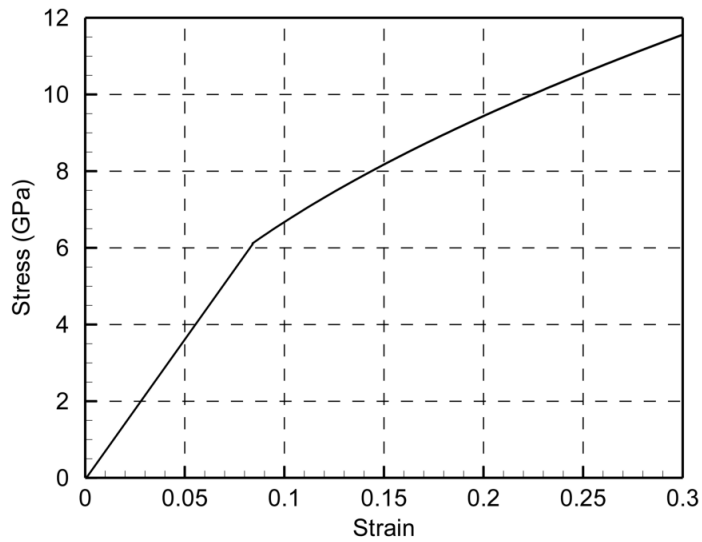


Figure 5.9 (b): Stress-strain curve (in compression) from FE simulation

The numerical values of the load-displacement curve were compared with the
experimental and the measure of fit was carried out by minimizing the least squares
correlation coefficient. In order to obtain a better fit, the initial assumed values were so
adjusted as to minimize the least squares correlation coefficient. Thus, the material

parameters were adjusted until good agreement was reached between experimental and numerical data. The best-fit parameters were then used to determine the stress-strain relationship for the sand grain sample.

It should be noted, the maximum strain up to which the stress-strain curve is valid, using this approach, is limited by the strain produced by the nanoindentation test [see Ref. Dao *et al.*, 2001)]. No cracks were observed by examining the indent impressions (for Berkovich indenter tip) obtained from Nanovision. Thus, the continuum plasticity material model was justified. As stated earlier, we used an inverse problem solving approach to determine the stress-strain relationship of sand at granular level by correlating the FEM simulated nanoindentation load-displacement data with the measured results. Fig. 5.9 (a) shows the fitting obtained using the FEM simulation (obtained using ABAQUS-Standard) to the representative experimental data. The predicted stress-strain response [Fig. 5.9 (b)] is represented in the form of power-law model and the parameters obtained were $n = 0.5$ and $\sigma_y = 6.1$ GPa.

### 5.4.3 Fracture toughness of sand grains

When a brittle material is loaded by a sharp indenter with sufficient load, radial cracks propagate out of the indenter corners. In such a case, the fracture toughness can be estimated by measuring the length of the radial cracks produced at a given indentation load. In order to understand the failure behavior of the sand grains, a cube corner indenter was used to indent into a polished sand grain to initiate cracks at the corners of three edges of the tip.

It is well known that sand grains would generally behave in a brittle material under load. In order to estimate the fracture toughness, a formula derived by Pharr *et al.* (1993) was used,

$$K_C = \alpha \left( \frac{E}{H} \right)^{0.5} \left( \frac{P}{c^{3/2}} \right) \tag{5.8}$$

where α is an empirical constant which takes into account, the geometry of the indenter tip (for a cube-corner tip $\alpha = 0.032$). Before proceeding with the nanoindentation on sand grains, a sample test was run on a standard fused silica sample. The average value for fracture toughness obtained was 0.6 MPa-m$^{0.5}$ which is in reasonable agreement with the value of 0.5 MPa-m$^{0.5}$ reported for fused silica by Harding (1995).

For sand, the values of the elastic modulus ($E$) and hardness ($H$) were obtained using the Berkovich nanoindenter tip prior to indenting with a cube-corner tip (see Sec. 4.1). Since we are interested in the ratio of $E/H$ from the nanoindentation tests, we obtained an average value for the ratio as 8.5. In Eqn. (5.8), $c$ is the crack length and can be determined from the surface scans obtained (two of the scans along with inverse images) are shown in Figs. 5.10 (a) and (b). Both 3D inverse images and 2D nanoindentation residual images are shown for details on the crack formation and fracture. It may be noted that due to slight errors in the alignment and inhomogeniety of the sand grain, it is rather difficult to get all the three cracks to be of equal length. When there are differences between the crack lengths from the same indent, we have taken the average crack length for a particular indent. The histogram of the fracture toughness values obtained is shown in Fig. 5.11 (a) and the Weibull distribution in Fig. 5.11 (b). From the Weibull distribution, median value for the fracture toughness observed was 1.77 MPa-m$^{0.5}$ (range 0.8 to 3.6 MPa-m$^{0.5}$).
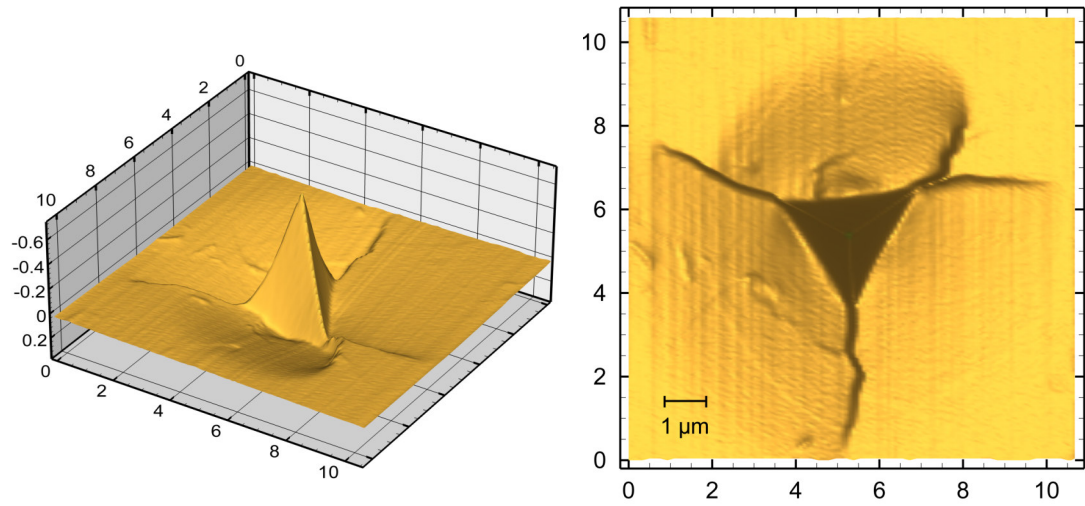
(a) At maximum load of 80 mN
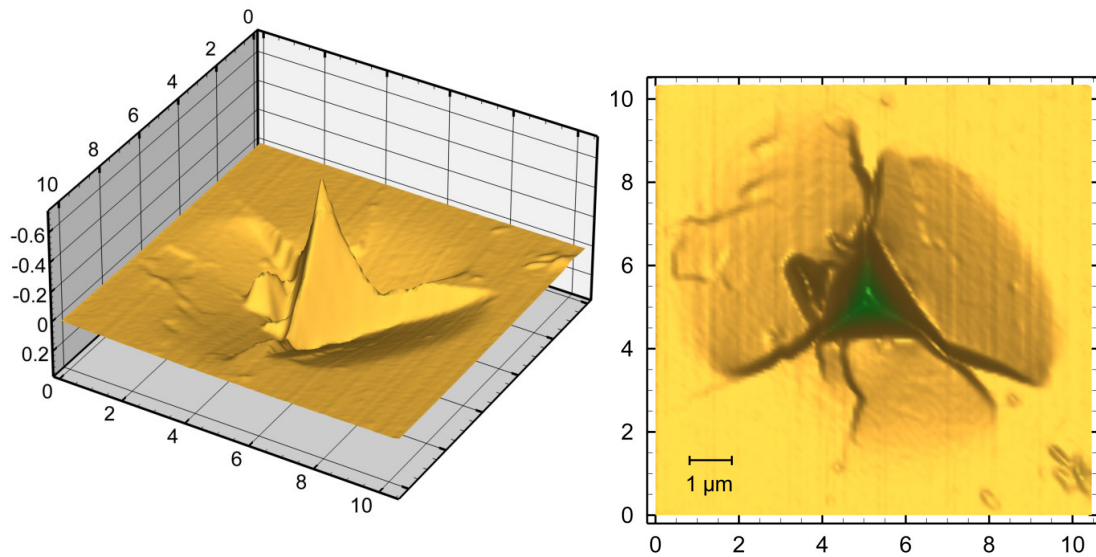


(b) At maximum load of 70 mN

Figure 5.10: 3D inverse image and 2D residual surface profile showing cracks generated after nanoindentation using a cube corner tip
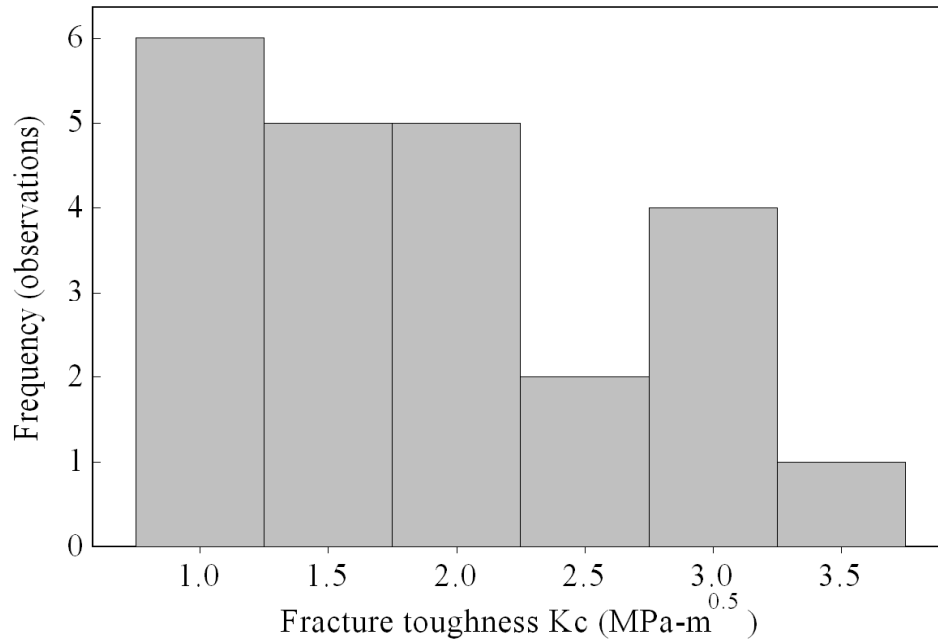
Figure 5.11 (a): Distribution of fracture toughness for nanoindentations on
different sand grains
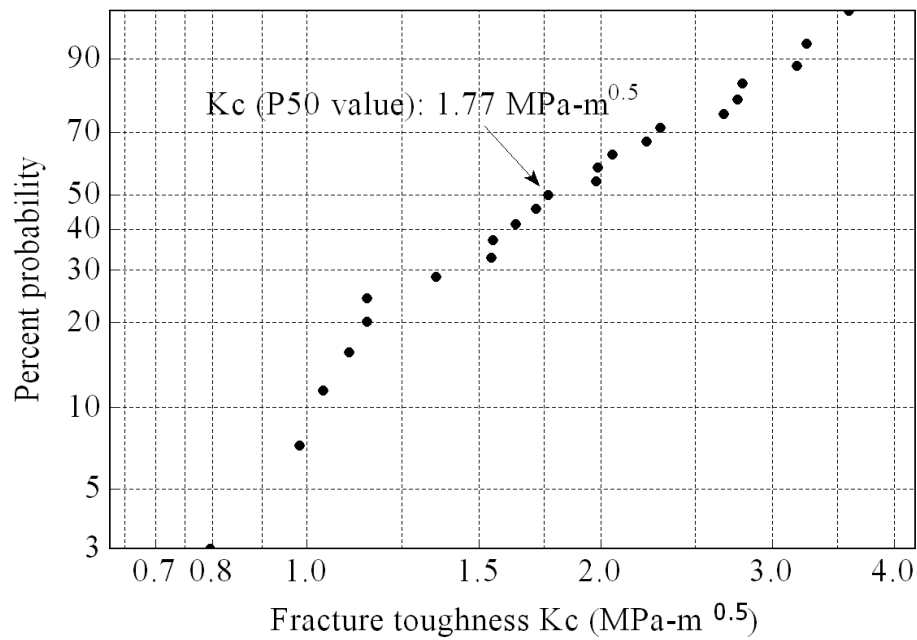


Figure 5.11 (b): Weibull plot for fracture toughness from nanoindentations on
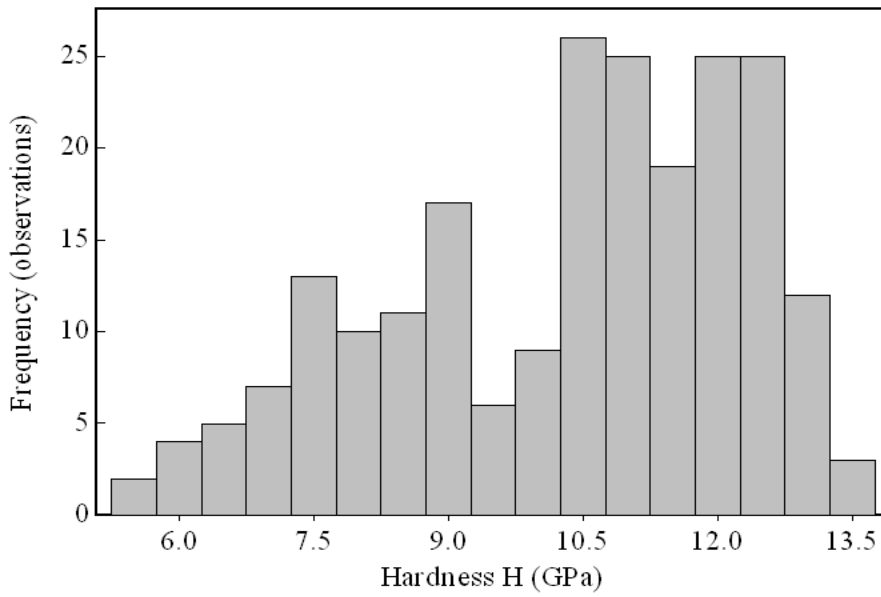different sand grains
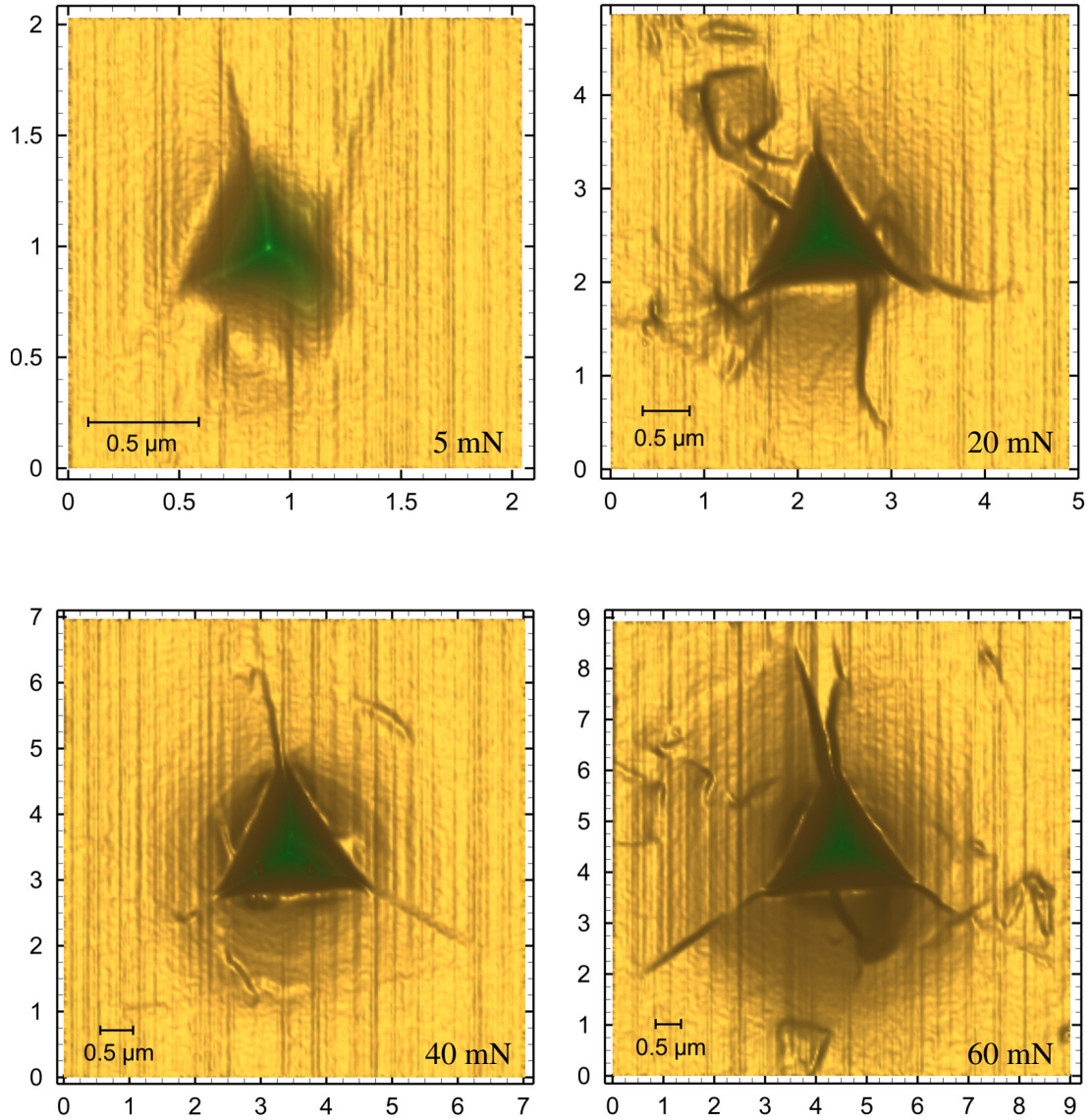
Figure 5.12: Surface profile showing cracks generated under different loads using nanoindentation (cube corner tip), at different locations on a sand grain

117
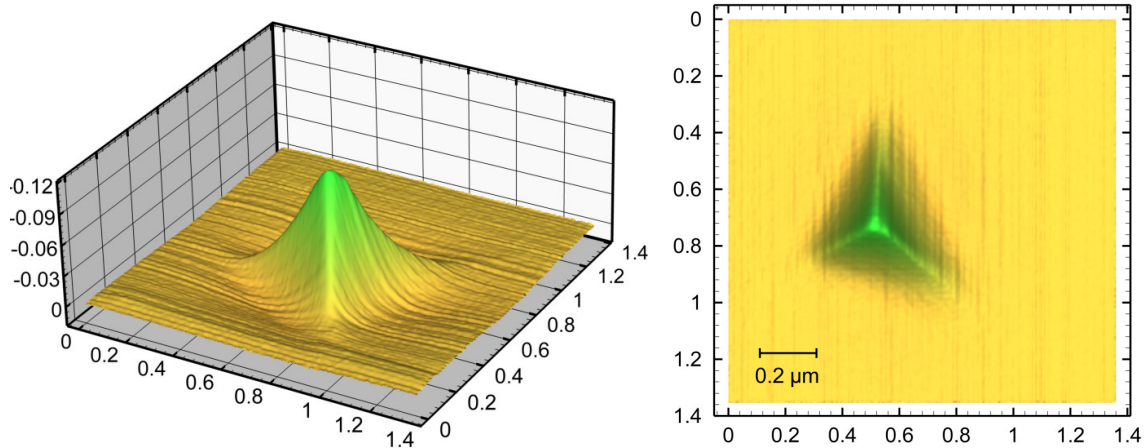
Figure 5.13: Inverse image of nanoindentation on a sand grain at 5 mN load using a cube corner nanoindenter tip.

Indentations were also made on a sand grain with different maximum loads. Fig. 5.12 shows the cracks generated after indentation under different maximum loads at different locations on a same sand grain. Theoretically, for an isotropic homogeneous brittle material, one can expect consistent increase in the crack length as the maximum load increases as well as formation of straight cracks. However, the cracks observed on sand grains were not exactly straight. This is attributed to the inhomogeneity even within a single sand grain, such as presence of defects and different crystal orientations. Additionally, not all the sand grains exhibit the same tendency for producing cracks.

Fig. 5.13 shows a 3D inverse image of nanoindentation on a sand grain using a nanoindenter with a cube corner at 5 mN load. No cracks can be seen and indentation clearly shows the flow lines from the surface down to the bottom of indentation indicating ductile flow in a nominally brittle material. This may be the minimal load below which the sand grains behave in a ductile manner with a possible size-effect implications. Further studies are needed to confirm this hypothesis.

## 5.5  Conclusions

In order to assess the granular level mechanical behavior of sand, nanoindentation tests were conducted on individual sand grains to characterize their mechanical properties, namely, Young's elastic modulus, hardness, fracture toughness, and stress-strain relationship. As can be expected, a wide variation in the granular properties of sand was observed. Representative Young's modulus for the sand grains was found to be 90.1 GPa (range 41.4 to 115.8 GPa), hardness to be 10.7 GPa (range 5.4 to 13.7 GPa), and fracture toughness to be 1.77 MPa-m$^{0.5}$ (range 0.8 to 3.6 MPa-m$^{0.5}$). Power-law was used to represent the homogenized and isotropic stress-strain behavior for sand at the granular level. However, the variation in the property value indicates that sand at granular level is very inhomogeneous and not isotropic due to different material constituents, defect structure, and crystal orientations. Need exists to establish the link between nanoindentation measured properties of sand grains with the observed macro properties for correct prediction of bulk behavior of sand. The data reported here can be used for meso scale (granular) simulations of sand in which the individual sand grains would have different properties with the distributions obtained in this study.

CHAPTER VI

CONTACT ALGORITHM IN MATERIAL POINT METHOD FOR SIMULATION OF
GRANULAR MATERIALS

6.1   Introduction

The mechanics of granular materials, such as sand, or particulate mechanics, has been an area of increasing interest in the past ten years, due mainly to the challenges it poses in addressing various problem as well as the emerging technologies, such as μ-CT, X-ray radiography, and laminography and rapidly increasing computing power available that facilitates in addressing the mechanical behavior of granular matter. However, this area remains to be relatively insufficiently understood.

Investigation of the mechanical behavior of sand from micro- (meso scale) to macro (granular level) can enable us to contribute towards a fundamental understanding of the underlying mechanisms of deformation, flow, and fracture of granular materials under load and ultimately realize the science behind large scale phenomena, such as the motion of an impacting solid with sand, and the size (typically a few mm) of the influential shearing zones in tectonic plates in sliding during earthquakes and landslides. To investigate the trajectory of an impacting solid with sand, it is essential to understand the mechanical behavior of sand under pressure and deviatoric stresses. Due to the loosely connected nature, sand cannot sustain any tensile load and has relatively low shear

strength compared to compressive strength. This feature, in combination with the irregular shape of individual sand grains, allows an impacting object to sometimes deviate from initial impacting trajectory. Understanding and characterizing such asymmetric mechanical behavior of sand requires consideration of sand from granular scale to conglomerate of sand (micrometer scale for finer granules) and up to continuum and even at geological scales. This requires extensive experimental and numerical simulation work to determine the mechanical behavior of sand.

6.2 Background

Simulations of granular materials has been a challenging problem in different disciplines. Material point method (MPM) has been used to simulate the behavior of granular materials under different loading conditions. Bardenhagen *et al.* (2000) applied MPM to investigate the stress distribution in sheared granular material using simulations at meso scale. A contact algorithm was used to define the interaction between grains and model friction between them. Wieckowski (2004) used MPM for granular flow in a silo while filling and discharging, using elastic-viscoplastic constitutive material model with the Drucker-Prager yield criteria and non-associative flow rule. Due to the advantage of combined Eulerian and Lagrangian schemes, MPM was found suitable for many engineering problems, including penetration, impact, and large rotations of solid bodies which otherwise would cause severe numerical problems in purely Lagrangian methods, and thus a suitable candidate for simulation of sand at meso scale.

In this part of the current investigation, a contact algorithm is implemented in MPM to enable it to handle slip and friction between bodies in contact. Verification of the

implementation is carried out using simulations of a rolling sphere over an inclined plane. A new methodology is used to update the normals required for contact algorithm in MPM, which uses gradients of displacements. In MPM, during the process of discretizing geometries, especially the ones involving curved surfaces (for e.g. sphere), the resulting discretized surface loses information (original surface geometry), depending on the size of the background mesh used. In this investigation, the method used of calculating normals in the deformed and undeformed configurations considers the original geometry of the bodies. Velocity gradients are used to update the normals, which confirms with the deformation of the geometric surface. No complicated neighbor search algorithms or surface fittings are required for successive MPM steps, and it thus saves computational time as compared with other algorithms reported in the literature.

6.3 Methodology of contact algorithm at granular level:

During motion, sand cannot sustain tensile stresses. Furthermore, sand grains cannot penetrate into each other, but are allowed to separate. In the simulation of discrete particulate matter, we have used the contact algorithm developed for MPM by Bardenhagen, *et al.* (2000, 2001). The grains would be first discretized into a collection of material points in a single valued velocity field for calculation using MPM computation as described in Chapter II. Through this computation the velocity field will be determined and is designated as center-of-mass field $v_i$ at node $i$. The velocity of each material point on the grain is given as $v_i^g$ with $g$ ranging from one to the total number of grains, $N_g$, and $i = 1, \ldots, N_n$ indicate the number of nodes. Only those nodes in the neighborhood of the grain will have meaningful velocity and the grain velocity at other

nodes will be zero. Let $\boldsymbol{n}_i^g$ be the unit outward normal vector at grid points along the grain boundary. When one grain approaches the other, the two velocity fields $\boldsymbol{v}_i^g$ and the center-of-mass field $\boldsymbol{v}_i$ will be different. Consequently, the contact can be defined when the two velocities differ, given by the condition (Bardenhagen *et al.* 2000)

$$\left(\boldsymbol{v}_i^g - \boldsymbol{v}_i\right) \cdot \boldsymbol{n}_i^g > 0, \tag{6.1}$$

which indicates that the grain velocity is overtaking the center-of-mass velocity along the normal to the surface. Once this condition is satisfied, the grain velocity is adjusted to a new value $\bar{v}_i^g$, so that

$$\bar{\boldsymbol{v}}_i^g \cdot \boldsymbol{n}_i^g = \boldsymbol{v}_i \cdot \boldsymbol{n}_i^g \tag{6.2}$$

holds. That is, the normal component of the grain velocity is set equal to the normal component of the center-of-mass velocity. Since the center-of-mass velocity does not allow interpenetration of the grains in MPM simulation, this choice of contact is natural. The constraint in velocity at the interface can be converted to normal force that will be applied to the grain for computation to proceed to the next computational step. A normal force magnitude equivalent to the Eqn. (6.2), which can be applied to the grain is given as

$$f_{n,i}^g = -m_i^g \left[\left(\boldsymbol{v}_i^g - \boldsymbol{v}_i\right) \cdot \boldsymbol{n}_i^g\right] / \Delta t. \tag{6.3}$$

Here, $m_i^g$ is the nodal mass corresponding to the particles making up the grain $g$, and $\Delta t$ is the simulation time-step. In the case of frictionless slip, no tangential contact force is induced. Therefore, the net contact force at the node is given by

$$\boldsymbol{f}_{g,i}^{cont} = f_{n,i}^g \boldsymbol{n}_i^g, \tag{6.4}$$

and can be applied for each grain in contact at the node to form a net force vector as

$$\dot{\boldsymbol{p}}_i = \boldsymbol{f}_i^{int} + \boldsymbol{f}_i^b + \boldsymbol{f}_i^\tau + \boldsymbol{f}_i^{coh} + \boldsymbol{f}_{g,i}^{cont}. \tag{6.5}$$

123

In the presence of friction, the frictional slip is accomplished by adjusting the tangential component of grain velocity. In this work, we have assumed Coulomb friction in which the frictional force equals the product of coefficient of friction ($\mu$) and the normal force at contact. This frictional force acts in the direction opposing the relative motion between the surfaces of the bodies in contact. The sticking force obtained from common mesh velocity field is given by

$$\boldsymbol{f}_{stick,i}^{g} = -m_i^g \boldsymbol{n}_i^g \times \left[\left(\boldsymbol{v}_i^g - \boldsymbol{v}_i\right)\times\boldsymbol{n}_i^g\right]\!/\Delta t \tag{6.6}$$

However, in the case of slip, the tangential force considering friction is given by

$$\boldsymbol{f}_{slip,i}^{g} = -m_i^g \mu\left[\left(\boldsymbol{v}_i^g - \boldsymbol{v}_i\right)\cdot\boldsymbol{n}_i^g\right]\!\left(\boldsymbol{n}_i^g \times \hat{\boldsymbol{\omega}}\right)\!/\Delta t \; . \tag{6.7}$$

Generalizing Eqns. (6.6) and (6.7), we get

$$\boldsymbol{f}_{fric,i}^{g} = -m_i^g \mu'\left[\left(\boldsymbol{v}_i^g - \boldsymbol{v}_i\right)\cdot\boldsymbol{n}_i^g\right]\!\left(\boldsymbol{n}_i^g \times \hat{\boldsymbol{\omega}}\right)\!/\Delta t \; , \tag{6.8}$$

where $\mu' = \text{minimum}\left(\mu, \dfrac{\left|\left(\boldsymbol{v}_i^g - \boldsymbol{v}_i\right)\times\boldsymbol{n}_i^g\right|}{\left(\boldsymbol{v}_i^g - \boldsymbol{v}_i\right)\cdot\boldsymbol{n}_i^g}\right),$ \hfill (6.9)

and the unit vector $\hat{\boldsymbol{\omega}} = \dfrac{\left(\boldsymbol{v}_i^g - \boldsymbol{v}_i\right)\times\boldsymbol{n}_i^g}{\left|\left(\boldsymbol{v}_i^g - \boldsymbol{v}_i\right)\times\boldsymbol{n}_i^g\right|} \; .$ \hfill (6.10)

So, the net contact force at the node is given by

$$\boldsymbol{f}_{g,i}^{cont} = f_{n,i}^g\boldsymbol{n}_i^g + \boldsymbol{f}_{fric,i}^g \; , \tag{6.11}$$

and is applied for each grain through equation (6.5).

The computational cost for this contact algorithm was found to be linear with the number of grains in the simulation and requires no iteration. This contact algorithm has been applied to simulation of cylindrical sand grains of uniform as well as non-uniform size in 2D case (Bardenhagen and Brackbill, 2001), for irregular sand grains in contact

124

(Sulsky, 2003), and was found to be effective in capturing features such as force chains in mono- or polydispersed grains of sand (Bardenhagen *et al.* 2000, 2001).

6.4 Method for determining normals to the surface for contact algorithm implementation:

The normals to the surface at any point on the surface can be determined by taking the spatial gradient of the known surface geometry at that point. For irregular and unknown surface geometries, the normals to the contact surface can be determined by taking the gradient of the equation for the surface determined by fitting a cubic b-spline to the surface material points. In this work we have focused upon simple geometries. For example, consider the determination of normals for the surface material points of a solid sphere. The equation of a solid sphere is given by

$$(x - x_0)^2 + (y - y_0)^2 + (z - z_0)^2 \leq R^2, \tag{6.12a}$$

and let the surface $S(x, y, z) = (x - x_0)^2 + (y - y_0)^2 + (z - z_0)^2 = R^2$. $\tag{6.12b}$

where $(x_0, y_0, z_0)$ are the co-ordinates of the geometric center.

When the spherical geometry is discretized, the material points near the surface will not form a smooth surface. In this case, we have adopted using a cut-off radius (smaller than the geometric radius) to determine the surface material points. As such, the surface material points determined in this way do not necessarily lie on the geometric surface defined by equation (6.12b). For such material points, a new surface $S'$ is defined with radius equal to the radial distance of this surface material point to the geometric center.

$$S'(x, y, z) = (x - x_0)^2 + (y - y_0)^2 + (z - z_0)^2 = (R')^2, \tag{6.13a}$$

where $(R')^2 = (x_p - x_0)^2 + (y_p - y_0)^2 + (z_p - z_0)^2$. $\tag{6.13b}$

and $(x_p, y_p, z_p)$ are the co-ordinates of the material point for which the normal vector needs to be found.

The normal vector ($n$) to the surface at any surface point is then given by evaluating the gradient of surface $S'$ at that material point location. Additionally, the tangents to the surface ($S'$) are determined at that point (corresponding to the surface material point). Numerous ways exist to determine tangents. One of which is to determine the equation for the tangent plane and extracting a vector ($t_1$) which would be tangent to the surface. A second tangent ($t_2$) can then be found using cross-product of unitized vectors $\hat{t}_1$ and $\hat{n}$. Thus we have defined two tangents at the surface material point, which will be tracked as the material points convect over the background grid during MPM simulation. Thus, with known velocity gradients the tangents can be updated during successive simulation steps as

$$\hat{t}^{\ new} = (\delta + \nabla u)\,\hat{t}, \tag{6.14}$$

where $\nabla u$ are the displacement gradients for that simulation step, $\delta$ is the Kronecker delta function, $\hat{t}_j^{new}$ is the updated tangent vector for the next time-step.

Further, the updated normal for the deformed/updated configuration of material points can then be computed using the cross-product of updated tangent vectors. The normals calculated at the material points in this manner can be used for the next timestep by projecting them on to the nodes of the background grid with the help of shape functions.

6.5 Numerical simulation results: Verification using simulation of a sphere rolling on an inclined plane

The contact algorithm presented in Section 6.3 and the procedure proposed to determine normals presented in Section 6.4 was implemented in 3D MPM for two geometries considered here, namely, a sphere and a cuboid. For verification of the implementation, a 3D rolling simulation is considered.
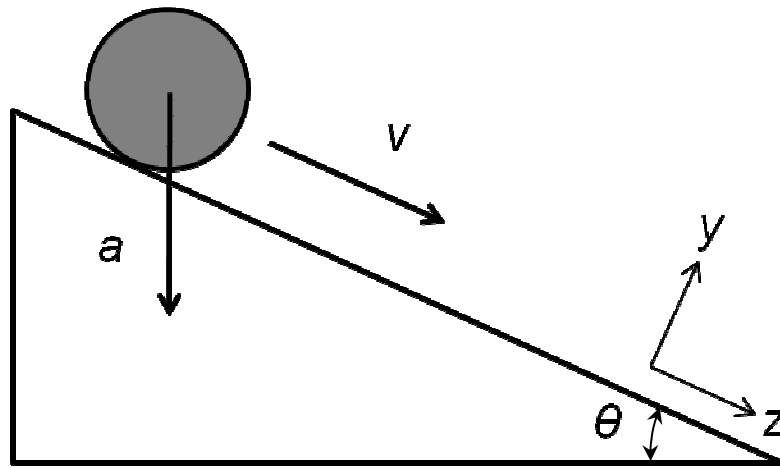


Figure 6.1: Schematic showing rolling of a sphere on an inclined plane.

Figure 6.1 shows a schematic for simulation of sphere rolling on an inclined which is at an angle $\theta$ with the horizontal. An acceleration $a$ is acting on the sphere which acts as a body force on the material points resulting from discretization of the geometry. For modeling this example, the boundary of the computational mesh is aligned with the inclined plane. The 3D contact algorithm in this work considers friction between the interacting surfaces of the sphere and the plane.

Theoretical solution for a rigid sphere rolling on a rigid plane is used for verification of simulation results. Depending on the value of the coefficient of friction and the angle

of inclination for the plane, the sphere will either purely roll on the surface or it will slip. For a rigid sphere rolling on a rigid surface, the center-of-mass position as a function of time is given as

$$z_{cm}(t) = \begin{cases} z_0 + wt + \dfrac{1}{2}at^2 \sin\theta, & \text{for } tan\,\theta < 3\mu \text{ (pure rolling)} \\ z_0 + wt + \dfrac{1}{2}at^2(\sin\theta - \mu\cos\theta), & \text{for } tan\,\theta \geq 3\mu \text{ (slip)} \end{cases}$$

(6.15)

where $w$ is the initial velocity along z-axis at time, $t = 0$ s, and $z_0$ is the initial z-component of the center-of-mass position.

A sphere of diameter 10 mm is used in the simulation of rolling, and an acceleration of magnitude $a = 9800$ m/s. It should be noted that acceleration used are on the higher side, so that the total computational time required for the entire simulation is short, in this case ~ 20 minutes. The background grid uses 8-node cubic elements with length of their sides as 0.5 mm, and one material point is used to represent the volume in each cell. Figure 6.2 shows the discretized model used in the simulations. In order to allow for large time-steps using an explicit code, material properties chosen are for a soft material. Both the sphere and the plane are modeled using material model for hypoelastic bodies. It is assumed that the sphere has bulk modulus of 6 MPa, a shear modulus of 3 MPa, and a density of 1000 kg/m$^3$ (roughly approximating to those of natural rubber) (Bardenhagen *et al.*, 2004). The body force is applied on the material points as

$$\boldsymbol{f}^b = \rho\boldsymbol{a}.$$

(6.16)
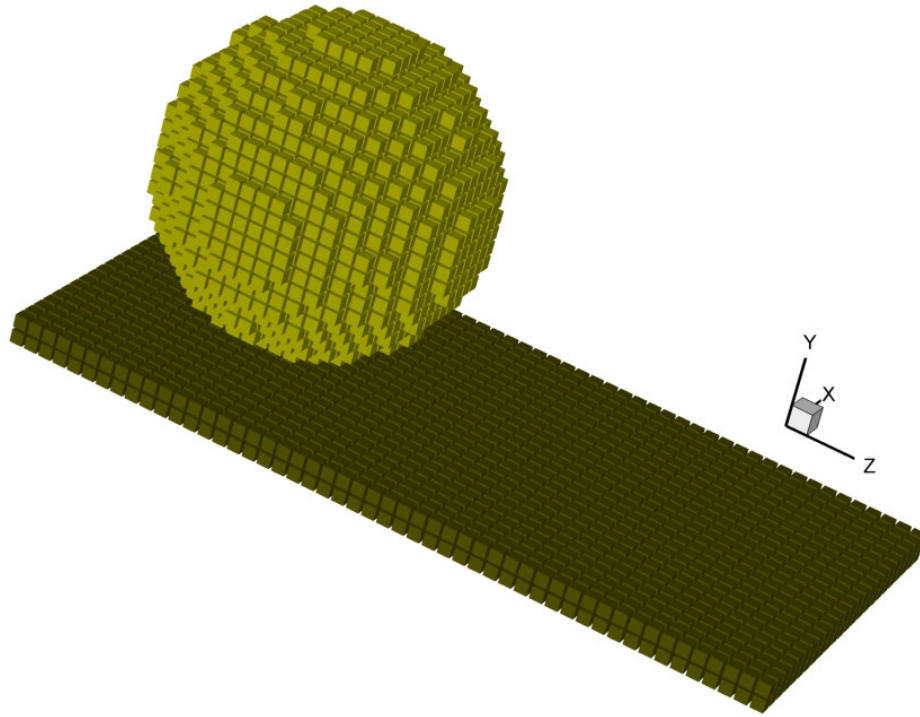
Figure 6.2: Discretized MPM model of rolling simulation.

A parametric study is carried out with respect to varying the inclination of the plane and changing the coefficient of friction. For the first part of study, the coefficient of friction is held constant of $\mu = 3$, and the angle of inclination used are $\pi/6$, $\pi/4$, and $\pi/3$ radians. Fig. 6.3 shows the variation of normalized center-of-mass positions with normalized time, obtained for three different angles of inclination. In all the cases, the simulations consist of pure rolling of the sphere over the inclined plane. The figure also shows the corresponding analytical solutions for rigid bodies applicable for the stick or pure rolling case. The next parametric study involved keeping the angle of inclination fixed to $\theta = \pi/4$ radians and changing the coefficient of friction from 0.1 to 3.

Fig. 6.4 shows the normalized center-of-mass positions at different times (normalized), obtained for three different coefficients of friction 0.1, 1, and 3. The

simulation results show pure rolling of the sphere over the inclined place for the case of $\mu$ = 1 and 3. The corresponding analytical solutions for the center-of-mass positions applicable for the pure rolling case are used to verify the simulation results. The simulation results for $\mu$ = 0.1 agree with the theoretical predictions indicating slip of the sphere over the inclined plane. In this case, the analytical solution given by Eqn. (6.15) for the slip case is used to compare with the simulation results. Overall, the computed solutions for the deformable sphere compares well with the rigid-sphere solutions. The difference observed can be attributed to the use of deformable bodies in simulations.
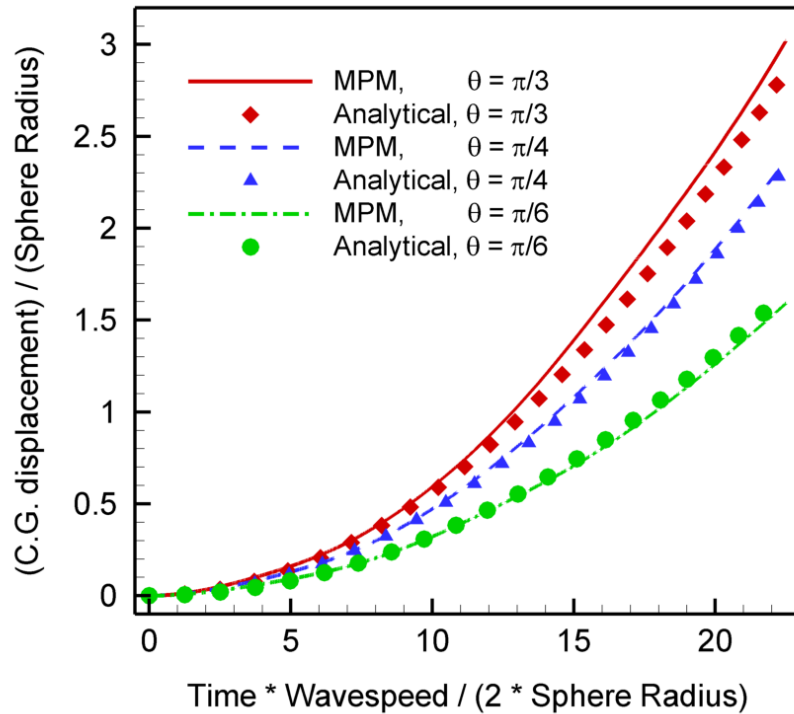


Figure 6.3: Discretized MPM model of rolling simulation.
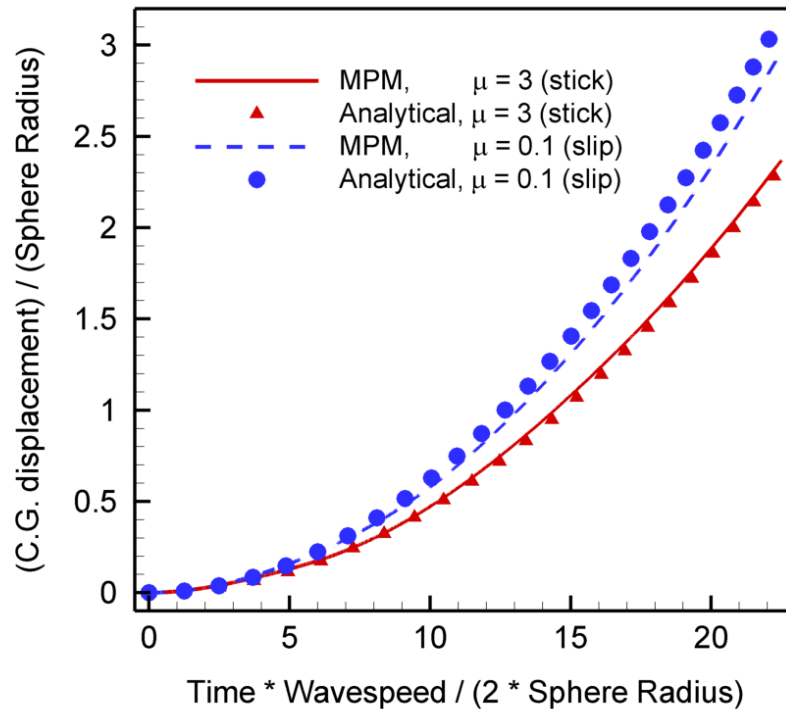
Figure 6.4: Discretized MPM model of rolling simulation.

6.6 Conclusions

A contact algorithm was implemented in 3D MPM based on multimesh technique. The contact condition based on center-of-mass velocity field can effectively detect contact between surfaces. A new methodology was developed to update the normals for the surface material points in contact, which conserved the original surface geometry before MPM discretization. This method does not require time-consuming neighbor search algorithm in order to find the normals for successive MPM simulation steps and hence is computationally efficient. The algorithm was demonstrated and verified using a

131

rolling simulation example, for which the deformable body solution compared favorably well with the rigid body solutions. Contact algorithm, considering friction and 3D µ-CT information of sand grains, can be used for simulation of granular materials in compression.

CHAPTER VII

SUMMARY OF CONCLUSIONS AND FUTURE WORK

7.1 Summary of conclusions

Material Point method (MPM) can effectively simulate many dynamic problems in solid mechanics, which otherwise would be challenging using purely Lagrangian or Eulerian based methods. Application of MPM has been demonstrated through various problems involving dynamic mode-II crack propagation, simulations of Rohacell foam in compression considering its real microstructure, and its potential for simulation of granular media with implementation of highly efficient contact algorithm for frictional slip considerations.

Cohesive zone model was implemented in MPM so that it can handle dynamic crack propagation. The particle nature of the material makes it relatively easier (compared with FEM) to incorporate cohesive segments to model the crack surfaces independent of the background mesh. For the MPM simulations of crack propagation in the intersonic regime, the dependence of shear shock angle on the crack-tip speed conforms to the theoretical prediction. A transition crack-tip velocity of 1.66 $c_S$ m/s was observed, which remained more or less constant for cohesive strengths of 4, 12, 24, and 35 MPa (in both shear and normal directions) corresponding to the impact speeds of 2.25, 5.7, 9.5, and 12.5 m/s, respectively. The Burridge-Andrews transitions mechanism, which relates to

transitions of crack-tip speed from sub-Rayleigh to intersonic regime, was observed over a range of impact speeds.

Further, MPM was demonstrated as an effective method for the simulation of foam microstructures with ease in discretization. MPM simulations of Rohacell foam under compression were able to capture features observed during *in-situ* experiments using μ-CT. Cohesive zone model along with foam microstructures can be used in MPM to simulate interfacial failure of composite sandwich structures.

Nanoindentation was shown to be an effective technique for the characterization of mechanical properties of sand grains at the granular level and skeletal properties of foam microstructure. Properties determined using nanoindentation can be used as input for MPM simulations of granular materials. An improved contact algorithm was implemented in MPM. This algorithm forbids interpenetration of surfaces but allows separation, sliding and rolling with friction. No separate contact detection step is required and the computational cost scales linearly with the number of grains. Material properties determined from nanoindentation and geometry information obtained from μ-CT will enable MPM simulations of granular materials.

## 7.2 Future work

### 7.2.1 Crack surface contact and dynamic friction model in the wake of the crack-tip

With respect to the dynamic mode-II crack propagation simulation results (from a comparison between numerical and experimental photoelastic patterns in Fig. 3.16) we concluded that the crack surface contact behind the cohesive zone can affect the stress field in the wake of the crack-tip. Thus, as part of future work, contact and friction

between the crack surfaces in the wake of the crack-tip can be considered. The classical Amontons-Coulomb law fails to consider the length scale and rate dependency. Rate and state dependent relation (Prakash and Clifton, 1993; Prakash, 1998) needs to be implemented in MPM to simulate friction in the wake of the crack-tip and as outlined in the following:

Following Chapter-2, the friction at the interface can be considered through traction boundary conditions as

$$\boldsymbol{\tau}_{fric} = \overline{\boldsymbol{\tau}}_{fric} \text{ on } \partial\Omega_{fric}, \tag{7.1}$$

where $\partial\Omega_{coh} \cap \partial\Omega_{fric} = \varnothing$, $\partial\Omega_{fric} \cap \partial\Omega_{\tau} = \varnothing$ and $\partial\Omega = \partial\Omega_u \cup \partial\Omega_{\tau} \cup \partial\Omega_{coh} \cup \partial\Omega_{fric}$.

Applying chain rule and divergence theorem to the variational form of conservation of momentum equation (incorporating traction vector for friction considerations at the boundary, $\partial\Omega_{fric}$), we get

$$\int_{\Omega} \rho \boldsymbol{a} \cdot \delta v d\boldsymbol{x} + \int_{\Omega} \boldsymbol{\sigma} : \nabla \delta v d\boldsymbol{x} = \int_{\Omega} \boldsymbol{b} \cdot \delta v d\boldsymbol{x} + \int_{\partial\Omega_{\tau}} \overline{\boldsymbol{\tau}} \cdot \delta v dS + \int_{\partial\Omega_{coh}} \overline{\boldsymbol{\tau}}_{coh} \cdot \delta v dS + \int_{\partial\Omega_{fric}} \overline{\boldsymbol{\tau}}_{fric} \cdot \delta v dS + \int_{\partial\Omega_u} \overline{\boldsymbol{\tau}}_u \cdot \delta v dS \tag{7.2}$$

Here, $\boldsymbol{\tau}_u$ is the resultant traction due to the displacement boundary condition on $\partial\Omega_u$, and $\overline{\boldsymbol{\tau}}$ is the external traction vector and $\overline{\boldsymbol{\tau}}_{coh}$ and $\overline{\boldsymbol{\tau}}_{fric}$ are the cohesive and frictional traction, respectively, at the interface, $\partial\Omega_{coh}$ and $\partial\Omega_{fric}$.

The momentum conservation equation is modified as

$$\sum_p \int_{\Omega\cap\Omega_p} \frac{\dot{\mathbf{p}}_p \chi_p}{V_p} \cdot \delta\mathbf{v} d\mathbf{x} + \sum_p \int_{\Omega\cap\Omega_p} \boldsymbol{\sigma}_p \chi_p : \delta\mathbf{v} d\mathbf{x} = \sum_p \int_{\Omega\cap\Omega_p} \frac{m_p \chi_p}{V_p} \mathbf{b} \cdot \delta\mathbf{v} d\mathbf{x} + \sum_p \int_{\partial\Omega_{\tau}\cap\Omega_p} \overline{\boldsymbol{\tau}} \cdot \delta\mathbf{v} dS + \sum_p \int_{\partial\Omega_{coh}\cap\Omega_p} \overline{\boldsymbol{\tau}}_{coh} \cdot \delta\mathbf{v} dS + \sum_p \int_{\partial\Omega_{fric}\cap\Omega_p} \overline{\boldsymbol{\tau}}_{fric} \cdot \delta\mathbf{v} dS + \sum_p \int_{\partial\Omega_u\cap\Omega_p} \overline{\boldsymbol{\tau}}_u \cdot \delta\mathbf{v} dS \tag{7.3}$$

Finally, the momentum conservation, can eventually be written for each node $i$ as

$$\dot{\mathbf{p}}_i = \mathbf{f}_i^{\text{int}} + \mathbf{f}_i^{b} + \mathbf{f}_i^{\tau} + \mathbf{f}_i^{coh} + \mathbf{f}_i^{fric}. \tag{7.4}$$

and the frictional force vector $\mathbf{f}_i^{fric} = \sum_p \int_{\partial \Omega_{fric} \cap \Omega_p} \overline{\boldsymbol{\tau}}_{fric} S_i(\mathbf{x}) dS$. \hfill (7.5)

with other parameters remaining the same as given in Chapter-2.

Coker *et al.* (2005) summarizes the rate and state dependent friction law proposed by Prakash and Clifton (1993), and Prakash (1998). They also describe the explicit time integration procedure to calculate the frictional traction vector for each integration point, which they implemented in the finite element method. In MPM, this procedure will remain the same and can be used to calculate the frictional traction on the material points forming the boundary in the wake of the crack-tip.

In order to avoid interpenetration of crack surfaces behind the crack tip, the multimesh contact algorithm present in Chapter VI can be used. The normals can be determined based on the positions of the cohesive segments and the contact forces, considering of normal and frictional forces can be applied at the cohesive nodes in the wake of the crack tip.

### 7.2.2 MPM simulation of sand under compression

Since MPM does not use body-fixed mesh for computation, it offers an advantage in the simulation of dynamic problems in solid mechanics over finite element and meshless methods. MPM can handle relatively easily, the modeling of realistic microstructures and particulate media at meso level. Bardenhagen *et al.* (2000) demonstrated 2D MPM for simulation of particulate matter. MPM offers advantages over discrete element method. MPM considers size, shape, and material properties of each

individual sand grain at meso level to model the realistic structures instead of modeling them as rigid spheres, as in Discrete Element Method (DEM). MPM has three major advantages in sand simulations: (1) capability to handle large deformations; (2) ability to model real microstructures; and (3) ability to handle extensive contact. Additionally, implementation of various history-dependent constitutive models (e.g. elastic-plastic, viscoelastic, single crystal plasticity) is straightforward. MPM can consider the phenomenological models for friction and sand grains to effectively model the behavior of sand. For simulations at the granular level, the mechanical properties of sand grains determined from nanoindentations can be used.

Fig. 7.1 shows the microstructure of sand in a cylindrical container. Material points are assigned at locations within the material to generate a MPM model, as shown in Fig. 7.2. Experimentally characterized material properties for individual sand grains can be assigned.
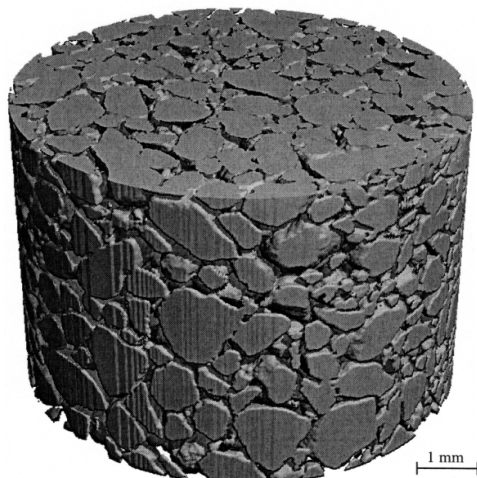


Figure 7.1: μ-CT of sand sample
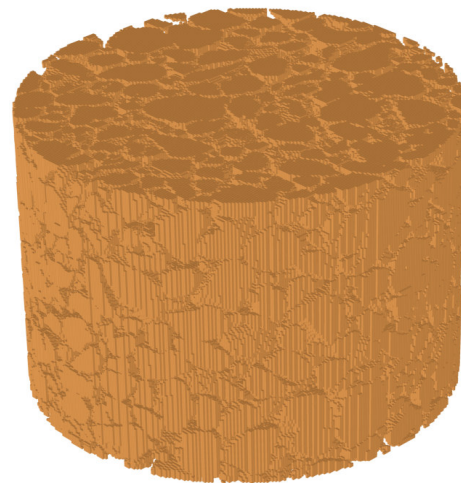
Figure 7.2: A discretized MPM model

Modulus values can be assigned for each sand grain based on their grayscale value (indicating the density of sand, which is output from the µ-CT scanning) following the same distribution as observed in experiments. This is under the assumption that the sand grains being modeled are isotropic. To consider the inhomogeneity of the sand grain, the distribution of stress-strain properties obtained from nanoindentation can be used. Further, the model shown in Figure 7.2 and similar models obtained considering variation in grain size and sand type can be used in MPM simulations using parallel computing.

REFERENCES

ABAQUS Documentation Version 6.4

Abraham, F.F. and Gao, H., 2000. How fast can cracks propagate? *Physical Review Letters* 84(40), 3113-3116

Andrews, D.J., 1976. Rupture velocity of plane strain shear cracks. *Journal Geophysics Research* 81, 5679-5687.

Arthur, J.R.F. and Menzies, B.K., 1972. Inherent anisotropy in a sand. *Geotechnique* 22(1), 115–128.

Bardenhagen, S.G., Brackbill, J.U. and Sulsky, D., 2000. The material point method for granular materials. *Computer Methods in Applied Mechanics and Engineering* 187, 529-541.

Bardenhagen, S.G., Guilkey, J.E., Roessig, K.M., Brackbill, J.U., Witzel, W.M. and Foster, J.C., 2001, An improved contact algorithm for the Material Point Method and application to stress propagation in granular material. *Computer Modeling in Engineering and Sciences* 2, 509-522

Bardenhagen, S.G. and Kober, E.M., 2000. The generalized interpolation material point method. *Computer Modeling in Engineering and Sciences* 1(1), 11-29.

Bardenhagen, S.G. and Kober, E.M., 2004. The generalized interpolation material point method. *Computer Modeling in Engineering and Sciences* 5(6), 477-496.

Bardenhagen, S. G., Brydon, A. G. and Guilkey, J. E., 2005. Insights into the physics of foam densification via numerical simulation," *Journal of the Mechanics and Physics of Solids* 53, 597-617.

Barenblatt, G.I., 1962. The mathematical theory of equilibrium cracks in brittle fracture. *Advances in Applied Mechanics* 7, 55-129.

Belytschko, T., Chen, H., Xu, J. and Zi, G., 2003. Dynamic crack propagation based on loss of hyperbolicity and a new discontinuous enrichment. *International Journal for Numerical Methods in Engineering* 58, 1873-1905.

Bhattacharya, A.K. and Nix, W.D., 1988. Finite element simulation of indentation experiments. *International Journal of Solids and Structures* 24(9), 881-891

Bhattacharya, A.K. and Nix, W.D., 1991. Finite element analysis of cone indentation. *International Journal of Solids and Structures* 27(8), 1047-1058

Borst, R. de, Remmers, J.J.C. and Needleman, A., 2006. Mesh-independent discrete numerical representations of cohesive-zone models. *Engineering Fracture Mechanics* 73, 160-177.

Brackbill, J. U., Kothe, D. B. and Ruppel, H. M., 1988. FLIP: A low-dissipation particle-in-cell method for fluid flow. *Computational Physics Communications* 48, 25-38.

Brackbill, J.U. and Ruppel, H.M., 1986. FLIP: A method for adaptively zoned, particle-in-cell calculations in two dimensions. *Journal of Computational Physics* 65, 314-343.

Broberg, K.B., 1989. The near-tip field at high crack velocities. *International Journal of Fracture* 39, 1-13.

Brydon, A.D., Bardenhagen, S.G., Miller, E.A. and Seidler, G.T., 2005. Simulation of the densification of real open-celled foam microstructures. *Journal of the Mechanics and Physics of Solids* 53, 2638-2660.

Burridge, R., 1973. Admissible speeds for plane strain shear cracks with friction but lacking cohesion. *Geophysical Journal of the Royal Astronomical Society* 35, 439-455.

Camacho, G.T. and Ortiz, M., 1996. Computational modeling of impact damage in brittle materials. *International Journal of Solids Structures* 33, 2899-2938.

Cheng, L., Xia, X., Yu, W., Scriven, L.E. and Gerberich, W.W., 2000. Flat-punch indentation of viscoelastic material. *Journal of Polymer Science, Part B: Polymer Physics* 38, 10-22.

Cirak, F., Ortiz, M. and Pandolfi, A., 2004. A cohesive approach to thin-shell fracture and fragmentation. XXI International Congress of Theoretical and Applied Mechanics, Warsaw, Poland.

Coker, D., Rosakis, A. J. and Needleman, A., 2003. Dynamic crack growth along a polymer composite—Homalite interface. *Journal of the Mechanics and Physics of Solids* 51, 425-460.

Cummins, S. J. and Brackbill, J. U., 2002. An Implicit Particle-in-Cell Method for Granular Materials. *Journal of Computational Physics* 180, 506.

Dao, M., Chollacoop, N., Van Vliet, K.J., Venkatesh, T.A. and Suresh, S., 2001. Computational modeling of the forward and reverse problems in instrumented sharp indentation. *Acta Materialia* 49, 3899-3918.

Daphalapurkar, N., Lu, H., Coker, D., Komanduri, R., 2007. Simulation of Dynamic crack growth using the generalized interpolation material point (GIMP) method. *International Journal of Fracture* 143, 79-102.

De Carlo F., Xiao, X. and Tieman, B., 2006. X-Ray Tomography System, Automation and Remote Access at Beamline 2-BM of the Advanced Photon Source. *Developments in X-Ray Tomography V*, edited by Ulrich Bonse, Proc. of SPIE Vol. 6318, 63180K, ·1605-7422.

Desrues, J., Lanier, J. and Stutz, P., 1985. Localization of the deformation in tests on sand sample. *Engineering Fracture Mechanics* 21(4), 909–921.

Doerner, M.F. and Nix, W.D., 1986. A method for interpreting the data from depth-sensing indentation instruments. *Journal Materials Research* 1, 601-613.

Dugdale, D.S., 1960. Yielding of steel sheets containing slits. *Journal of the Mechanics and Physics of Solids* 8, 100-104.

Falk, M.L., Needleman, A. and Rice, J.R., 2001. A critical evaluation of cohesive zone models of dynamic fracture. *Journal de Physique IV France* 11, 543-550.

Fay, J., Puria, S., Decraemer, W.F. and Steele, C., 2005. Three approaches for estimating the elastic modulus of the tympanic membrane. *Journal of Biomechanics* 38, 1807-1815.

Fischer-Cripps, A.C., 2002. Nanoindentation. Springer-Verlag, Berlin, Germany.

Fivel, M.C., Robertson, C.F., Canova, G.R. and Boulanger, L., 1998. Three-dimensional modeling of indent-induced plastic zone at a mesoscale. *Acta Materialia* 46(17), 6783-6194.

Freund, L.B., 1998. Dynamic fracture mechanics. Cambridge University Press, Cambridge.

Gao, H., Huang, Y. and Abraham, F.F., 2001. Continuum and atomistic studies of intersonic crack propagation. *Journal of the Mechanics and Physics of Solids* 49, 2113-2132.

Gao, H. and Ji, B., 2003. Modeling fracture in nanomaterials via a virtual internal bond method. *Engineering Fracture Mechanics* 70, 1777-1791.

Gao, H. and Klein, P., 1998. Numerical simulation of crack growth in an isotropic solid with randomized internal cohesive bonds. *Journal of the Mechanics and Physics of Solids* 46 (2), 187-218.

Geng J.,Howell E., Behringer R., Reydellet G., Vanel L., Clement E. and Luding S., 2001. Footprints in sand: The response of a granular material to local perturbations. *Physical Review Letters* 87(3), 35506

Gibson, L. J. and Ashby, M. F., 1997. Cellular Solids: Structure and Properties, 2nd Ed., Cambridge University Press.

Goldenberg, C. and Goldhirsch, I., 2005. Friction enhances elasticity in granular solids," *Nature* 435, 188-191

Guilkey, J.E. and Weiss, J.A., 2003. Implicit time integration for the material point method: Quantitative and algorithmic comparisons with the finite element method. *International Journal for Numerical Methods in Engineering* 57, 1323-1338.

Guo, G., Yang, W., Huang, Y. and Rosakis, A.J., 2003. Sudden deceleration or acceleration of an intersonic shear crack. *Journal of the Mechanics and Physics of Solids* 51, 311-331.

Haard, T. M., Gervais, G., Nomura, R. and Halperin, E.P, 2000. The pathlength distribution of simulated aerogels. *Physica* B 284-288, 289-290.

Hao, S., Liu, W.K., Klein, P.A. and Rosakis, A.J., 2004. Modeling and simulation of intersonic crack growth. *International Journal of Solids and Structures* 41, 1773-1799.

Harding, D.S., 1995. Cracking during nanoindentation and its use in the measurement of fracture toughness. *Materials Research Society symposia proceedings* 356(5), 663-668.

Harlow, F. H., 1964. The particle-in-cell computing method for fluid dynamics. *Methods for Computational Physics* 3, 319-343.

Hasmy, A., Foret, M., Pelous, J. and Jullien, R., 1993. Small-angle neutron-scattering investigation of short-range correlations in fractal aerogels: Simulations and experiments. *Physical Review* B 48(13), 9345-9353.

Haythornthwaite, R., 1997. Simple shear in granular media. *Applied Mechanics Reviews* 50(11), 81-86

Hill, R., Lee, E.H. and Tupper, S.J., 1947. The theory of combined plastic and elastic Deformation with Particular Reference to a Thick Tube under Internal Pressure. *Proceedings of the Royal Society of London* A188, 278-303.

Hornung, R.D. and Kohn, S.R., 2002. Managing application complexity in the SAMRAI object-oriented framework. *Concurrency and Computation: Practice and Experience* 14, 347-368.

Hu, W. and Chen, Z, 2006. Model-based simulation of the synergistic effects of blast and fragmentation on a concrete wall using MPM. *International Journal of Impact Engineering* 32, 2066-2096.

Huang, Y. and Gao, H., 2001. Intersonic crack propagation – part I: the fundamental solution. *Journal of Applied Mechanics* 68, 169-175.

Huang, G. and Lu, H., 2006. Measurement of Young's relaxation modulus using Nanoindentation. *Mechanics of Time-Dependent Materials* 10, 229-243

Huang, G. and Lu, H., 2007. Measurements of Two Independent Viscoelastic Functions by Nanoindentation. *Experimental Mechanics* 47, 87-98.

Huang, G., Wang, B. and Lu, H., 2004. Measurements of Viscoelastic Functions in Frequency-Domain by Nanoindentation. *Mechanics of Time-Dependent Materials*, 8, 345-364.

Huang, G., Wang, B. and Lu, H., 2004. Measurements of viscoelastic functions in frequency-domain by nanoindentation. *Mechanics of Time-Dependent Materials* 8, 345-364.

Ishlinskii, A.J., 1944. The axisymmetrical problem in plasticity and the Brinell test. *Journal of Applied Mathematics and Mechanics* 8, 201-224.

Johnson, K.L., 1970. The correlation of indentation experiments. *Journal of Mechanics and Physics of Solids* 18(2), 115-126.

Katti, A., Nilesh, S., Samit, R., Lu, H., Fabrizio, E.F., Dass, A., Capadona, L.A. and Leventis, N., 2006. Chemical, physical and mechanical characterization of isocyanate cross-linked amine-modified silica aerogels. *Chemistry of Materials* 18, 285-296.

Klein, P.A., Foulk, J.W., Chen, E.P., Wimmer, S.A. and Gao, H.J., 2001. Physics-based modeling of brittle fracture: cohesive formulations and the applications of meshfree methods. *Theoretical and Applied Fracture Mechanics* 37, 99-166.

Knapp, J.A., Follstaedt, D.M., Myers, S.M., Barbour, J.C., Friedmann, T.A., Ager, J.W., Monteiro, O.R. and Brown, I.G., 1998. Finite-element modeling of nanoindentation for evaluating mechanical properties of MEMS materials. *Surface Coating Technology* 103–104, 268-75.

Knauss, W.G., 1993. Time dependent fracture and cohesive zones. *Transactions of the American Society of Mechanical Engineers* 115, 262-267.

Lade, P.V. and Duncan, J.M., 1973. Cubical triaxial tests on cohesionless soil. *Journal of the Soil Mechanics and Foundations Division* 99(10), 793-812

Lade, P.V. and Prabucki, M.J., 1995. Softening and preshearing effects in sand. *Soils and Foundation* 35(4), 93-104

Lee, E.H. and Radok, J.R.M., 1960. The contact problem for viscoelastic bodies. *Journal of Applied Mechanics* 27, 438-444.

Leventis, N., Mulik, S., Wang, X., Daas, A., Leventis, C.S. and Lu, H., 2007. Stresses at the Interface of Micro with Nano. *Journal of the American Chemical Society* 129, 10660-10661.

Leventis, N., Mulik, S., Wang, X., Dass, A., Patil, V.U., Leventis, C., S., Lu, H., Churu, G. and Capecelatro, A., 2008. Conformal Polymer Nano-Encapsulation of Ordered Mesoporous Silica Monoliths for Improved Mechanical Properties. *Journal of Non-Crystalline Solids* 354, 632-644.

Li, X. and Bhushan, B., 2002. A Review of Nanoindentation Continuous Stiffness Measurement Technique and Its Applications. *Materials Characterization* 48, 11─36.

Liao, J.J., Yang, M.-T. and Hsieh, H.-Y., 1996. Direct tensile behavior of a transversely isotropic rock. *International Journal of Rock Mechanics and Mining Sciences* 34(5), pp. 837-849

Lichinchi, M., Lenardi, C., Haupt, J. and Vitali, R., 1998. Simulation of Berkovich nanoindentation experiments on thin films using finite element method. *Thin Solid Films* 1-2, 240-248

Liu, Y., Wang, B., Yoshino, M., Roy, S., Lu, H. and Komanduri, R., 2005. Combined numerical simulation and nanoindentation for determining mechanical properties of single crystal copper at mesoscale. *Journal of Mechanics and Physics of Solids* 53, 2718─2741

Lu, H., Daphalapurkar, N.P., Wang, B., Roy, S. and Komanduri, R., 2006. Multiscale simulation from atomistic to continuum – Coupling molecular dynamics (MD) with the material point method (MPM). *Philosophical magazine*, v86-n20, 2971-2994.

Lu, H., Wang, B., Ma, J., Huang, G. and Viswanathan, H., 2003. Measurement of creep compliance of solid polymers by nanoindentation. *Mechanics of Time-Dependent Materials* 7, 189-207.

Lu, H., Zhang, X. and Knauss, W. G., 1997. Uniaxial, shear and Poisson relaxation and their conversion to bulk relaxation: Studies on Poly(Methyl Methacrylate). *Polymer Engineering and Science* 37(6), 1053-1064

Luo, H., Lu, H. and Leventis, N., "The Compressive Behavior of Isocyanate-Crosslinked Silica Aerogel at High Strain Rates," *Mechanics of Time-Dependent Materials* **10**, 83-111 (2006).

Oda, M. Konishi, J. and Nemat-Nasser, S., 1980. Some experimentally based fundamental results on the mechanical behavior of granular materials. *Geotechnique*, 30, 479-495

Oda, M. and Konishi, J., 1974. Microscopic deformation mechanism of granular material in simple shear. *Soils and Foundation* 14(4), 25-38

Oliver, W.C., Hutchings, R. and Pethica, J.B., 1986. Measurement of hardness at indentation displacements as low as 20 nanometers. Microindentation Techniques in Materials Science and Engineering, ASTM STP 889, American Society for Testing and Materials. Philadelphia, 90-108.

Oliver, W.C. and Pharr, G.M., 1992. An improved technique for determining hardness and elastic modulus using load and displacement sensing indentation experiments. *Journal of Materials Research* 7 (6), 1564-1583.

Ma, J., Lu, H. and Komanduri, R., 2006a. Structured Mesh Refinement in Generalized Interpolation Material Point (GIMP) Method for Simulation of Dynamic Problems. *Computer Modeling in Engineering and Sciences* 12(3), 213-227.

Ma, J., Lu, H., Wang, B., Roy, S., Hornung, R., Wissink, A. and Komanduri, R., 2005. Multiscale simulations using generalized interpolation material point (MPM) method and SAMRAI parallel processing. *Computer Modeling in Engineering & Sciences* 8 (2), 135-152.

Ma, J., Lu, H., Wang, B., Hornung, R., Wissink, A. and Komanduri, R., 2006. Multiscale simulations using generalized interpolation material point (GIMP) method and molecular dynamics (MD). *Computer Modeling in Engineering and Sciences* 14(2), 101-118.

Moes, N. and Belytschko, T., 2002. Extended finite element method for cohesive crack growth. *Engineering Fracture Mechanics* 69, 813-833.

Morales-Florez, V. and De La Rosa-Fox, N., 2005. The Cluster model: A simulation of the aerogel structure as a hierarchically-ordered arrangement of randomly packed spheres. *Journal of Sol-Gel Technology* 35, 203-210.

Morrissey, J.W. and Rice, J.R., 1998. Crack front waves. *Journal of the Mechanics and Physics of Solids* 46 (3), 467-487.

Nairn, J.A., 2003. Material point method calculations with explicit cracks. *Computer Modeling in Engineering and Sciences* 4(6), 649-663.

Nairn, J. A., 2006. Numerical simulations of Transverse Compression and Densification in Wood. *Wood and Fiber Science* 38(4), 576-591.

Nairn, J.A. and Guo Y.J., 2005. Material point method calculations with explicit cracks, fracture parameters and crack propagation. 11th International Conference on Fracture, in press, Turin, Italy.

Needleman, A., 1987. A continuum model for void nucleation by inclusion debonding. *ASME Journal of Applied Mechanics* 54, 525-531.

Needleman, A., 1990. An analysis of tensile decohesion along an interface. *Journal of the Mechanics and Physics of Solids* 38 (3), 289-324.

Needleman, A., 1999. An analysis of intersonic crack growth under shear loading. *Journal of Applied Mechanics* 66, 847-857.

Nguyen, T.D., Govindjee, S., Klein, P.A. and Gao, H., 2004. A rate dependent cohesive continuum model for the study of crack dynamics. *Computer Methods in Applied Mechanics and Engineering* 193, 3239-3265.

Oliver, W.C., Hutchings, R. and Pethica, J.B., 1986. Measurement of hardness at indentation displacements as low as 20 nanometers. *Microindentation Techniques in Materials Science and Engineering* ASTM STP 889, American Society for Testing and Materials. *Philadelphia*, 90-108.

Parker S.G., 2002. A component based architecture for parallel multi-physics PDE simulation. International conference on computational science (ICCS2002) Workshop on PDE software

Pethica, J.B., Hutchings, R. and Oliver, W.C., 1983. Hardness measurement at penetration displacements as small as 20 nm. *Philosophical Magazine* A 48, 593-606.

Pethica J. B. and Oliver, W.C., 1987. Tip surface interactions in STM and AFM. *Physica Scripta* T19, A:61-66.

Pharr, G.M., Harding, D.S. and Oliver, W.C., 1993. Measurement of fracture toughness in thin films and small volumes using nanoindentation method," Mechanical properties and deformation behavior of materials having ultra-fine microstructures, edited by M. Nastasi, D. M. Parkin and H. Gleiter, Kluwer Academic Publishers, 449-461.

Pohl, P.I., Faulon, J.-L. and Smith, D.M., 1995. Molecular dynamics computer simulations of silica aerogels. *Journal of Non-Crystalline Solids* 186, 349-355.

Poorooshasb, H.B., Holubec, I. and Sherbourne, A.N., 1966. Yielding and flow of sand in triaxial compression Part I. *Canadian Geotechnical Journal* 3(4), 179-190.

Prakash, V., 1998. Frictional response of sliding interfaces subjected to time varying

normal pressures. *Journal of Tribology* 120, 97-102.

Prakash, V. and Clifton, R.J., 1993. Pressure-shear plate impact measurement of dynamic friction for high speed machinig applications. *Proceedings of the Seventh International Congress on Experimental Mechanics*. Society of Experimental Mechanics, Bethel, CT, 556-564.

Prandtl, L., 1920. Ueber die Haerte plasticher Koerper. *Goettinger. Nachr, Math.-Phys. KI.*, 74-85

Ravi-Chandar, K. and Knauss, W.G., 1984. An experimental investigation into dynamics fracture: II. Microstructural aspects. *International Journal of Fracture* 26, 65-80.

Ravi-Chandar, K. and Knauss, W.G., 1984. An experimental investigation into dynamics fracture: IV. On the interaction of stress waves with propagating cracks. *International Journal of Fracture* 26, 189-200.

Rosakis, A.J., 2002. Intersonic shear cracks and fault ruptures. *Advances in Physics* 51 (4), 1189-1257.

Rosakis, A.J., Samudrala, O., Coker, D., 1999. Cracks faster than the shear wave speed. *Science* 284, 1337-1340.

Samudrala, O., Huang, Y. and Rosakis, A.J., 2002. Subsonic and intersonic mode II crack propagation with a rate-dependent cohesive zone. *Journal of the Mechanics and Physics of Solids* 50, 1231-1268.

Shield, R.T., 1955. Plastic flow of metals under conditions of axial symmetry. *Proceedings of the Royal Society of London* A233, 267-287

Sulsky, D., Zhou, S.-J. and Schreyer, H.L., 1995. Application of a particle-in-cell method to solid mechanics. *Computer Physics Communications* 87, 236-252.

Sulsky, D. and Schreyer, H.L., 2004. MPM simulation of dynamic material failure with decohesion constitutive model. *European Journal of Mechanics A Solids* 23, 423-445.

Sulsky, D. and Schreyer, H.L., 1996. Axisymmetric form of the material point method with Applications to Upsetting and Taylor Impact Problems. *Computer Methods in Applied Mechanics and Engineering* 139, 409-429.

Sulsky, D., Zhou, S-J. and Schreyer, H.L., 1995. Application of a particle-in-cell method to solid mechanics," *Computer Physics Communications* 87, 236-252.

Sulsky, D., 2003. A numerical study of compaction of dry granular material. *Materials Research Society Symposium Proceedings* 759, MM3.1.1-9.

Sun, Y., Bell, T. and Zheng, S., 1995. Finite element analysis of the critical ratio of coating thickness to indentation depth for coating property measurements by nanoindentation. *Thin Solid Films* 258, 198-204

Tabor, D., 1970. The hardness of solids. *Review of Physics in Technology* 1, 145-179.

Tan H. and Nairn, J.A., 2002. Hierarchical, Adaptive, Material Point Method for Dynamic Energy Release Rate Calculations. *Computer Methods in Applied*

*Mechanics and Engineering* 191, 2095-2109

Timoshenko, S., 1940. Theory of plates and shells. McGraw-Hill, New York and London.

Tvergaard, V. and Hutchinson, J.W., 1993. The influence of plasticity on mixed mode interface toughness. *Journal of the Mechanics and Physics of Solids* 41, 1119-1135.

Ulm, F.-J. and Abousleiman, Y., 2006. The nanogranular nature of shale. *Acta Geotechnica* 1, 77-88.

Wang, H.F. and Bangert, H., 1993. Three-dimensional finite element simulation of Vickers indentation on coated systems. *Materials Science and Engineering* A163-1, 43-50

Wang, Q. and Lade, P.V., 2001. Shear banding in true triaxial tests and its effect on failure in sand. *Journal of Engineering Mechanics* 127(8), 754-761.

Washabaugh, P.D. and Knauss, W.G., 1994. A reconciliation of dynamic crack velocity and Rayleigh wave speed in isotropic brittle solids. *International Journal of Fracture* 65, 97-114.

Wieckowski, Z., 2004. The material point method in large strain engineering problems. *Computer Methods in Applied Mechanics and Engineering* 193, 4417-4438.

Xia, K., Rosakis, A.J. and Kanamori, H., 2004. Laboratory earthquakes: The sub-Rayleigh-to-supershear rupture transition. *Science* 303, 1859-1559.

Xia, K., Rosakis, A.J., Kanamori, H. and Rice, J., 2005. Laboratory earthquakes along inhomogeneous faults: directionality and supershear. *Science* 308, 681-684.

Xu, X.-P. and Needleman, A., 1994. Numerical simulations of fast crack growth in brittle solids. *Journal of the Mechanics and Physics of Solids* 42 (9), 1397-1434.

Yang, B. and Ravi-Chandar, K., 1996. On the role of the process zone in dynamic fracture. *Journal of the Mechanics and Physics of Solids* 44 (12), 1955-1976.

.

LIST OF JOURNAL PUBLICATIONS

Lu, H., Daphalapurkar, N.P., Wang, B., Roy, S., Komanduri, R., 2005. Multiscale simulation from atomistic to continuum – Coupling molecular dynamics (MD) with the material point method (MPM). *Philosophical Magazine* 86(20), 2971-2994.

Daphalapurkar, N.P., Lu, H., Coker, D., Komanduri, R., 2007. Simulation of dynamic crack growth using generalized interpolation material point (GIMP) method. *International Journal of Fracture Mechanics* 143, 79-102.

Huang, G., Daphalapurkar, N.P., Gan, R., Lu, H., 2008. Measurement of linear viscoelastic properties of human tympanic membrane using nanoindentation. *ASME Journal of Biomechanical Engineering* 130, 014501, 1-7.

Daphalapurkar, N.P., Hanan, J., Phelps, N., Bale, H., Lu, H., 2008. Simulation of microstructure evolution of a closed-cell polymeric foam in compression. *Special Issue on Micro- and Nanomechanics Mechanics of Advanced Materials and Structures* edited by Prof. J. N. Reddy (in press).

Daphalapurkar, N.P., Dai, C., Gan, R., Lu, H., 2008. Characterization of the linearly viscoelastic behavior of human tympanic membrane by nanoindentation. *Journal of Mechanical Behavior of Biomedical materials* doi:10.1016/j/jmbbm.2008.05.008.

Daphalapurkar, N.P., Lu, H., Komanduri, R., 2008. Measurement of mechanical properties of sand grains using nanoindentation. *Geotechnique* (in review).

VITA

Nitin Pandurang Daphalapurkar

Candidate for the Degree of

Doctor of Philosophy

Dissertation:   MODELING AND SIMULATION OF DYNAMIC PROBLEMS IN
                SOLID MECHANICS USING MATERIAL POINT METHOD


Major Field:  Mechanical Engineering

Biographical:

        Education:
        Completed the requirements for the Doctor of Philosophy in Mechanical
        Engineering at Oklahoma State University, Stillwater, Oklahoma, U.S.A. in
        December, 2008. Received Bachelor of Engineering degree in Mechanical
        Engineering from University of Pune, Maharashtra, India and Master of Science
        degree in Mechanical Engineering from Oklahoma State University, Stillwater,
        Oklahoma, U.S.A.


        Experience: As a graduate teaching research assistant from January 2003 to
                December 2007, and a graduate research assistant from January 2004 to
                July 2008 with the School of Mechanical and Aerospace Engineering,
                Oklahoma State University, Stillwater, Oklahoma, U.S.A.

        Professional Memberships:
                *Phi Kappa Phi* (Collegiate honorary society),
                *Sigma Gamma Tau* (Collegiate aerospace engineering honorary society),
                *Society of Engineering Sciences, Society of Experimental Mechanics,*
                and *American Society of Mechanical Engineers* (Student member)

Name: Daphalapurkar, Nitin Pandurang   Date of Degree: December, 2008

Institution: Oklahoma State University   Location: Stillwater, Oklahoma

Title of Study: MODELING AND SIMULATION OF DYNAMIC PROBLEMS IN
      SOLID MECHANICS USING MATERIAL POINT METHOD

Pages in Study: 150    Candidate for the Degree of Doctor of Philosophy

Major Field: Mechanical Engineering

Scope and Method of Study:

A relatively new computational method, namely, material point method (MPM), developed by Prof. Sulsky[1] of University of New Mexico from the Particle-In-Cell (PIC) method in computational fluid mechanics, was used for simulations of dynamic problems in solid mechanics. In this regard, some dynamic and material simulations have been carried out, such as dynamic crack growth using cohesive zone model, microstructure evolution of closed-cell polymer foam in compression, and simulation of granular materials. In this process, the MPM algorithm was developed by either implementing completely newer capabilities of simulation or refining the older versions for increased robustness and versatility.

Findings and Conclusions:

The incorporation of a characteristic length scale in MPM through cohesive zone model enabled investigation of physics-based dynamic crack propagation. The simulations are capable of handling crack growth with crack-tip velocities in both sub-Rayleigh and intersonic regimes. Crack initiation and propagation are the natural outcomes of the simulations incorporating the cohesive zone model. Good qualitative agreement was obtained between numerical results presented here and the experimental results reported in the literature in terms of the photoelastic stress patterns ahead of the crack-tip.

MPM can be used to predict of material properties for microstructures driving the optimization of processing and performance in foam materials through simulation of real microstructures. The simulations are capable of capturing various stages of deformations in foam compression. The stress-strain curve simulated from MPM compares reasonably with the experimental results. Based on the results from μ-CT and MPM simulations, it was found that elastic buckling of cell-walls occur even in the elastic regime of compression. Within the elastic region, less than 35% of the cell-wall material carries majority of the compressive load.

The particle nature in MPM was found to be suitable for simulation of granular materials. A contact algorithm has been implemented in MPM to allow MPM to handle slip and friction between bodies in contact. Nanoindentation was carried out on sand grains to determine its properties at the granular level, which can be used along with μ-CT to carry out granular simulations of sand.

---

[1] Sulsky, D., Zhou, S.-J., and Schreyer, H. L., "Application of a particle-in-cell method to solid mechanics," *Computer Physics Communications* **87**, 236-252 (1995).

ADVISER'S APPROVAL: Dr. Hongbing Lu